主　論　文

Study of the polarization characteristics of Pc1 geomagnetic pulsation at low and subauroral latitudes

（低緯度およびサブオーロラ帯での
Pc1地磁気脈動の偏波特性の研究）

野 村 麗 子

名古屋大学大学院 理学研究科 素粒子宇宙物理学専攻
太陽地球環境研究所

2012

Study of the polarization
characteristics of
Pc1 geomagnetic pulsation
at low and subauroral latitudes

STEL

Reiko Nomura

Graduate School of Science

Nagoya University

Doctor of Philosophy

March 2012

Abstract

Pc1 geomagnetic pulsation is a geomagnetic oscillation with frequencies of 0.2-5.0Hz typically observed by induction magnetometers on the ground. One of the source of Pc1 pulsation at low-subauroral latitudes (L<∼4) is the electromagnetic ion cyclotron (EMIC) wave excited in the equatorial region and propagated into the ionosphere along the magnetic field line. The EMIC waves also interact with magnetospheric ions and let them precipitate into the ionosphere to cause the isolated proton auroras. The interaction of EMIC waves with MeV-energy electrons is considered as a key phenomenon of the loss mechanism of MeV electrons in the radiation belt. However, contribution of EMIC waves to the loss mechanism of MeV electrons are still under study.

Ground induction magnetometer is a powerful tool to investigate the source region of Pc1/EMIC waves. Even away from the footprints where Pc1/EMIC waves enter into the ionosphere, we can observe the waves because of the ionospheric duct propagation of the waves. Using ground induction magnetometer chain, previous studies have tried to determine the wave source location by the polarization or amplitude analysis. However only analog data have been used in their studies and none of them compared the estimated wave-source locations with the isolated proton aurora which indicates the wave source location in the ionosphere at subauroral latitudes. In this thesis we investigate the ionospheric duct propagation of Pc1/EMIC waves in more detail by the polarization analysis with newly developed induction magnetometer chain at low and subauroral latitudes.

First we investigated Pc1 pulsations observed by induction magnetometers at three low-latitude stations (Paratunka (PTK), Moshiri

(MSR), and Sata (STA), L=1.2-2.1). A detailed polarization analysis shows that polarization parameters (angle of polarization ellipse orientation, Ψ, and polarization sense, ε) of individual Pc1 bands depend on frequency at all three stations. The dependence of Ψ on frequency was seen in $\sim$70% of the 93 Pc1 events observed at MSR (L=1.5) from July 14, 2007 to July 13, 2009. The maxima of seasonal and diurnal variations of the Pc1 occurrence rate were in winter and during the nighttime, as reported previously, indicating that the transmission of observed Pc1 pulsations to lower latitudes is controlled by the density of the F layer plasma. These facts suggest that spatially distributed Pc1 waves with varying frequencies depending on longitude or latitude at high latitudes propagated in the ionospheric duct to cause the frequency dependence of polarization parameters at low latitudes. We also found the Pc1 pearl structure with a repetition period of $\sim$5-30 s which is shorter than the periods expected from the bouncing wave packet model. The variation of Ψ was associated with that of the pearl structure. We suggest that the Pc1 pearl structure observed at low latitudes is a beat of high-latitude waves with slightly different frequencies.

Then we investigated the polarization of Pc1 pulsations and related proton auroras at subauroral latitudes, using an induction magnetometer and an all-sky camera at Athabasca, Canada (54.7°N, 246.7°E, magnetic latitude (mlat) 61.7°N). Isolated proton auroras often appear in association with Pc1 pulsations because of proton scattering by EMIC waves in the magnetosphere. We used the proton aurora as a proxy for the location and size of the Pc1 ionospheric source. For 27 Pc1 events with simultaneously observed proton auroras over 4 years from September 7, 2005 to September 6, 2009, we calculated the distances between the Pc1 ionospheric source and the observation site, normalized by the horizontal scale size of the source. We tried three different definitions of the scale size of Pc1 ionospheric source to calculate the normalized distances. We found that the rotation angle θ between the Pc1 polarization ellipse and the direction to the

proton aurora changes from 90° to 0° as the normalized distance increases. For the definition of the scale sizes that gives most clear θ-transition from 90° to 0°, the transition occurs at the normalized distance $\sim$2.0-4.0, while it was $\sim$1.0-2.0 by the model calculation of Fujita and Tamao [1988]. The averaged major axes tend to point toward the proton aurora at larger distances. The difference of the transition location may imply that the Pc1 ionospheric sources are larger than the isolated proton auroras, or that the inhomogenuity of the ionospheric conductivity by the proton precipitation affects the transition distances.

I would like to dedicate this thesis to everyone
whom I met in my life.

Acknowledgements

Contents

List of Figures

Chapter 1

Introduction

1.1 Overview

Pc1 geomagnetic pulsation (Pc1) is observed as a geomagnetic oscillation with the frequency range of 0.2-5.0 Hz on the ground by induction magnetometers. This frequency range is classified by Jacobs et al. [1964] as shown in Figure 1.1. For the hydromagnetic (HM) emissions at Syowa in the range of 0.1-2.0 Hz,

Notation	Period Range, sec
Pc 1	0.2– 5
Pc 2	5 – 10
Pc 3	10 – 45
Pc 4	45 –150
Pc 5	150 –600

Figure 1.1: Classification of geomagnetic pulsations (after Jacobs et al. [1964]).

Fukunishi et al. [1981] classified eight subtypes of geomagnetic pulsations in the Pc1 frequency range based on spectral structures (Figure 1.2). They showed that each subtype has a preferential magnetic local time interval and frequency range for its occurrence. For example, periodic HM emission with dispersive spectral structure and HM chorus occur around magnetic local noon and in the afternoon,

1

respectively. The frequencies of HM emissions vary from high frequencies in the morning hours to low frequencies in the afternoon. They discussed that the local time dependence of the frequency seemed to be explained by the L value dependence of the plasmapause location if HM emissions are generated near the plasmapause.
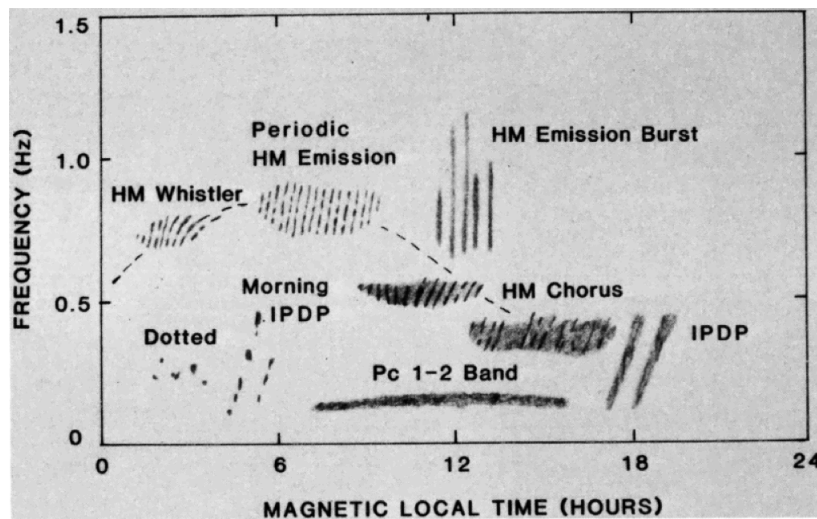
Figure 1.2: Summary plot showing the dependence of each subtype HM emissions in the Pc1 frequency range on frequency and magnetic local time. (after Fukunishi et al. [1981])

One of the Pc1 generation mechanisms is that the electromagnetic ion cyclotron (EMIC) waves excited by the ion cyclotron instability in the equatorial region of the magnetosphere, propagate along the geomagnetic field line into the ionosphere. Figure 1.3 shows a schematic picture of the generation and propagation mechanisms of Pc1/EMIC waves. Magnetospheric plasma particles are scattered by EMIC waves and precipitate into the ionosphere. The precipitation of ions make the proton aurora at altitudes of 110-140km. When EMIC waves reach the ionosphere, the interaction with the ionospheric plasma generates fast mode waves. These waves are partly trapped in the ionospheric duct at the F layer and propagate horizontally. The electromagnetic waves produced by ducting ionospheric waves are observed as Pc1 geomagnetic pulsations (Pc1) with frequencies of 0.2-5.0 Hz on the ground (e.g., Greifinger [1972], Fujita and Tamao
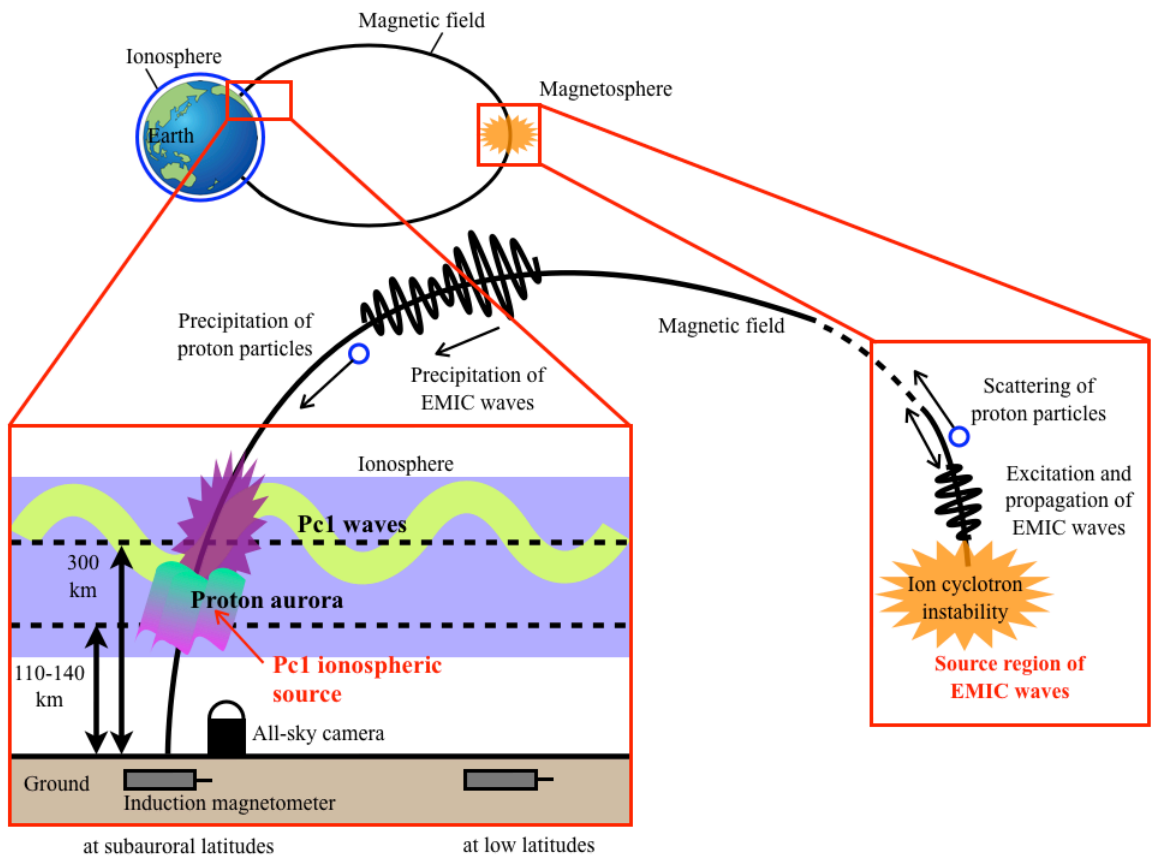
Figure 1.3: Schematic picture of the generation and propagation mechanism of Pc1/EMIC waves

[1988]).

Until the 1980s, the Pc1 geomagnetic pulsation has been studied extensively using the ground magnetometer data. Associated with the duct propagation process of Pc1 in the ionosphere, the attenuation effect (< 10 dB/1000 km), group velocity (300-800 km/s), propagation direction (mostly along the geomagnetic meridian), and polarization parameters were investigated using multi-point magnetometers at high and low latitudes (e.g., Kawamura et al. [1981]; Fraser [2001]). Statistical analyses also reveal the Pc1 characteristics, more frequent occurrences in winter months and less in summer months (Kawamura et al. [1983]).

1.2 Electromagnetic ion cyclotron (EMIC) waves

Here we describe growth of the EMIC waves and their interaction with plasma, according to the descriptions by Fukunishi et al. [1981]. When the temperature of high energy ions in the direction parallel to the local magnetic field line differs from that in the perpendicular direction, or the pitch angle distribution of ions is not isotropic, the ion cyclotron wave grow by obtaining the energy from ions in order to recover from the anisotropy. This process is called as the ion cyclotron instability. At the radiation belt in the magnetosphere, the ion cyclotron instability is frequently occurred because of the loss cone distribution of ions. The growth rate γ of the ion cyclotron wave is expressed as,

$$\gamma = \sqrt{\pi} \frac{N_1}{N_0} \frac{\omega_{ci}^2}{kU_{\parallel}} \frac{(1-x)^2}{2-x} \left[A \left(\frac{1-x}{x} \right) - 1 \right] \exp \left[-\frac{\omega_{ci}^2 (1-x)^2}{k^2 U_{\parallel}^2} \right], \qquad (1.1)$$

where k is the Boltzmann constant, N_0 and N_1 are the cold and hot plasma densities, respectively, ω_{ci} is the angular frequency of the ion cyclotron wave, $x = \omega/\omega_{ci}$, $A = T_{\perp}/T_{\parallel} - 1$ is the temperature anisotropy constant, $T_{\perp}$ and $T_{\parallel}$ are the perpendicular and parallel temperature, respectively, $U_{\parallel} = \left(\frac{2kT_{\parallel}}{m_i} \right)^{\frac{1}{2}}$, and m_i is the ion mass (Fukunishi et al. [1983]). The cyclotron waves grow at $\gamma > 0$. Thus $T_{\perp} > T_{\parallel}$ is the necessary condition for the wave growth. The cyclotron waves interchange their energy with ions through the ion cyclotron resonance.

We consider transverse waves propagating along the homogenous magnetic

field $\boldsymbol{B}_0$. The electric and magnetic field of waves are $\boldsymbol{E} \propto \exp[i(\boldsymbol{k} \cdot \boldsymbol{r} - \omega t)]$ and $\boldsymbol{B} \propto \exp[i(\boldsymbol{k} \cdot \boldsymbol{r} - \omega t)]$, respectively. By substituting $\boldsymbol{E}$ and $\boldsymbol{B}$ in Maxwell equations, we obtain $\boldsymbol{k} \times \boldsymbol{E} = \omega \boldsymbol{B}$. Then the phase velocity v_p is $v_p = \omega/k = |E/B|$. A particle moving along $\boldsymbol{B}_0$ with a velocity v_p will not feel an action $\boldsymbol{F}$ by $\boldsymbol{E}$ because of $\boldsymbol{F} = q(\boldsymbol{E} + v_p \times \boldsymbol{B}) = 0$, where q is a particle charge. Therefore in the system moving with a phase velocity v_p the kinetic energy will be conserved,

$$\frac{1}{2}m{v_\perp}^2 + \frac{1}{2}m(v_\parallel - v_p)^2 = \text{const.}, \tag{1.2}$$

where $v_\perp$ and $v_\parallel$ are particle velocities in the directions parallel and perpendicular to the local magnetic field in a static system. In the case that the particle velocity changes slightly ($\Delta \boldsymbol{v} = \Delta \boldsymbol{v}_\perp + \Delta \boldsymbol{v}_\parallel$), we will obtain the following equations in a first-order approximation.

$$mv_\perp \Delta v_\perp + m(v_\parallel - v_p)\Delta v_\parallel = 0 \tag{1.3}$$

If we set

$$\Delta W \;\; = \;\; \Delta W_\perp + \Delta W_\parallel \tag{1.4}$$

$$\Delta W_\perp \;\; = \;\; mv_\perp \Delta v_\perp \tag{1.5}$$

$$\Delta W_\parallel \;\; = \;\; mv_\parallel \Delta v_\parallel, \tag{1.6}$$

by using eq. 1.3 we will get $\Delta W = mv_\perp \Delta v_\perp + mv_\parallel \Delta v_\parallel = mv_p \Delta v_\parallel$. Therefore, $\Delta W_\parallel$ and $\Delta W_\perp$ are expressed as follows,

$$\frac{\Delta W_\perp}{\Delta W} \;\; = \;\; \frac{mv_\perp \Delta v_\perp}{mv_p \Delta v_\parallel} = \frac{mv_p \Delta v_\parallel - mv_\parallel \Delta v_\parallel}{mv_p \Delta v_\parallel} = 1 - \frac{v_\parallel}{v_p} \tag{1.7}$$

$$\frac{\Delta W_\parallel}{\Delta W} \;\; = \;\; \frac{mv_\parallel \Delta v_\parallel}{mv_p \Delta v_\parallel} = \frac{v_\parallel}{v_p}. \tag{1.8}$$

The condition of the cyclotron resonance is

$$\omega - k_\parallel v_\parallel = \omega_{ci}, \tag{1.9}$$

where ω is the angular frequency of waves, $k_\parallel$ is the wave number vector and $v_\parallel$

is the velocity of ions both in the direction parallel to the local magnetic field line. The equation 1.9 means that for the ions with a velocity $v_\parallel$ the frequency of the doppler-shifted wave is equal to the ion cyclotron frequency. In this cyclotron resonance, waves and particles move in the opposite directions each other.

Because the frequency of the ion cyclotron waves is lower than the ion cyclotron frequency ($\omega < \omega_c$), for the ion cyclotron resonance, from eq. 1.9 we will obtain $k_\parallel v_\parallel < 0$. Also from eq. 1.9,

$$\frac{k_\parallel v_\parallel}{\omega} = \frac{v_\parallel}{v_p} = 1 - \frac{\omega_c}{\omega}. \tag{1.10}$$

Then eq. 1.7 and eq. 1.8 will be

$$\frac{\Delta W_\perp}{\Delta W} = \frac{\omega_c}{\omega} > 1 \tag{1.11}$$

$$\frac{\Delta W_\parallel}{\Delta W} = 1 - \frac{\omega_c}{\omega} < 0. \tag{1.12}$$

When the energy moves from a particle to a wave ($\Delta W < 0$), from eq. 1.11 and eq. 1.12, we obtain $\Delta W_\perp < \Delta W < 0$ and $\Delta W_\parallel > 0$, respectively.

The particle energy in the direction perpendicular to the local magnetic field line is partially converted to the wave energy, and at the same time the velocity $v_\parallel$ increase. Thus the pitch angle of ions become smaller by the cyclotron resonance and consequently the pitch angle is scattered to cause the precipitation of ions to the ionosphere.

1.3 Pc1 geomagnetic pulsations

1.3.1 Ground observation of Pc1 geomagnetic pulsations

Electromagnetic ion cyclotron (EMIC) waves are excited in the equatorial region of the inner magnetosphere by the ion cyclotron instability (ICI) of energetic resonant ions with an anisotropic energy distribution. The regimes of the ICI may differ at latitudes beyond and near the plasmapause projection. At higher latitudes the fluxes of energetic ions are often near the ICI threshold, and even modest compression of the magnetosphere can trigger EMIC wave excitation

(Engebretson et al. [2002]). At lower latitudes near the plasmapause, EMIC waves are generated by ring current protons in the late recovery phase of magnetic storms. EMIC waves propagate along the magnetic field lines to the ionosphere. When EMIC waves reach the ionosphere, the interaction with the anisotropic ionospheric plasma results in compressional mode generation. A part of the compressional wave, in the frequency range above the cutoff frequency, can be trapped in the ionospheric duct at the F layer and propagate horizontally to lower or higher latitudes. This ionospheric cavity also forms the Ionospheric Alfvén Resonator (IAR) (e.g., Pilipenko et al. [2002]), where part of the incident Alfvén wave energy can be trapped. On the ground, the electromagnetic fields of these ionospheric waves are observed as Pc1 geomagnetic pulsations in the frequency range of 0.2-5.0 Hz.

1.3.2 Frequency

The Pc1 frequency is expected to be higher for the Pc1 ionospheric source at lower latitudes because the frequency f_{ci} of the ion cyclotron waves is proportional to the magnetic field B ($f_{ci} = eB/m_i$). When the Pc1 frequency increases, simultaneously observed isolated proton auroras as Pc1 ionospheric sources move equatorward (e.g., Sakaguchi et al. [2008], Yahnin et al. [2009]). For latitudinal distributions of high-latitude Pc1 source region, Kawamura et al. [1981] found by comparing between high- and middle-latitude ground observations that Pc1 pulsations appear first at low latitudes and then shift to higher latitudes probably associated with outward expansion of the plasmasphere during the recovery phase of intense geomagnetic storm. Plyasova-Bakounina et al. [1996] observed that the Pc1 frequency increases depending on the latitudes from high to low latitudes. Mursula et al. [1997] showed using data from the ionospheric Viking satellite that the Pc1 frequency shifts from 0.3 to 0.6 Hz as the satellite moves from L=6.3 to 5.6.

1.3.3 Ionospheric duct propagation

When the left-hand polarized Pc1 wave packets enter the high-latitude ionosphere, the waves are converted into the compressional waves through a mode

conversion, and propagate horizontally in the ionospheric duct centered by the F layer (e.g., Greifinger and Greifinger [1968]). Figure 1.4 shows a schematic
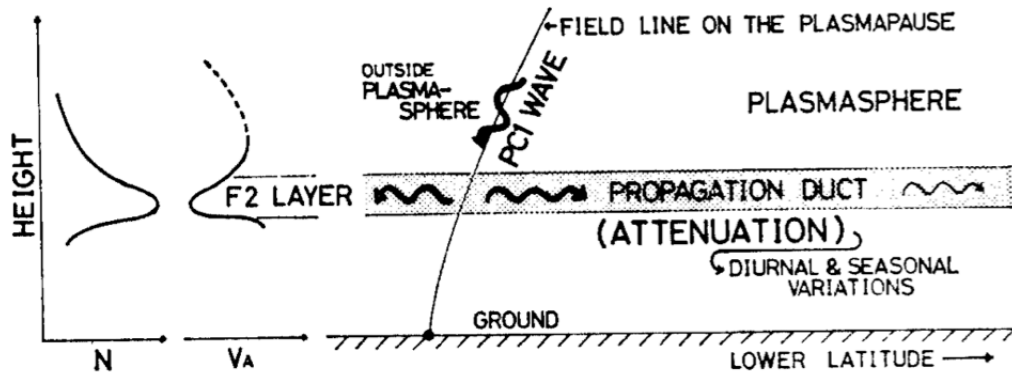
Figure 1.4: A schematic picture of the ionospheric duct propagation (after Kawamura et al. [1981]).

picture of the ionospheric duct propagation by Kawamura et al. [1981]. There is a local minimum of the Alfvén velocity in the ionospheric F layer due to the electron density maximum at ∼300km. Pc1 waves are trapped in this region and propagates to lower latitudes.

The plasma density of the ionosphere controls Pc1 propagation from high to low latitudes. Although the Pc1 waves observed at high latitudes can result from direct incidence of magnetospheric EMIC waves, the Pc1 waves at low latitudes are due to the propagation along the ionosphere. This difference in the physical mechanism results in the different Pc1 occurrence rates at high and low latitudes. At low latitudes, Pc1 waves are observed most frequently during the nighttime with a maximum at 1-2 h before sunrise, whereas at high latitudes Pc1 pulsations are observed mostly during the daytime with a maximum at ∼1 h after magnetic local noon (Fraser [1968]; Kuwashima et al. [1981]). There is also a seasonal difference: high occurrence rates in winter at low latitudes and in equinox months at high latitudes. These Pc1 characteristics at low latitudes indicate that a decreasing electron density of the F layer, which is the center of the ionospheric duct, favors Pc1 occurrence (Kawamura et al. [1981]). The Pc1 occurrence rate also has a negative correlation with solar activity parameterized by the sunspot

numbers (Kawamura et al. [1983]).

1.3.4 Polarization characteristics

The polarization parameters of Pc1 waves observed on the ground may hold important information about the location of their ionospheric source. According to theoretical predictions (e.g., Greifinger [1972]; Fujita and Tamao [1988]) the polarization parameters (polarization ellipse orientation and ellipticity) associated with the incidence of localized Alfvén waves (with a horizontal scale size r_0), vary significantly with both r_0 and the distance r from the source to the observation point.

1.3.4.1 Major axis of Pc1 polarization waves

Fujita and Tamao [1988] gave a detailed model calculation of the Pc1 polarization in the vicinity of the Pc1 ionospheric source as shown in Figure 1.5. The
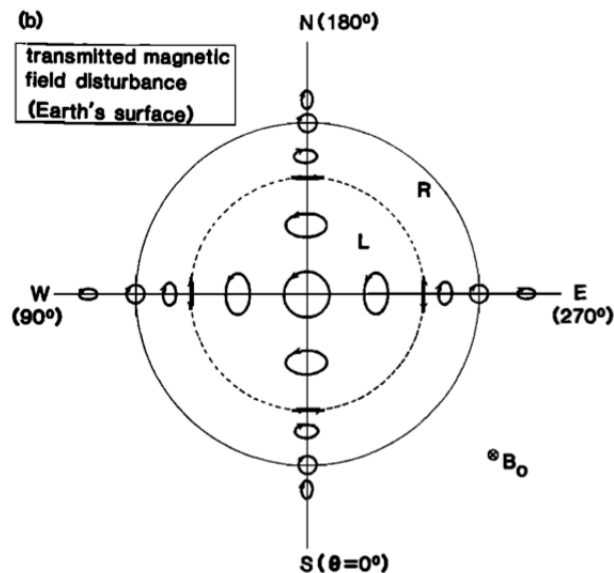
Figure 1.5: A schematic picture of the polarization patterns for horizontal magnetic field variations on the ground (after Fujita and Tamao [1988]).

orientation of the polarization ellipse observed on the ground changes from az-

imuthal to radial direction depending on both the horizontal size of source r_0 and the distance r from source to the observing point, as a result of the coupling of incident Alfvén waves and ducted compressional waves of Pc1 pulsations in the ionosphere. Near the source region ($r \leq r_0$), the polarization structure is the same as that of incident waves and the minor axis of the polarization ellipse points toward the source center. In the intermediate and far-zone regions ($r \gg r_0$) the major axis of the polarization ellipse points to the source center. This theoretical prediction implies that the orientation of Pc1 wave ellipses could be used for the remote location of a source region.

The major axis direction of the Pc1 polarization ellipse observed on the ground has been used to investigate the position of the Pc1 ionospheric source. Fraser and Summers [1972] found that direction of major axis of linearly polarized waves pointed to the possible source location at high latitudes under nighttime ionospheric conditions. The variations of the ducted ray-path direction will be small at nighttime because the F layer is reasonably uniform. Some other Pc1 observations at low latitudes consistently indicated the possible ionospheric source region of the waves to be at high latitudes. The locations of high-latitude sources determined by the polarization method were consistent with those determined by the triangulation method, using the arrival times of Pc1 waves at the three stations (Fraser [1975a]). Fraser [1975b] showed that the polarization parameters obtained at high and low latitudes were often consistent and related to each other in both statistical and case studies. Webster and Fraser [1984] found that the polarization ellipse orientations of Pc1 waves observed at two low-latitude stations are stable in time over the duration of a Pc1 segment, implying corotating magnetospheric sources of EMIC waves. They also found that different Pc1 segments often show different directions of arrival, implying multiple localized source cells of EMIC waves in the magnetosphere. Therefore, the polarization method gives the possibility of monitoring the spatial and temporal structure of Pc1 sources at high latitudes using the polarization ellipse orientation of Pc1 pulsations observed at low latitudes.

There are, however factors that may substantially degrade this method. For example, the lateral gradients of the ionospheric plasma density, especially in the vicinity of the terminator, can distort the polarization ellipse orientation

(Summers [1974]; Summers and Fraser [1972]). Large changes in the F layer are expected associated with the time of sunrise and sunset (Fraser [1975b]). Althouse and Davis [1978] showed that polarization characteristics obtained using narrow-band filters often varied significantly in time, and the propagation direction determined by the major axis of the Pc1 polarization ellipse did not agree with that determined from multi-point propagation delay measurements. The other method used to find the possible location of the Pc1 ionospheric source is the distribution of Pc1 amplitudes with multi-point observations (Hayashi et al. [1981]).

None of previous studies, however, has compared these observations with the actual location of Pc1 ionospheric source. We do not know whether the major axis of Pc1 polarization waves points toward the Pc1 ionospheric source as suggested by the model calculation.

1.3.4.2   Polarization sense

Near the wave incidence region from the magnetosphere ($r \leq r_0$), the polarization structure is the same as those of incident wave: disturbances are left-handed (LH) polarized with the minor axis of the polarization ellipse oriented toward the incidence center. In the intermediate and far-zone regions ($r \gg r_0$), the ground signals are expected to be right-handed (RH) elliptically polarized with the polarization ellipse orientation pointing to the incidence center. The polarization sense of incident Pc1 waves was expected to be LH, because EMIC waves with this polarization interact effectively with energetic protons. The left-hand polarization should be observed dominantly at high latitudes, while the rate of right-hand polarized waves should increase with increasing distance from the high-latitude source region. In the multi-point observation, the nearest station to the high latitude source, which is connected to the magnetospheric source, can be determined by comparing the rate of the right- to left-handed polarization waves (Fraser [1976]). However, the polarization sense can be reversed during EMIC wave propagation along the geomagnetic field lines across the crossover frequencies (Rauch and Roux [1982]). Further satellite and ground observations showed that elegant models of Alfvén wave interactions with the ionosphere (Fujita and

Tamao [1988]; Lysak [1999]) are oversimplified descriptions of the polarization sense. Indeed, Hayashi et al. [1981] found from multipoint observations over Canada that Pc1 pulsations observed near a high-latitude source location which was determined by the spatial distribution of Pc1 amplitudes, did not necessarily have LH polarization. Low-altitude satellite observations showed that incident Pc1 waves in the topside ionosphere were highly localized (<100 km) in the direction transverse to B and were composed of a mixture of LH and RH modes (Iyemori and Hayashi [1989]; Engebretson et al. [2008]).

In order to understand the propagation process of Pc1/EMIC waves from the magnetosphere to the ionosphere, and from the high to low latitudes in the ionosphere, we need to investigate the polarization sense comparing with the distance from the source to the observation point.

1.3.5 Pearl structure

The Pc1 pulsation can be classified into two types: structured and less-structured. The structured Pc1 is often called as "pearl", which is a periodic intensification of Pc1 amplitudes with repetition periods of ∼30-40 s. The pearl structure is most common at low to middle latitudes and less observed at high latitudes (Mursula [2007]). The idea of bouncing wave packet (BWP) along geomagnetic field line is one of the explanations for the Pc1 pearl structure (Jacobs et al. [1964]; Obayashi [1965]). According to BWP, the repetitive pearl structure is generated by a wave packet bouncing along the geomagnetic field line between the northern and southern hemispheres, losing part of its energy when reflecting from the ionospheres and gaining energy when traversing through the equatorial growth region like VLF whistler mode. However, the BWP idea is in contradiction with satellite observations. Mursula et al. [1997] observed Pc1 burst with a repetition period 40-45 seconds by the Viking satellite. The observed repetition periods were shorter than a period predicted by BWP. Usanova et al. [2008] also reported a THEMIS and ground-satellite observation of Pc1 pulsations, showing that the observed repetition period was not explained by BWP. Erlandson et al. [1992] showed that Pc1 waves reflected from the ionosphere are very weak, less than ∼10-20% of the downward-directed wave amplitudes. These results indicate that

some new explanation is necessary for the Pc1 pearl structures.

New ideas based on the equatorial growth modulation (EGM) of Pc1 growth rate are introduced by Erlandson et al. [1992] and Mursula [2007]. Mursula [2007] showed that the EGM model naturally explains the Pc1 pearl structures as the perturbation of some critical plasma parameters, which could lead to instability raising and lowering the Pc1 wave growth in the equatorial source region. Both ground and satellite observations reported the simultaneous occurrence of Pc1 pearl structures and lower-frequency ULF waves with a period matching the pearl repetition period, suggesting that the lower-frequency ULF wave could modulate the Pc1 wave amplitude. However in order to determine this idea as the mechanism of the pearl structure, we should investigate statistically the relation between the repetition period and the amplitudes of simultaneously observed ULF waves.

1.4 Isolated proton aurora at subauroral latitudes

Magnetospheric ions are scattered by resonance with EMIC waves and precipitate into the ionosphere to cause isolated proton auroras at subauroral latitudes. Yahnina et al. [2000] found from NOAA satellite and ground observations that localized proton precipitation (> 30keV) is related to the ground Pc1 waves and the frequency of Pc1 waves decreases with increasing proton aurora latitudes. This suggests that the Pc1 waves are the result of the ion cyclotron instability. (Sakaguchi et al. [2007] and Sakaguchi et al. [2008]) found a one-to-one correspondence between the isolated proton auroras observed by a ground all-sky camera and the Pc1 waves observed by a ground induction magnetometer. The localized proton auroras associated with Pc1 waves were also observed by the IMAGE satellite (e.g., Yahnin et al. [2007]; Yahnina et al. [2008]).

We observe two emission lines, 486.1 nm and 557.7 nm in the isolated proton aurora. The precipitating protons along the magnetic field line collide with atoms

and molecules in the neutral atmosphere which are ionized or excited as,

$$H^+ + X \rightarrow H^+ + X^{+(*)} + e \qquad (1.13)$$

$$H^+ + X \rightarrow H^+ + X^*. \qquad (1.14)$$
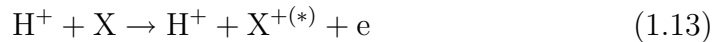
The secondary electrons in eq. 1.13 collide with oxygens to excite them to the $O(^1S)$ state which emits 557.7 nm emission when it shifts to the lower state $O(^1D)$. Excited oxygens will emit 557.7 nm. At the same time, protons are excited by the charge exchange reaction with the neutral atmosphere.

$$H^+ + X \rightarrow H^* + X^{+(*)} \qquad (1.15)$$

Excited hydrogen H^* will shift to the ground state by emitting 486.1-nm emission. Most of the precipitated protons are neutralized at altitudes of 300-500 km (e.g., Davidson [1965]; Fukunishi et al. [1981]). The neutralized energetic hydrogens can move across the magnetic field in the ionosphere.

Then energetic hydrogens collide with atoms and molecules in the neutral atmosphere to ionize or excite them again.

$$H + X \rightarrow H^+ + X^{(*)} + e \qquad (1.16)$$

$$H + X \rightarrow H^- + X^{+(*)} \qquad (1.17)$$

Protons become excited hydrogen by the charge exchange reaction in eq. 1.15 again. These processes continue repeating until the energy of precipitating protons vanishes.

Figure 1.6 shows a photo of an isolated proton aurora observed at Athabasca (ATH, L=4.4), Canada at subauroral latitudes.

The isolated proton aurora can be considered as the ionospheric footprint of the interaction between protons and EMIC waves in the equatorial region in the magnetosphere. Thus, the isolated proton aurora indicates the position and size of the Pc1 ionospheric source. However it has not been investigated that how the position and the size of the Pc1 ionospheric source relate to the Pc1 pulsations observed on the ground.

Figure 1.6: Photograph of an isolated proton auroral arc in the southern sky of Athabasca, Canada, taken on September 5, 2005 (after Miyoshi et al. [2008])

1.5 Purpose of this thesis

Ground induction magnetometer is a powerful tool to investigate the source region of Pc1/EMIC waves. Even away from the footprints where Pc1/EMIC waves enter into the ionosphere, we can observe the waves because of the ionospheric duct propagation of the waves. The Pc1 polarization has important information of the Pc1 duct propagation in the ionosphere. The Pc1 polarization on the ground changes their characteristics depending on the distance from the ionospheric source and the size of the ionospheric source. Even though detailed model calculations have revealed the two dimensional distribution of the polarization in the Pc1 ionosphere source, they were not enough to be understood by observations using ground magnetometers. Previous studies have tried to determine the wave source location from the polarization analysis using ground induction magnetometer chain. However only analog data have been used in their studies and none of them compared the estimated wave-source locations with the isolated proton aurora which indicates the wave source location in the ionosphere at subauroral latitudes.

In this thesis we investigate the ionospheric duct propagation of Pc1/EMIC

waves in more detail by the polarization analysis with newly developed induction magnetometer chain at low and subauroral latitudes. In Chapter 2, we show the ground-based stations we used in this thesis and the calibration results of the induction magnetometers at these stations. We also introduce the method of polarization analysis used in this thesis. By this method, in Chapter 3, we investigate the Pc1 polarization characteristics at low latitudes. We show the frequency dependence of the Pc1 polarization observed at three stations, Paratunka in Russia, and Moshiri and Sata in Japan (L=1.2-2.1). From the statistical study, we found that 70% of the 93 Pc1 events observed at Moshiri over two years had the frequency dependence of the polarization. We also show the seasonal and local time dependence of the Pc1 occurrence. From these observation we discuss a possible spatial structure of the Pc1 ionospheric source at high latitudes, and a possible beating mechanism that cause the Pc1 pearl structure. In Chapter 4, we investigate the relation between the Pc1 ionospheric source and the Pc1 polarization on the ground. We used the isolated proton aurora as a proxy for the location and size of the Pc1 ionospheric source. For 27 Pc1 events with simultaneously observed proton auroras over four years at Athabasca in Canada (L=4.4), we calculated the distances between the Pc1 ionospheric source and the observation site, normalized by the horizontal scale size of the source. We found that the rotation angle θ between the Pc1 polarization ellipse and the direction to the proton aurora changes from 90° to 0° as the normalized distance increases. We also found that for the definition of the scale sizes that gives most clear θ-transition from 90° to 0°, the transition occurs at the normalized distance $\sim$2.0-4.0, while it was $\sim$1.0-2.0 by the model calculation. The averaged major axes tend to point toward the proton aurora at larger distances. From these observation we discusse the reason of the discrepancy between the observation and model calculation. Finally in Chapter 6, we conclude this thesis and suggest some future works.

Chapter 2

Instruments and data analysis method

2.1 Induction magnetometer

In this thesis, we use multi-point induction magnetometer data at low and subau-roral latitudes obtained by the Solar-Terrestrial Environment Laboratory, Nagoya University (Shiokawa et al. [2010]). One induction magnetometer was installed at Athabasca (ATH), Canada in 2005 and four induction magnetometers were installed at Magadan (MGD) and Paratunka (PTK), Russia, and Moshiri (MSR) and Sata (STA), Japan in 2007-2008. Table 2.1 shows these station locations in geographic and geomagnetic latitudes and longitudes, and the dates when the data acquisition started. Figures 2.1 and 2.2 indicate the location of these stations.

Table 2.1: Station locations and date of datas acquisition start.

station	glat	glon	mlat	mlon	acquisition start
ATH	54.7	246.7	61.7	306.2	Sep. 7, 2005-
MGD	60.1	150.7	51.9	213.2	Nov. 5, 2008-
PTK	53.0	148.3	45.8	221.4	Aug. 2, 2007-
MSR	44.4	142.3	35.6	209.5	Jul. 14, 2007-
STA	31.0	130.7	21.2	200.5	Sep. 5, 2007-
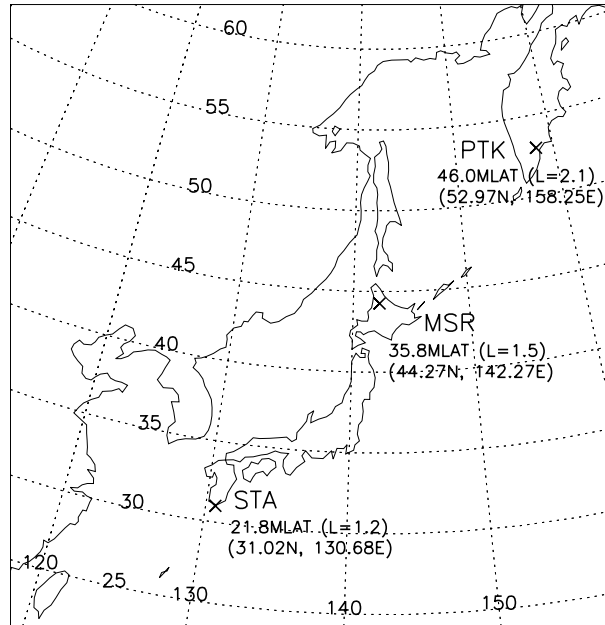
Figure 2.1: Location of the three induction magnetometer stations: Paratunka (PTK) in Russia and Moshiri (MSR) and Sata (STA) in Japan. The dipole magnetic latitudes are calculated using the IGRF-11 model with an epoch time of 2010.
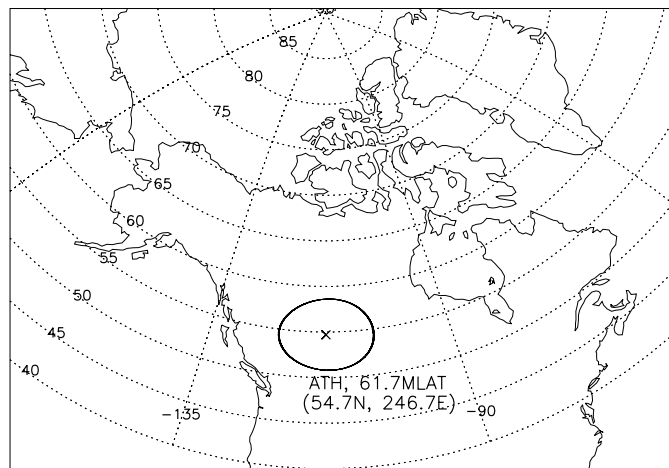
Figure 2.2: Location of the all-sky camera and the induction magnetometer at Athabasca (ATH) in Canada. The dipole magnetic latitude was calculated using IGRF-11 with an epoch time of 2010.

2.1.1 Data Sampling

Figure 2.3 shows the induction magnetometer system installed at these stations. The induction magnetometer sensors (H-, D-, and Z-components) measure mag-
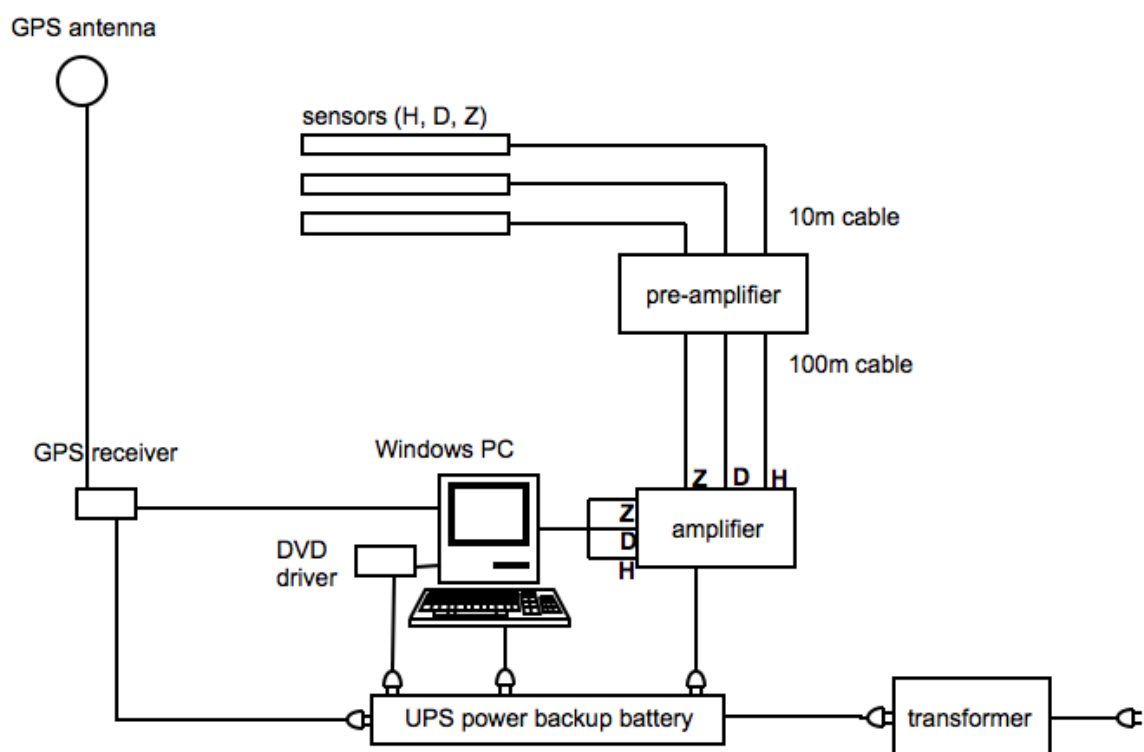
Figure 2.3: Induction magnetometer system.

netic field fluctuations and generate output voltages. Signals are amplified 100 times by the pre-amplifier. This prevent the data from being interfered by the noise in the 100 m cable. Then the signal to noise ratio (SNR) in this system becomes 100 times larger than the one without pre-amplifiers. The GPS receiver generates 1 pps signals with an accuracy of ± 1 μs. The GPS receiver also has the crystal-controlled oscillator generating 12.8 MHz signals. A timing marker

is generated by dividing the frequency of the 12.8 MHz signals. Windows PC is triggered by this timing marker to record the data with a sampling rate of 64 Hz. The time accuracy of this system controlled by GPS is $\sim$200 ns, which is suitable to investigate phase difference of multi-point observation of Pc1 geomagnetic pulsations which have a period of 0.2-5.0 s.

2.1.2 Calibration

We calibrated the sensitivity, phase differences, and polarity at 0.1-50 Hz of four induction magnetometers for low latitudes using a calibration facility shown in Figure 2.4. The induction magnetometer sensors measure the magnetic fluctuations generated by the AC oscillator and the calibration coil with a resistance R of 10 $k\Omega$. The output sensor signals amplified by two amplifiers are put into the phase difference detector and the oscilloscope. The sensitivity V/nT is obtained by dividing the output voltages by the magnetic field strength ($\sim$100 nT) imposed on the sensor. The diameter, length, and the number of turns of the calibration coil are 0.4 m, 2.0 m, and 100 turns/m, respectively.

Figure 2.4: Calibration system of the induction magnetometer.

2.1.2.1 Sensitivity and phase difference

The magnetic field is inducted in the calibration coil when voltage V (volts) are applied by the AC oscillator. The relation between current I (A) and magnetic field B (nT) is derived by assuming an infinitly-long solenoidal coil as:

$$I = \frac{B}{n\mu_0}, \tag{2.1}$$

where μ_0 is the permeability of vacuum ($\mu_0 = 1.256 \times 10^{-6}$ H/m). The target value B is set to be 100 nT. Then V is derived from Ohm's law with a circuit resistance R (Ω).

$$V = IR = \frac{B \cdot R}{n\mu_0} \tag{2.2}$$

The actual voltage V_a used for calibration is slightly different from these calculated voltages because of the setting accuracy of the AC oscillator. The actual current intensity I_a is,

$$I_a = \frac{V_a}{R}. \tag{2.3}$$

Then the actual magnetic field B_a generated in the coil is,

$$B_a = n\mu_0 I_a = \frac{n\mu_0 V}{R}. \tag{2.4}$$

In case of the magnetometer system for MGD, for example, the AC oscillator generates voltages to provide 100 nT in the coil with n= 100 turns/m. This coil has a resistance of 10 kΩ. From equation 2.2,

$$V = \frac{100 \times 10^{-9} \cdot 10.03 \times 10^3}{100 \cdot 1.256 \times 10^{-6}} = 7.961 \text{ (V)}. \tag{2.5}$$

Actually, $V_a = 8.141$ is applied by the AC oscillator. From equation 2.4,

$$B_a = \frac{100 \cdot 1.256 \times 10^{-7} \cdot 8.161}{10 \times 10^3} = 99.792 \text{ (nT)}. \tag{2.6}$$

By changing the frequency of the AC oscillator, we obtain the frequency-dependence of the magnetometer sensitivity, and the phase delay between the input magnetic field and the magnetometer output voltage. Figure 2.5 shows the frequency dependence of the sensitivities for the induction magnetometers at five stations, MGD, PTK, MSR, STA and ATH. The turnover frequencies are 1.7 Hz for MGD,
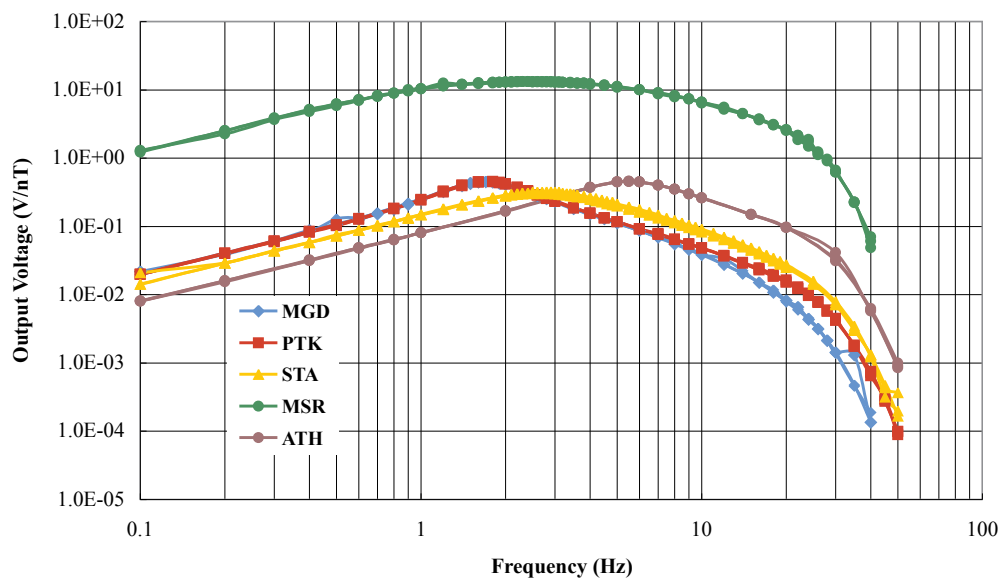
Figure 2.5: Sensitivities of the induction magnetometers at MGD (blue), PTK (red), MSR (green), STA (yellow), and ATH (purple). H-, D-, and Z-components are overplotted in the same color.

1.8 Hz for PTK, 2.2-2.9 Hz for MSR, 1.9-2.7 Hz for STA, and 5.5 Hz for ATH. The sensitivities are 0.450 V/nT for MGD, 0.450 V/nT for PTK, 13.2 V/nT for MSR, 0.291 V/nT for STA, and 0.455 V/nT at the turnover frequencies. For the

induction magnetometer at MSR, the sensitivity for the magnetometer is larger and the curve of sensitivity is smoother than the other stations. The induction magnetometers at MGD and PTK have the same specification and the sensitivity curves are almost identical. For the lower frequency range than the turnover frequency, the output voltages are proportional to dB/dt as expected the induction coil characteristics.

Figure 2.6 shows the frequency dependence of the phase differences for the induction magnetometers at four stations, MGD, PTK, MSR, and STA. We did not calibrate the phase differences of the magnetometer at ATH. The phase differences
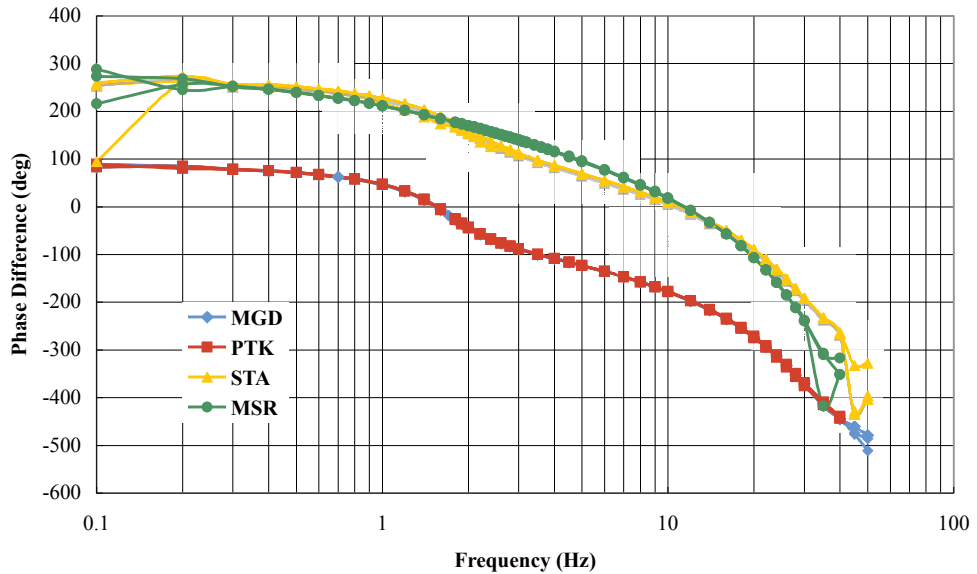
Figure 2.6: Phase differences between input magnetic field fluctuations and output signals of induction magnetometers at MGD (blue), PTK (red), MSR (green), and STA (yellow). H-, D-, and Z-components are overplotted in the same color.

are equal to zero near the turnover frequencies. For the induction magnetometer at MSR, the phase difference is $\sim \pi$ radian different from that of the other stations, because of the opposite polarity of the magnetometer. As shown in Figures 2.5 and 2.6, the frequency dependence of the sensitivities and the phase differences for H-, D-, and Z-components are almost identical at the frequency range of Pc1 pulsations (0.2-5.0 Hz) for low-latitudinal stations. Therefore these magnetometers are suitable to study the polarization characteristics of the Pc1 geomagnetic pulsations.

2.1.2.2 Polarity

In order to check the polarity of the magnetometers, a dry battery cell (1.5 V) was connected to the calibration coil to produce a temporal increase of the magnetic field in the coil. If the output signal from the magnetometer deviates to plus (minus) for the increasing magnetic field in the direction from the sensor connector to the other end of the sensor, the polarity is defined as positive (negative). In the present study, the relation between the magnetometer sensor and the direction of magnetic field fluctuations is important because if the polarity is opposite then the phase difference differs $\pm\pi$. The polarities for the five magnetometers are identical except for those at MSR and ATH, which have a negative polarity.

2.1.2.3 Gain

The main amplifier of the magnetometer has a gain volume which can change the magnetometer sensitivity discretely. To calibrate the gain volume, the AC oscillator generates magnetic field oscillations in the calibration coil at a fixed frequency. Eight gain scales are calibrated with an input voltage of 8.161 V ($\sim$100 nT oscilation) at a frequency of 0.2 Hz for scales 5-7 and 2.0 Hz for scales 1-4. Tables 2.2 and 2.3 show that signals are amplified 1, 2, 5, 10, 20, 50, 250, and 2500 times in order according to the gain scales.

2.2 All-sky Imager

Figure 2.7 shows the all-sky camera system installed at ATH. The highly sensitive

Table 2.2: Gain scales with an input voltage of 8.161 V ($\sim$100 nT) and a frequency of 2.0 Hz of the AC oscillator. H_M, D_M, and Z_M are for MGD, H_P, D_P, and Z_P are for PTK, and H_S, D_S, and Z_S are for STA. These values indicate the factors of output voltages compared with that at the gain scale 1.

gain scales	H_M	D_M	Z_M	H_P	D_P	Z_P	H_S	D_S	Z_S
1	1.00	1.00	1.00	-	1.00	1.00	1.00	1.00	1.00
2	2.10	1.90	1.00	-	1.90	2.00	2.10	2.00	2.00
3	5.10	5.10	4.70	-	4.80	5.00	4.60	5.10	4.60
4	10.3	10.2	9.40	-	9.60	9.90	9.30	10.0	9.10
5	20.2	20.2	18.6	-	19.3	20.0	18.0	20.0	18.3

Table 2.3: Gain scales with an input voltage 8.161 V ($\sim$ 100 nT) and a frequency of 0.2 Hz of the AC oscillators. These values indicate the factors of output voltages compared with that at the gain scale 5.

gain scales	H_M	D_M	Z_M	H_P	D_P	Z_P	H_S	D_S	Z_S
5	1.00	1.00	1.00	-	-	1.00	1.00	1.00	1.00
6	2.50	2.50	2.50	-	-	2.50	2.40	2.60	2.40
7	5.00	4.90	5.10	-	-	5.00	4.70	5.10	4.80
8	9.70	9.60	10.0	-	-	10.0	9.50	12.2	9.60
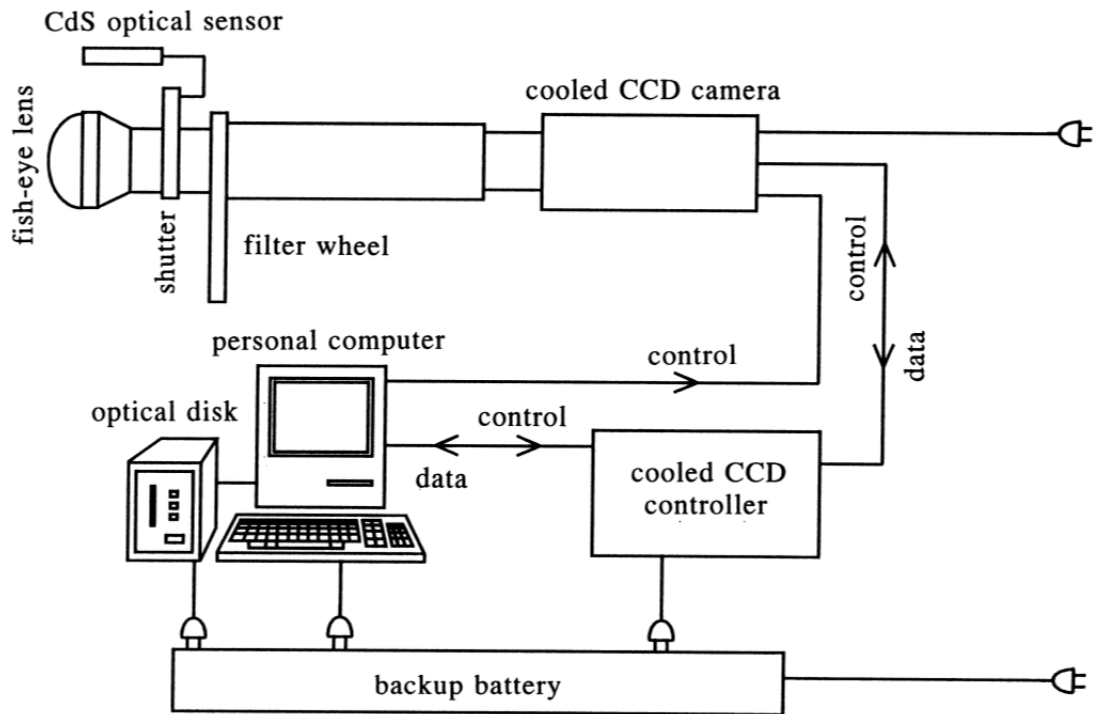
Figure 2.7: All-sky camera system (after Shiokawa et al. [1999])

all-sky camera is one of the Optical Mesosphere Thermosphere Imagers (OMTIs) (Shiokawa et al. [1999], Shiokawa et al. [2009]). The camera records OI (557.7 nm, 630.0 nm), H$_\beta$ (486.1 nm), Na (589.3 nm) emissions with a time resolution of 2 min, and OH-band (720-910 nm) and OI (894.6 nm) emissions with a time resolution of 10 min. The exposure times used to obtain 557.7 nm and 486.1 nm images are 5 s and 40 s, respectively.

2.3   Analysis method

In this section, we describe how the spectrum parameters (coherence and cross spectrum) and the polarization parameters (polarization angle, degree of polarization, and polarization sense) are calculated. The spectrum parameters are obtained by the method described by Hino [1977]. The polarization parameters were obtained by the method developed by Fowler et al. [1967]. We also shows a result of the polarization analysis using artificial waves with a frequency range of 0.0-1.0 Hz and a sampling rate of 64 Hz.

2.3.1   Coherence and cross spectrum

The cross-correlation function $C_{xy}(t)$ between the two time series $x(t)$ and $y(t)$ is given as:

$$C_{xy}(t) = \overline{x(t)y(t+\tau)}, \tag{2.7}$$

where τ is the time lag and the horizontal bar indicates the ensemble average. The cross spectrum $S_{xy}(\omega)$ is defined by the Fourier transform of $C_{xy}(t)$,

$$S_{xy}(\omega) = \frac{1}{2\pi}\int_{-\infty}^{\infty} C_{xy}(t)e^{-i\omega t}\mathrm{dt} \tag{2.8}$$

$$C_{xy}(t) = \int_{-\infty}^{\infty} S_{xy}(t)e^{i\omega t}\mathrm{d}\omega. \tag{2.9}$$

The cross spectrum contains information of argument difference between two signals. Below we show mathematical explanation of the cross spectrum. Fourier

integral expressions of $x(t)$ and $y(t)$ are,

$$x(t) = \int_{-\infty}^{\infty} X(\omega)e^{i\omega t}\mathrm{d}\omega \tag{2.10}$$

$$y(t) = \int_{-\infty}^{\infty} Y(\omega)e^{i\omega t}\mathrm{d}\omega \tag{2.11}$$

$$X(\omega) = \frac{1}{2\pi} \int_{-\infty}^{\infty} x(t)e^{-i\omega t}\mathrm{d}t \tag{2.12}$$

$$Y(\omega) = \frac{1}{2\pi} \int_{-\infty}^{\infty} y(t)e^{-i\omega t}\mathrm{d}t \tag{2.13}$$

The vector representation of equation 2.12 is,

$$X(\omega) = |X(\omega)|e^{i\theta_x(\omega)}, \tag{2.14}$$

where $\theta_x(\omega)$ is the argument. We can consider equation 2.10 as the superposition of the vectors such as equation 2.14 for all range of the angular frequency. Then equation 2.10 is expressed as,

$$
\begin{aligned}
x(t) &= \int_{-\infty}^{\infty} X(\omega)e^{i\omega t}\mathrm{d}\omega \\
&= \int_{-\infty}^{\infty} |X(\omega)|e^{i\theta_x(\omega)} \cdot e^{i\omega t}\mathrm{d}\omega \\
&= \int_{-\infty}^{\infty} |X(\omega)|e^{i(\theta_x(\omega)+\omega t)}\mathrm{d}\omega. \tag{2.15}
\end{aligned}
$$

Since $x(t)$ and $y(t)$ are the real functions,

$$
\begin{aligned}
x(t) &= R_e\left[\int_{-\infty}^{\infty} |X(\omega)|e^{i(\theta_x(\omega)+\omega t)}\mathrm{d}\omega\right] \\
&= \int_{-\infty}^{\infty} |X(\omega)| \cos\left(\theta_x(\omega)+\omega t\right)\mathrm{d}\omega, \tag{2.16}
\end{aligned}
$$

$$y(t) = \int_{-\infty}^{\infty} |Y(\omega)| \cos\left(\theta_y(\omega)+\omega t\right)\mathrm{d}\omega. \tag{2.17}$$

The relation between the two vectors, $X(\omega)$ and $Y(\omega)$, can be expressed as the argument difference $\theta_{xy}(\omega) = \theta_x(\omega) - \theta_y(\omega)$. Figure 2.8 shows $X(\omega)$ and $Y(\omega)$ in the complex space. These two vectors rotate in a period T with conserving a

constant value $\theta_{xy}(\omega)$.
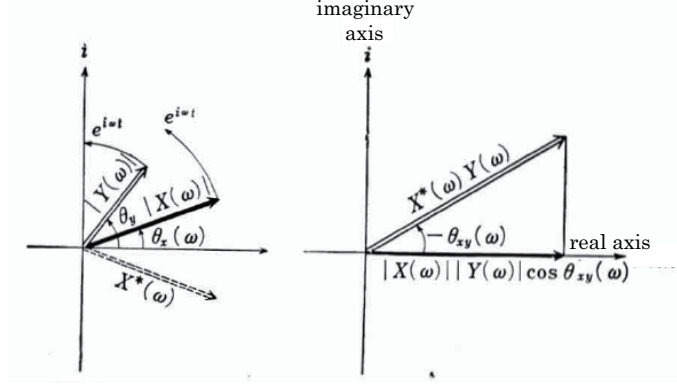
Figure 2.8:   Relation between $X(\omega)$ and $Y(\omega)$ in the complex space.

The product of the conjugate vector of X, X^* and Y contains $\theta_{xy}(\omega)$ as expressed in equations 2.16 and 2.17.

$$X^*(\omega)Y(\omega) = |X(\omega)||Y(\omega)|e^{i(\theta_y(\omega)-\theta_x(\omega))} = |X(\omega)||Y(\omega)|e^{-i\theta_{xy}(\omega)} \qquad (2.18)$$

Thus X^*Y can be an index of the argument difference, the cross spectrum. The spectrum $S_{xy}(\omega)$ is expressed by,

$$\begin{aligned} S_{xy}(\omega) &= \frac{2\pi}{T}\mathrm{E}\left[X^*(\omega)Y(\omega)\right] \\ &= \frac{2\pi}{T}\mathrm{E}\left[|X(\omega)||Y(\omega)|e^{-i\theta_{xy}(\omega)}\right], \end{aligned} \qquad (2.19)$$

where T is the time segment and E denotes the ensemble average. The term $2\pi/T$ is multiplied in order to express $S_{xy}(\omega)$ in unit of the power spectrum density. The cross spectrum is represented as a complex function and is difficult to understand in the real world. Therefore, the coherence $\mathrm{coh}_{xy}(\omega)$ is introduced and is defined as:

$$\mathrm{coh}_{xy}(\omega)^2 = \frac{|S_{xy}(\omega)|^2}{S_{xx}(\omega)S_{yy}(\omega)}, \qquad (2.20)$$

where $S_{xx}(\omega)$ and $S_{yy}(\omega)$ are the power spectrum density for time series $x(t)$ and $y(t)$, respectively. Equation 2.20 indicates that if $\mathrm{coh}_{xy}(\omega)$ is equal to 1, two signals are identical and if $\mathrm{coh}_{xy}(\omega)$ is equal to 0, two signals have no correlation.

Therefore,

$$0 \leq \mathrm{coh}_{xy}^2(\omega) \leq 1. \tag{2.21}$$

The coherence shows the correlation between two signals. The larger the coherence indicates more correlation between the two signals. In this thesis, the coherence between H- and D-components of induction magnetometer data is calculated in order to distinguish signals due to geomagnetic pulsations from random noises which do not have correlation between the two components.

From equation 2.20, the cross-spectrum of discrete time series, $x(t)$ and $y(t)$, is defined as:

$$\begin{aligned} P_{xy}(f) &= \frac{1}{T}\mathrm{E}\left[X^*(f)Y(f)\right] \\ &= \frac{T^2}{N}\mathrm{E}\left[(A_x + iB_x)(A_y - iB_y)\right]. \end{aligned} \tag{2.22}$$

where A_x and B_x are real and imaginary parts of the Fourier coefficients, respectively, for the time series $x(t)$ obtained by the Fast Fourier Transform (FFT). Thus, the coherence is calculated from equations 2.20 and 2.22 as:

$$\mathrm{coh}_{xy}(f) = \frac{|P_{xy}(f)|}{\sqrt{P_x(f)P_y(f)}}. \tag{2.23}$$

2.3.2 Polarization

Fowler et al. [1967] have developed a method of polarization analysis based on the principle of statistical optics as applied to the quasi-monochromatic wave theory. Their analysis allows to investigate signals without noises by separating totally polarized signals from unpolarized noises. They showed that this analysis is more useful than the ordinary hodogram analysis, which vary considerably and can be interpreted only as an average value over the whole signals. In this section, we describe the polarization analysis method adopted in this thesis, based on Fowler et al. [1967]. They defined a quasi-monochromatic wave as:

$$\Delta\nu/\bar{\nu} \ll 1, \tag{2.24}$$

where $\Delta\nu$ is the frequency band width and $\bar{\nu}$ is the mean signal frequency. We

assume this condition can be applied to the present analysis of Pc1 pulsations. To derive the polarization matrix, we first introduce the coherence matrix $\mathbf{J}$ as:

$$\mathbf{J} = \begin{pmatrix} <H_x H_x^*> & <H_x H_y^*> \\ <H_y H_x^*> & <H_y H_y^*> \end{pmatrix}, \tag{2.25}$$

where H_x and H_y are the orthogonal components of Fourier transform of H- and D-component of magnetic field variations, respectively. The sharp brackets denote time averages, and the asterisks denote the complex conjugates. The general form of H_x and H_y are given as:

$$\begin{aligned} H_x(t) &= A_1(t)\exp\{i[\bar{\omega}t + \phi_1(t)]\} \\ H_y(t) &= A_2(t)\exp\{i[\bar{\omega}t + \phi_2(t)]\}, \end{aligned} \tag{2.26}$$

where $\bar{\omega} = 2\pi\bar{\nu}$, $A_1(t)$ and $A_2(t)$ are amplitudes, $\phi_1(t)$ and $\phi_2(t)$ are phases.

When the fluctuations are totally polarized, A_1, A_2, ϕ_1, and ϕ_2 become constants and $\mathbf{J}$ can be expressed with these values.

$$\mathbf{J} = \begin{pmatrix} A_1^2 & A_1 A_2 e^{i(\phi_1 - \phi_2)} \\ A_1 A_2 e^{-i(\phi_1 - \phi_2)} & A_2^2 \end{pmatrix} \tag{2.27}$$

The determinant of this matrix is zero for totally-polarized waves.

$$\det|\mathbf{J}| = A_1^2 \cdot A_2^2 - A_1 A_2 e^{i(\phi_1 - \phi_2)} \cdot A_1 A_2 e^{-i(\phi_1 - \phi_2)} = 0. \tag{2.28}$$

The composition of the signal strength $\mathrm{T_r}$ is,

$$\mathrm{T_r}[\mathbf{J}] = A_1^2 + A_2^2. \tag{2.29}$$

The coherence matrix of a real phenomenon $\mathbf{J}$, which is a resultant of several signals, can be regarded as the sum of the individual signals. Consider to separate signals of the observation data of the induction magnetometers into the totally polarized and unpolarized elements $\mathbf{P}$ and $\mathbf{U}$.

$$\mathbf{J} = \mathbf{P} + \mathbf{U} \tag{2.30}$$

$\mathbf{J}$ is the Hermitian matrix as shown in equation 2.27. Then $\mathbf{P}$ is also the Hermitian matrix from equation 2.30.

$$\mathbf{P} = \begin{pmatrix} A & B \\ B^* & C \end{pmatrix} \tag{2.31}$$

For the totally polarized signals,

$$\det|\mathbf{P}| = AC - BB^* = 0. \tag{2.32}$$

Then we write unpolarized signals $\mathbf{U}$ as,

$$\mathbf{U} = \begin{pmatrix} U_{xx} & U_{xy} \\ U_{xy}^* & U_{yy} \end{pmatrix} \tag{2.33}$$

The coherence of two signals μ_{xy} is zero because "unpolarized" means that the signals have no correlations each other.

$$\mu_{xy} = \frac{|U_{xy}|}{\sqrt{U_{xx}U_{yy}}} = 0$$

Thus,

$$U_{xy} = U_{xy}^* = 0. \tag{2.34}$$

The components of matrixes are average value and we can put a constant real value D for U_{xx} and U_{yy}.

$$U_{xx} = U_{yy} = D \tag{2.35}$$

Therefore,

$$\mathbf{U} = \begin{pmatrix} D & 0 \\ 0 & D \end{pmatrix}. \tag{2.36}$$

From equation 2.30,

$$\begin{pmatrix} J_{xx} & J_{xy} \\ J_{yx} & J_{yy} \end{pmatrix} = \begin{pmatrix} A & B \\ B^* & C \end{pmatrix} + \begin{pmatrix} D & 0 \\ 0 & D \end{pmatrix}. \tag{2.37}$$

By comparing each component of equation 2.38, we obtain,

$$\begin{aligned} A + D &= J_{xx} \\ B &= J_{xy} \\ B^* &= J_{yx} \\ C + D &= J_{yy} \end{aligned} \tag{2.38}$$

$$\begin{aligned} A &= J_{xx} - D \\ B &= J_{xy} \\ B^* &= J_{yx} \\ C &= J_{yy} - D \end{aligned} \tag{2.39}$$

By substituting equation 2.39 to equation 2.32, and we obtain the quadric equation for D.

$$\begin{aligned} AC - BB^* &= 0 \\ (J_{xx} - D)(J_{yy} - D) - J_{xy}J_{yx} &= 0 \\ J_{xx}J_{yy} - D(J_{xx} + J_{yy}) + D^2 - J_{xy}J_{yx} &= 0 \\ D^2 - D(J_{xx} + J_{yy}) + (J_{xx}J_{yy} - J_{xy}J_{yx}) &= 0 \end{aligned}$$
$$\tag{2.40}$$

By solving equation 2.40,

$$\begin{aligned} D &= \frac{1}{2} \left\{ (J_{xx} + J_{yy}) \pm \sqrt{(J_{xx} + J_{yy})^2 - 4(J_{xx}J_{yy} - J_{xy}J_{yx})} \right\} \\ &= \frac{1}{2} \left\{ (J_{xx} + J_{yy}) \pm \sqrt{(J_{xx} + J_{yy})^2 - 4|\mathbf{J}|} \right\}. \end{aligned} \tag{2.41}$$

Then the totally polarized components are written as:

$$\mathbf{P} = \begin{pmatrix} P_{xx} & P_{xy} \\ P_{yx} & P_{yy} \end{pmatrix} = \begin{pmatrix} J_{xx} - D & J_{xy} \\ J_{yx} & J_{yy} - D \end{pmatrix} = \begin{pmatrix} A & B \\ B^* & C \end{pmatrix}. \tag{2.42}$$

Here, the composition of the signal strength for $\mathbf{P}$ is,

$$
\begin{aligned}
\mathrm{T_r}[\mathbf{P}] &= P_{xx} + P_{yy} \\
&= (J_{xx} - D) + (J_{yy} - D) \\
&= J_{xx} + J_{yy} - 2D \\
&= J_{xx} + J_{yy} - 2 \cdot \frac{1}{2} \left\{ (J_{xx} + J_{yy}) - \sqrt{(J_{xx} + J_{yy})^2 - 4|\mathbf{J}|} \right\} \\
&= \sqrt{(J_{xx} + J_{yy})^2 - 4|\mathbf{J}|}.
\end{aligned}
\tag{2.43}
$$

The strength ratio of the totally polarized and unpolarized signals R is,

$$
\begin{aligned}
R = \frac{T_r[\mathbf{P}]}{T_r[\mathbf{J}]} &= \frac{\sqrt{(J_{xx} + J_{yy})^2 - 4|\mathbf{J}|}}{J_{xx} + J_{yy}} \\
&= \sqrt{1 - \frac{4|\mathbf{J}|}{(J_{xx} + J_{yy})^2}}.
\end{aligned}
\tag{2.44}
$$

R is used as the degree of the polarization.

The general formula of a ellipse is,

$$\frac{x^2}{a} + \frac{y^2}{b} = 1, \tag{2.45}$$

Equation 2.45 is represented in the matrix form,

$$\begin{pmatrix} y & x \end{pmatrix} \begin{pmatrix} a & 0 \\ 0 & b \end{pmatrix} \begin{pmatrix} y \\ x \end{pmatrix} = ab. \tag{2.46}$$

The coherence matrix can be also expressed like equation 2.46,

$$\begin{pmatrix} y & x \end{pmatrix} \begin{pmatrix} P_{xx} & P_{xy} \\ P_{xy}^* & P_{yy} \end{pmatrix} \begin{pmatrix} y \\ x \end{pmatrix} = P_{xx}P_{yy}. \tag{2.47}$$

Then, by expanding equation 2.47, we obtain,

$$\left(\begin{array}{cc} P_{xx}y + P_{xy}^*x & yP_{xy} + xP_{yy} \end{array} \right) \left(\begin{array}{c} y \\ x \end{array} \right) = P_{xx}P_{yy}$$

$$P_{xx}y^2 + P_{xy}^*xy + P_{xy}xy + P_{yy}x^2 = P_{xx} + P_{yy}$$

$$\frac{x^2}{P_{xx}} + \frac{2\mathrm{R_e}P_{xy}}{P_{xx}P_{yy}} \cdot xy + \frac{y^2}{P_{yy}} = 1. \tag{2.48}$$

The second term of equation 2.47 indicates that the ellipse expressed in this equation is rotated by a certain degree θ with the origin of the coordinate system (x, y). In order to solve θ, we introduce the rotation matrix T as:

$$T = \left(\begin{array}{cc} \cos\theta & -\sin\theta \\ \sin\theta & \cos\theta \end{array} \right). \tag{2.49}$$

When the ellipse is rotated by θ, θ should satisfy the following equation.

$$\left(\begin{array}{cc} \cos\theta & \sin\theta \\ -\sin\theta & \cos\theta \end{array} \right) \left(\begin{array}{cc} P_{xx} & P_{xy} \\ P_{xy}^* & P_{yy} \end{array} \right) \left(\begin{array}{cc} \cos\theta & -\sin\theta \\ \sin\theta & \cos\theta \end{array} \right) = \left(\begin{array}{cc} Q_{xx} & 0 \\ 0 & Q_{yy} \end{array} \right), \tag{2.50}$$

where Q_{xx} and Q_{yy} are the length of minor and major principle axes for a new coordinate system (x', y') after the rotation T. Two equations are obtained by expanding equation 2.50.

$$P_{xx}\sin\theta\cos\theta - P_{xy}^*\sin^2\theta + P_{xy}\cos^2\theta - P_{yy}\sin\theta\cos\theta = 0$$

$$P_{xx}\sin\theta\cos\theta - P_{xy}^*\cos^2\theta + P_{xy}\sin^2\theta - P_{yy}\sin\theta\cos\theta = 0 \tag{2.51}$$

By considering the trigonometrical functions,

$$\frac{1}{2}P_{xx}\sin 2\theta - (\mathrm{R_e}P_{xy} - \mathrm{I_m}P_{xy}\sin^2\theta) + (\mathrm{R_e}P_{xy} - \mathrm{I_m}P_{xy}\sin^2\theta)\cos^2\theta - \frac{1}{2}P_{yy}\sin 2\theta = 0$$

$$\frac{1}{2}P_{xx}\sin 2\theta - (\mathrm{R_e}P_{xy} - \mathrm{I_m}P_{xy}\cos^2\theta) + (\mathrm{R_e}P_{xy} - \mathrm{I_m}P_{xy}\sin^2\theta)\sin^2\theta - \frac{1}{2}P_{yy}\sin 2\theta = 0. \tag{2.52}$$

Equation 2.52 become simpler by factorize into real and imaginary parts of P_{xy}.

$$\frac{1}{2}(P_{xx} - P_{yy})\sin 2\theta + \mathrm{R_e}P_{xy}(\cos^2\theta - \sin^2\theta) + \mathrm{I_m}P_{xy}(\cos^2\theta + \sin^2\theta) = 0$$
$$\frac{1}{2}(P_{xx} - P_{yy})\sin 2\theta + \mathrm{R_e}P_{xy}(\cos^2\theta - \sin^2\theta) - \mathrm{I_m}P_{xy}(\cos^2\theta + \sin^2\theta) = 0$$

$$(2.53)$$

From equation 2.53,

$$(P_{xx} - P_{yy})\sin 2\theta + 2\mathrm{R_e}P_{xy}\cos 2\theta = 0$$
$$\frac{\sin 2\theta}{\cos 2\theta} = \tan 2\theta = \frac{-2\mathrm{R_e}P_{xy}}{P_{xx} - P_{yy}}. \qquad (2.54)$$

Equation 2.54 shows that θ can be obtained from the components of the totally polarized signals.

Then, the ellipticity ϵ is introduced in order to see the sense of the polarization. ϵ is the ratio of the minor and major axis of the ellipse.

$$\epsilon = Q_y/Q_x, \qquad (2.55)$$

where Q_x and Q_y are the length of the principle axis for the ellipse. We define the auxiliary angle β,

$$\tan \beta = Q_y/Q_x. \qquad (2.56)$$

Equations to connect β and the components of $\mathbf{P}$ are as follows.

$$\frac{\sin^2\beta}{\cos^2\beta} = \frac{1}{\cos^2\beta} - 1 = Q_y^2/Q_x^2 \qquad (2.57)$$

$$\cos^2\beta = \frac{Q_x^2}{Q_x^2 + Q_y^2} \qquad (2.58)$$

$$\cos\beta = \frac{Q_x}{\sqrt{Q_x^2 + Q_y^2}} \qquad (2.59)$$

$$\sin\beta \;\; = \;\; \frac{Q_y}{Q_x}\cos\beta = \frac{Q_y}{\sqrt{Q_x^2 + Q_y^2}} \tag{2.60}$$

Here, from the trigonometrical function, equations 2.59 and 2.60 become,

$$\begin{aligned} \sin 2\beta = 2\sin\beta\cos\beta \;\; &= \;\; \frac{2Q_x Q_y}{Q_x^2 + Q_y^2} \\ &= \;\; \frac{-iP_{xy} + iP_{yx}}{P_{xx} + P_{yy}} \\ &= \;\; \frac{2\mathrm{I_m}P_{xy}}{P_{xx} + P_{yy}}. \end{aligned} \tag{2.61}$$

$\sin\beta$ is negative (positive) for clockwise (counterclockwise) rotation of the polarization vector. We can use this value as the sense of polarization.

2.3.3 Polarization analysis for artificial waves

In order to investigate accuracy and reliability of the above procedure of polarization analysis, we analyzed artificially-made sinusoidal waves with a sampling rate of 64 Hz by this procedure. The artificial waves are mixture of waves with frequencies at 0.1 Hz, 0.2 Hz, $\cdots$, 0.9 Hz (every 0.1 Hz), which have the polarization angles of $-40°, -30°, \cdots, 40°$, respectively. Each frequency component has also a random-phase noise with an amplitude of 2 % of the sinusoidal waves. The polarization angle is defined as the angle from the geomagnetic pole (eastward positive).

Figure 2.9 shows the waveforms and hodograms of the input waves for 10 s. The polarization angle was set to be different for different frequencies. Figure 2.10 is the waveform and the hodogram of the composite wave of all these different waves. Since all the waves are mixed, the polarization angle of this composite wave is difficult to determine from the hodogram.

Figure 2.11 shows the result of the spectral and polarization analysis for the composite wave shown in Figure 2.10. The polarization parameters are calculated only when the coherence is higher than 0.5. Although it was not possible to identify the polarization angle from the hodogram, the polarization angle of each frequency is clearly identified by the present analysis. The degree of the
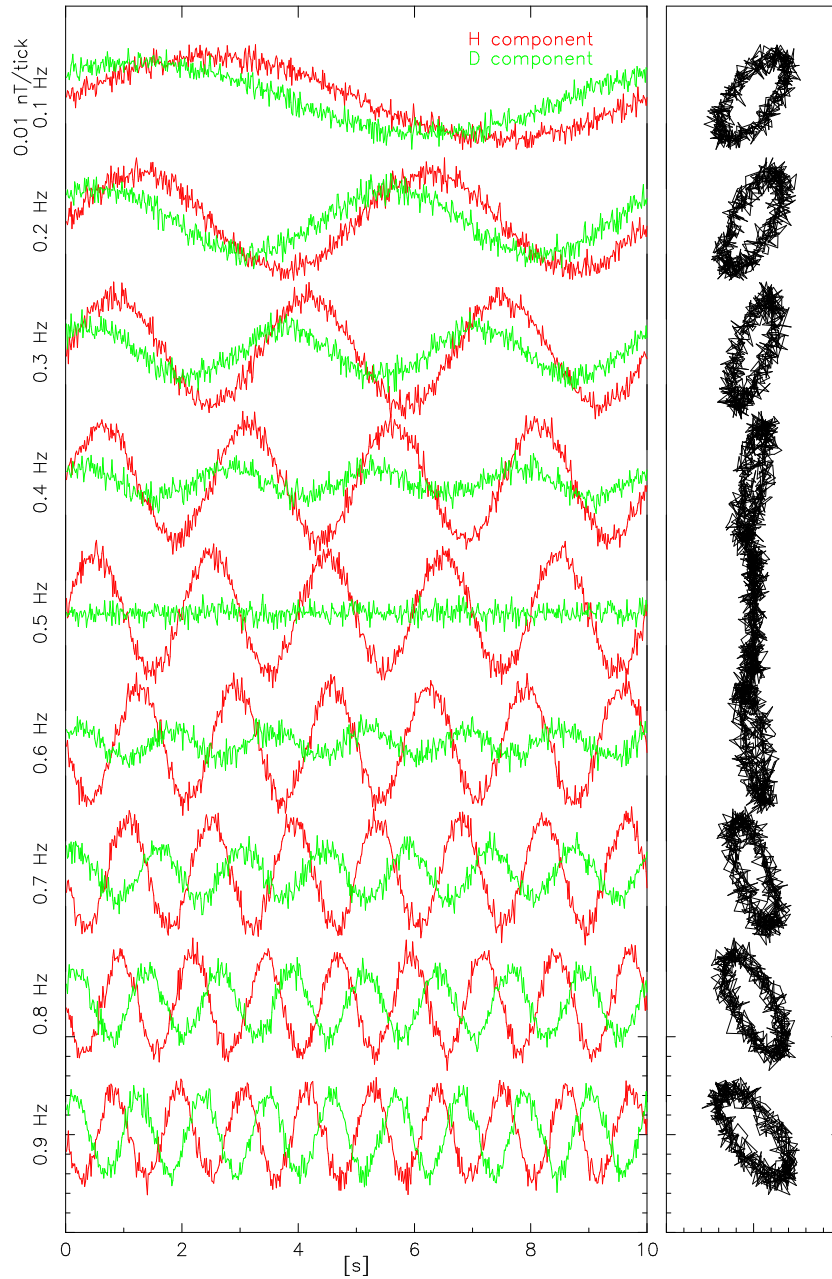
Figure 2.9: Waveforms (left) and hodograms (right) of artificial sinusoidal waves with frequencies of 0.1-0.9 Hz, used as the input signals of the polarization analysis. Red and green curves indicate H- and D-components, respectively.
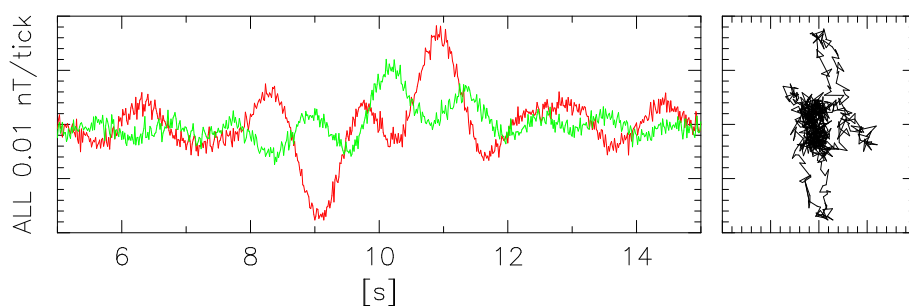
Figure 2.10: Waveform and hodogram of the artificial waves as the input signal of the polarization analysis. This data is obtained by summing all the waves shown in Figure 2.9.

polarization shows ∼ 1 at all the frequencies of the sinusoidal waves, indicating that all components are totally polarized and consistent with the condition of the input artificial waves. The sense of the polarization shows a clockwise rotation for 0.0-0.5 Hz and a counterclockwise for 0.5-1.0Hz wave. This result is also consistent with the information of the input waves.
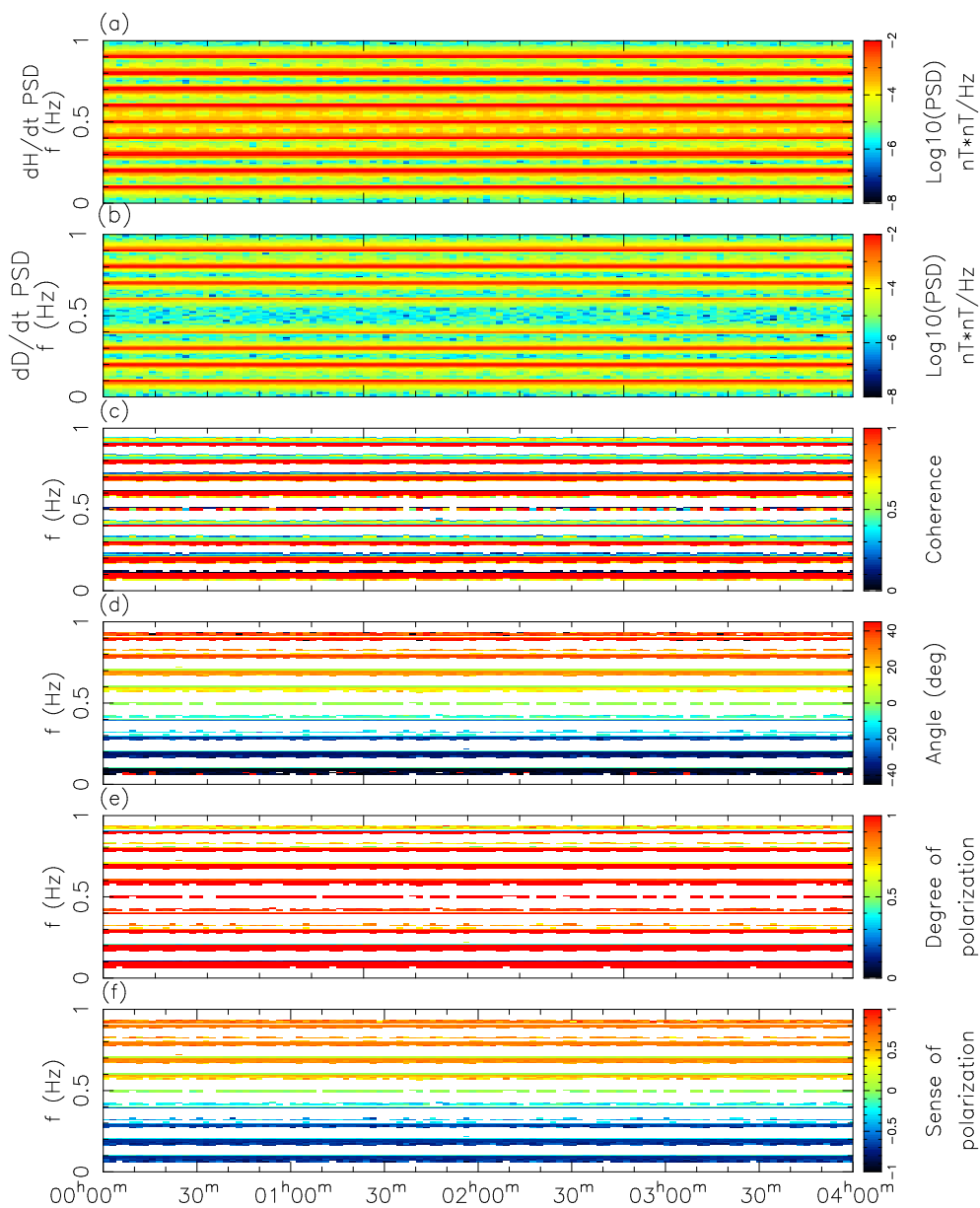
Figure 2.11: Spectral and polarization parameters of the input composite wave shown in Figure 2.10. From top to bottom, power spectrum density of (a) H- and (b) D-component magnetic field, (c) coherence of H and D components, (d) polarization angle, (e) degree of polarization, and (d) sense of polarization. These parameters are calculated by the procedures described in this chapter.

Chapter 3

Pc1 geomagnetic pulsations at low latitudes

3.1 Introduction

In previous studies of Pc1 polarization characteristics observed on the ground, it was implicitly assumed that the polarization parameters within an individual Pc1 wave packet do not depend on frequency. Summers and Fraser [1972] examined the polarization parameters (including polarization ellipse orientation and polarization sense) using hodograms and a narrow-band filter ($\Delta f \sim 0.01$ Hz), and concluded that they did not depend on the Pc1 center frequency. Webster and Fraser [1985] calculated the polarization ellipse orientation averaged over time and frequency by the method of Fowler et al. [1967] for 28 Pc1 events observed at low latitudes and found no relationship between the orientation and the typical Pc1 frequency. Althouse and Davis [1978] studied 18 Pc1 events observed at five middle-latitude ground stations. They showed that polarization parameters obtained using narrow-band filters often varied significantly over time, and only the time-averaged parameters showed the possible ionospheric source location. Erlandson et al. [1990] used the Viking satellite data to show that the polarization parameters of some Pc1 events vary as a function of frequency. Based on these results, Pc1 polarization parameters seem to show frequency dependences only when they are not averaged or filtered on time and frequency. Therefore, it

is important to investigate Pc1 polarization parameters with respect to each frequency component throughout the duration of event to understand the detailed polarization characteristics within each Pc1 band observed on the ground. In this chapter we study the frequency dependence of the polarization parameters (polarization ellipse orientation and polarization sense) within individual Pc1 wave packets detected at three low - latitude stations.

3.2 Observation

We used the low - latitude multipoint induction magnetometers deployed by the Solar Terrestrial Environment Laboratory, Nagoya University. Three induction magnetometers are located at Paratunka (PTK) in Russia, and Moshiri (MSR) and Sata (STA) in Japan. The distances between these stations are 1000-4000 km. The data were recorded at a sampling rate of 64 Hz. The clock of the recording is controlled by GPS receivers which generate a standard time pulse with an accuracy of $\sim \pm 1$ ms. The turnover frequency (1.8-2.9 Hz) and sensitivity of these induction magnetometers were calibrated using a calibration coil with a length of 2 m. The sensitivities and phase differences are almost identical for H, D, and Z components in the frequency range of Pc1 (0.2-5.0 Hz) and are suitable to analyze the polarization characteristics. Details of these induction magnetometers are given by Shiokawa et al. [2010].

3.2.1 Event Analysis

The power spectrum density (PSD) of the two horizontal magnetic field components, H and D, measured by induction magnetometers was calculated by Fast Fourier Transform (FFT) every 30 s with a time window width of 128 s and with a frequency resolution 0.0078 Hz. In each window the polarization parameters (angle of polarization ellipse orientation Ψ, degree of polarization P, and polarization sense ε) are calculated using the relationships from Fowler et al. [1967]. This method of polarization analysis is based on the principle of statistical optics and enables one to separate the polarized part of signals from the unpolarized part. This analysis is more robust and informative than the ordinary hodogram

technique. For the polarized part of signal, the angle of the polarization ellipse orientation Ψ is defined as the positive (negative) angle measured from the magnetic north westward (eastward). The degree of polarization P indicates the ratio of the polarized signal PSD to the total PSD of magnetic field variations. The polarization sense ε ($= \beta$ in equation (7) of Fowler et al. [1967]) is defined as the direction of rotation looking along the local magnetic field direction. Negative and positive signs of ε indicate LH and RH polarization, respectively. The value $\varepsilon = 0$ corresponds to linear polarization.

3.2.1.1 Monotonic frequency dependence of the angle of polarization ellipse orientation (monotonic FDA)

Examples of dynamic spectra and dynamic polarization spectra of clear Pc1 geomagnetic pulsations observed simultaneously at PTK, MSR, and STA at 1400-1800 UT on November 5, 2007 are shown in Figures 3.1, 3.2, and 3.3. Geomagnetic activity is quiet during this event (K_p=0-1). The spectral and polarization characteristics (PSD of H and D components, coherence γ between H and D components, Ψ, P, and ε) are shown from top to bottom. Clear Pc1 emission is observed in the 0.4-0.8 Hz band at all three stations. The characteristics of these dynamic spectra are classified as the combination of diffuse and periodic emissions according to a definition by Fukunishi et al. [1981]. For the frequency range of 0.5-0.6 Hz, the coherence and all the polarization parameters show similar tendencies at the three stations. In the following we describe the characteristics of the plotted parameters in greater detail.

The Pc1 waves are rather noisy at PTK (Figures 3.1a and 3.1b) but less so at MSR (Figures 3.2a and 3.2b). The intensity of PSD at STA (Figures 3.3a and 3.3b) is much weaker than those at the other two stations, probably because of attenuation due to ionospheric duct propagation to lower latitudes.

The coherence γ between the H and D components at PTK is high in the 0.5-0.8 Hz band (Figure 3.1c). The Pc1 emission band at PTK is rather broad because of local noise. The local noise, not evident at other stations, also shows a high γ between H and D components. Ionosondes and some observatory facilities nearby the magnetometer site possibly produce the local noise at PTK. At MSR,
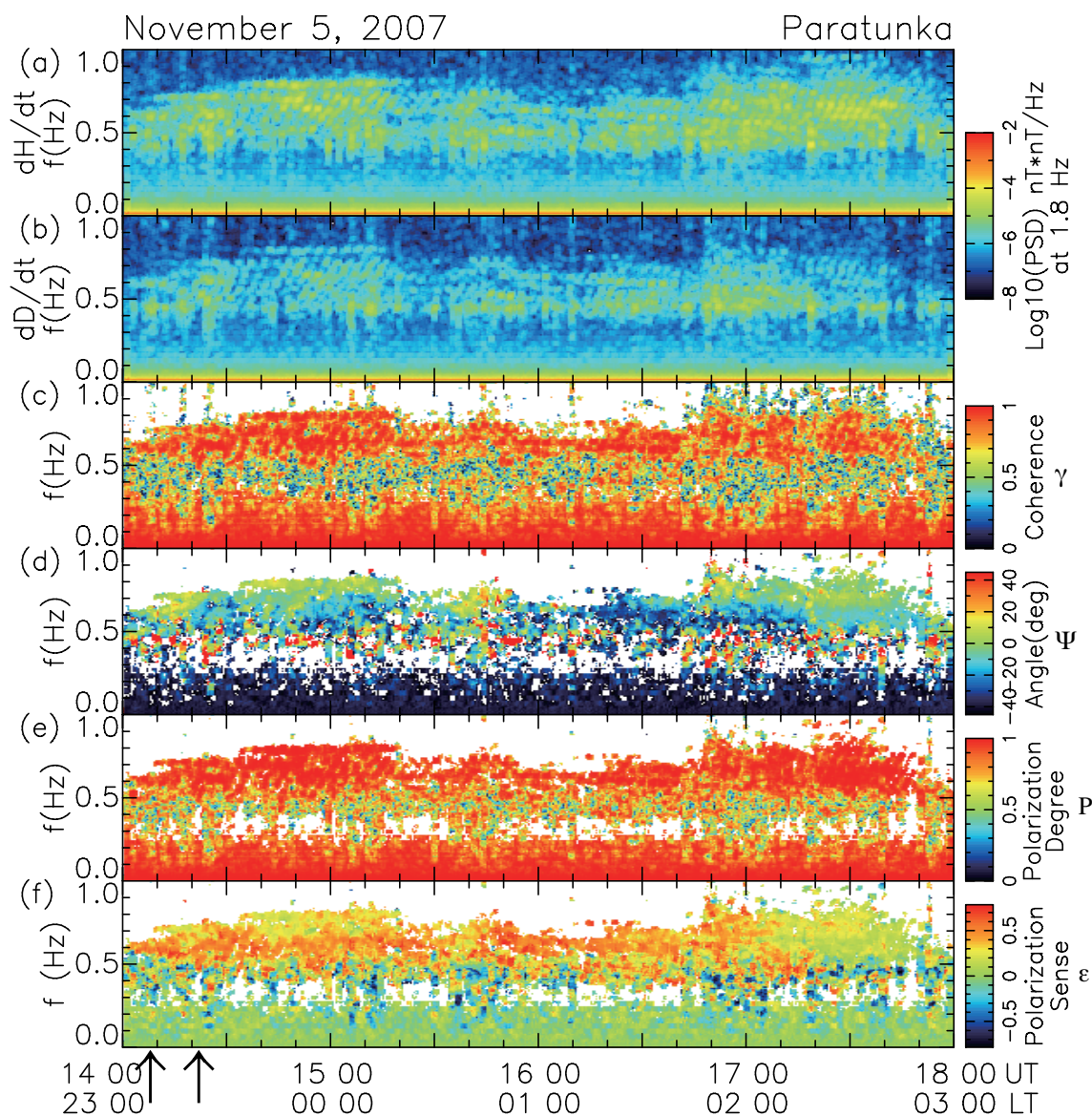
Figure 3.1: The power spectrum density of the (a) H and (b) D components of the magnetic field; (c) coherence, γ, between the H and D components; (d) angle of polarization ellipse orientation Ψ; (e) degree of the polarization P; and (f) polarization sense ε, observed at PTK at 1400-1800 UT (2300-0300 LT) on November 5, 2007 for a frequency range of 0.0-1.0 Hz. The vertical arrows indicate times 1408 UT and 1422 UT for which the waveform of the magnetic field is shown in Figures 3.5 and 3.6.
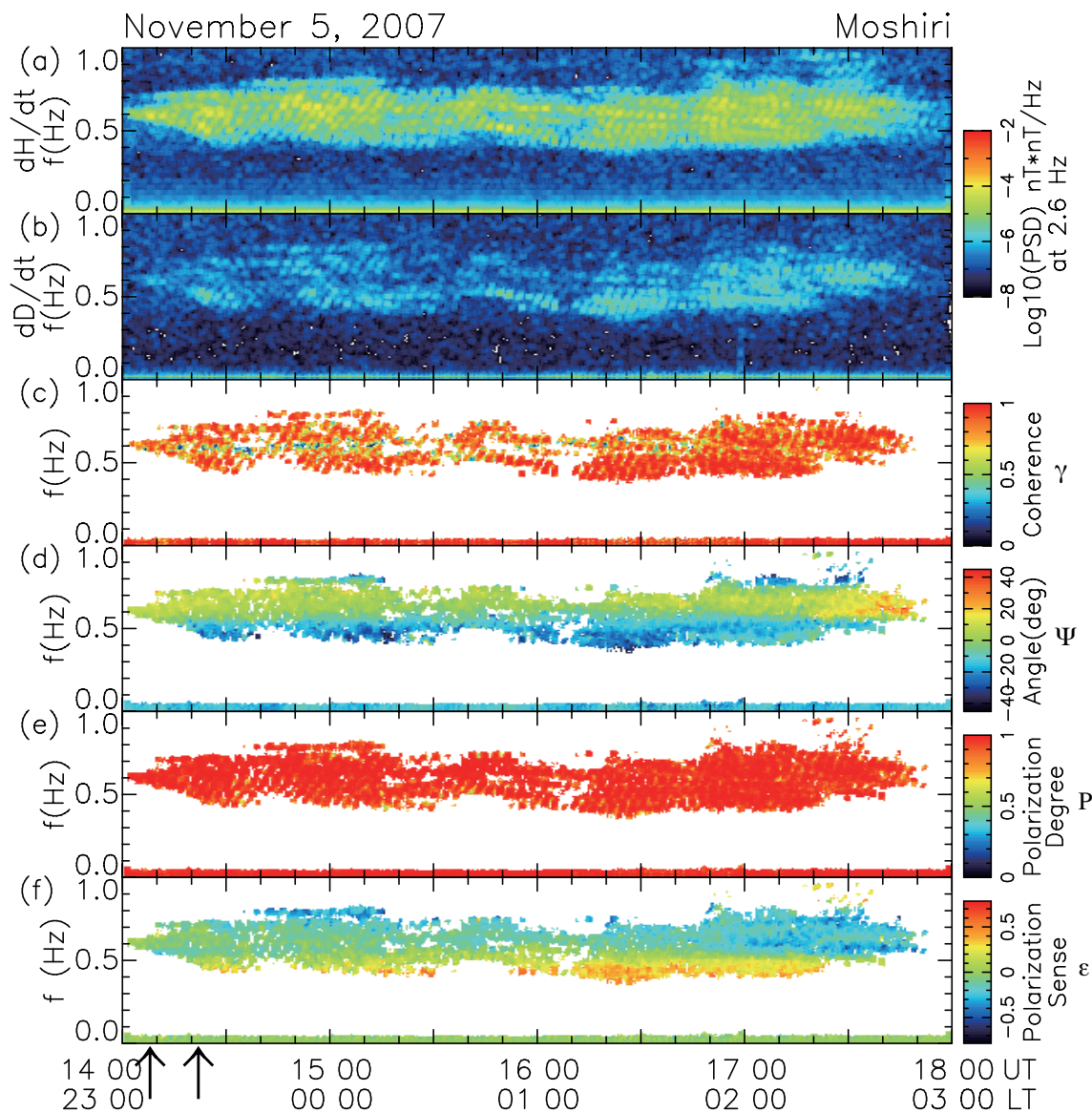
Figure 3.2: The power spectrum density of the (a) H and (b) D components of the magnetic field; (c) coherence, γ, between the H and D components; (d) angle of polarization ellipse orientation Ψ; (e) degree of the polarization P; and (f) polarization sense ε, observed at MSR at 1400-1800 UT (2300-0300 LT) on November 5, 2007 for a frequency range of 0.0-1.0 Hz. The vertical arrows indicate times 1408 UT and 1422 UT for which the waveform of the magnetic field is shown in Figures 3.5 and 3.6.

45
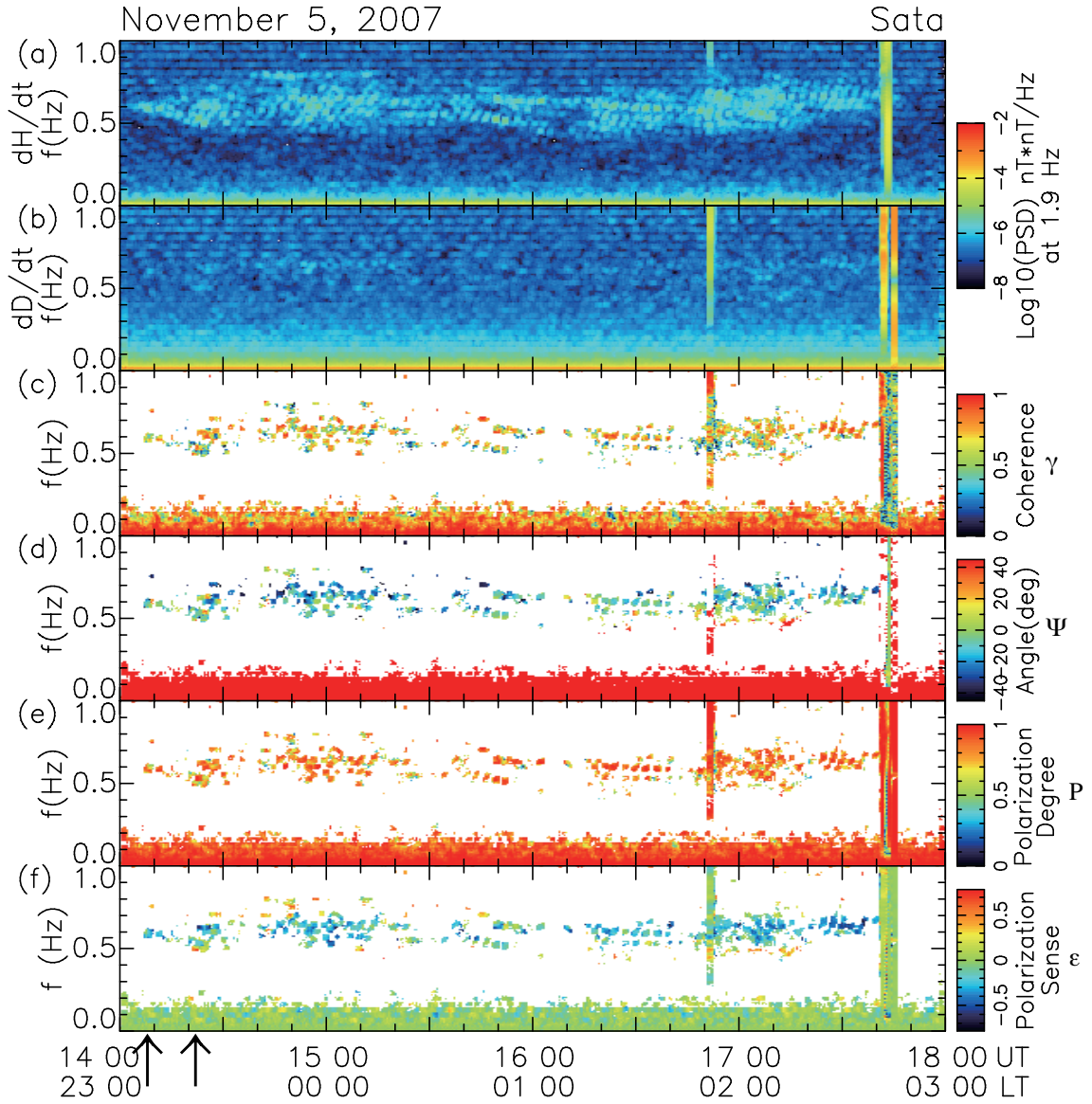
Figure 3.3: The power spectrum density of the (a) H and (b) D components of the magnetic field; (c) coherence, γ, between the H and D components; (d) angle of polarization ellipse orientation Ψ; (e) degree of the polarization P; and (f) polarization sense ε, observed at STA at 1400-1800 UT (2300-0300 LT) on November 5, 2007 for a frequency range of 0.0-1.0 Hz. The vertical arrows indicate times 1408 UT and 1422 UT for which the waveform of magnetic field is shown in Figures 3.5 and 3.6.

46

γ is high in the frequency band where PSD is high (Figure 3.2c). The coherence γ observed at STA is low (Figure 3.3c). Nonetheless, a band of high γ at 0.5-0.8 Hz, corresponding to the Pc1 range observed at other two stations, can be identified. Figure 3.1e shows that both the Pc1 waves and the local noise at lower frequencies observed at PTK are highly polarized. The degree of polarization P observed at MSR is high in the frequency range where PSD is high (Figure 3.2e). The signal at STA is highly polarized at the frequencies where γ is high (Figure 3.3e).

The angle of the polarization ellipse orientation, Ψ, observed at MSR is frequency-dependent (Figure 3.2d): Ψ increases from $\sim$-20° to $\sim$+20° with the increase of f from 0.4 to 0.8 Hz. At PTK (Figure 3.1d), Ψ is significantly affected by local noise, but one can still identify a variation of $\Psi(f)$ which is similar to that of MSR. We call this type of Pc1 event "monotonic Frequency Dependence of the Angle of polarization ellipse orientation (monotonic FDA)" because the angle Ψ varies monotonically with frequency. The frequency dependence at STA is not particularly clear because of the small amplitudes (Figure 3.3d). Nevertheless, one can see Ψ $\sim$-20° at around 0.6 Hz, which is consistent with the $\Psi(f)$ dependence at other stations.

At PTK polarization is RH (ε >0) over almost the entire frequency band of Pc1 (Figure 3.1f). At MSR the polarization clearly changes from RH to LH with increasing frequency (Figure 3.2f). At STA LH polarization is mostly observed (Figure 3.3f). Thus, there is a tendency for the observed polarization sense to change from RH (at PTK) to LH at lower latitudes (MSR and STA).

Figures 3.4a-3.4f show same parameters as those shown in Figure 3.2 at 1423:30-1425:38 UT at MSR with the frequency in the horizontal axis with a resolution of 0.0078 Hz. In Figure 3.4a, we can see a continuous band at frequencies of 0.45-0.75 Hz with high PSD. There are 3 peaks of PSD at 0.55 Hz, 0.63 Hz and 0.73 Hz. The number of these peaks varies temporally from 0 to 5 during this Pc1 event. The frequencies for these peaks also change temporally. The coherence γ between H and D components are over 0.7 except at $\sim$0.6 Hz. Since the amplitude in D component magnetic field variation was quite small at $\sim$0.6 Hz, γ is low. The polarization degree P indicates $\sim$1 for the Pc1 band (Figure 3.4e). In Figures 3.4d and 3.4f, we can see the frequency dependence of Ψ and ε,
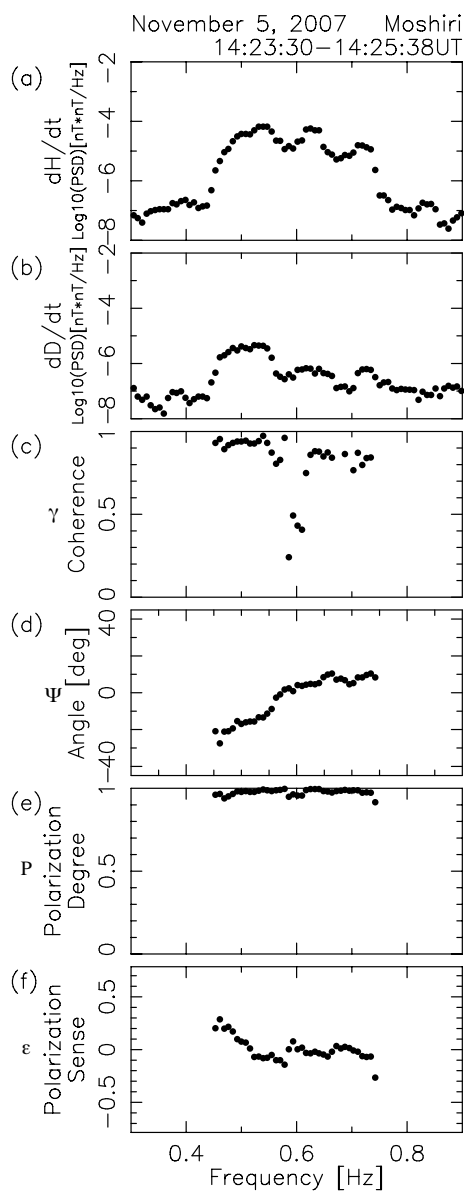
Figure 3.4: The power spectrum density of the (a) H and (b) D components of the magnetic field; (c) coherence, γ, between the H and D components; (d) angle of polarization ellipse orientation Ψ; (e) degree of the polarization P; and (f) polarization sense ε, observed at MSR at 1423:30-1425:38 UT (2323:30-0325:38 LT) on November 5, 2007 for a frequency range of 0.3-0.9 Hz.

varying almost monotonically from -20° to 10° and from 0.3 to -0.1, respectively.

For the low γ at $\sim$0.6 Hz, the PSD of H component is much higher than that of D component. This indicates that a linear 0.6 Hz wave propagated from the magnetic north. This is consistent with results of polarization analysis indicating that Ψ and ε indicate $\sim$0 degree and $\sim$0 for this band (Figures 3.4d and 3.4f), respectively. The angles Ψ show that the waves of higher (lower) frequencies propagated from west (east), with a monotonic variation of Ψ depending on the frequency. Therefore we can see Pc1 waves propagated continuously from east to west including the direction of magnetic north.

Considering the multiple peaks of PSD, several fundamental waves with a bandwidth of $\sim$0.1 Hz may be superimposed in this Pc1 event. Fujita [1988] showed, however, that the attenuation of duct propagation could also make similar multiple peaks in Pc1 bands at low latitudes.

3.2.1.2 Pc1 polarization characteristic and Pc1 pearl structure

Figures 3.5a-3.5f and 3.6a-3.6f show H components of Pc1 pulsations observed simultaneously at PTK, MSR, and STA together with the hodogram and polarization parameters observed at MSR, at 1408-1410 UT and 1422-1424 UT on November 5, 2007. These times are indicated by the vertical arrows in Figures 3.1-3.3. The amplitudes of quasi‑monochromatic pulsations with f $\sim$0.5 Hz vary with a repetition period of $\sim$30 s (Figures 3.5a-3.5c) and $\sim$5 s (Figures 3.6a-3.6c). This feature of amplitude variation has been called the Pc1 pearl structure (e.g., Kangas et al. [1998]). The maximum amplitudes and repetition periods of the pearl structure vary during this event. At STA it is hard to distinguish the pearl structure because of the low intensity of Pc1 pulsations. Figures 3.5d and 3.6d show the hodograms of the Pc1 at MSR calculated for each 4 s segment. These hodograms indicate almost linearly polarized waves, whose polarization ellipse orientation points continuously toward magnetic north with a slight tilt to the west (Figure 3.5d). The hodograms in Figure 3.6d also show almost linearly polarized waves. The orientations were again toward magnetic north with variations from slightly westward to slightly eastward at 1423:30 UT. Figures 3.5d and 3.6d show the hodograms of the Pc1 at MSR calculated for each 4 s segment. These
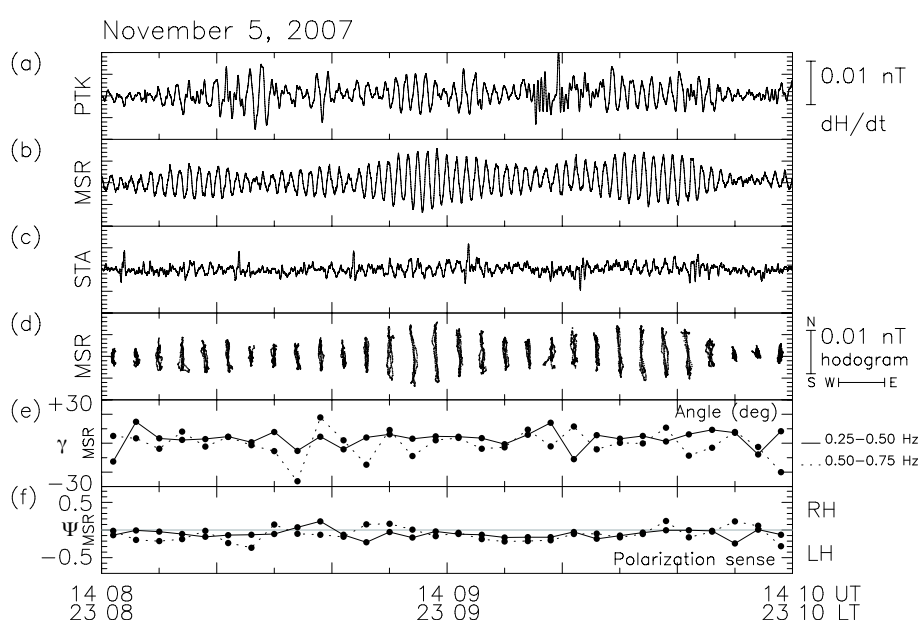
Figure 3.5: H component Pc1 waveform of the magnetic field observed at (a) PTK, (b) MSR, and (c) STA. (d) Pc1 hodogram, (e) angle of polarization ellipse orientation Ψ, and (f) polarization sense ε, at MSR at 1408-1410 UT on November 5, 2007. The polarization parameters are calculated with a time window of 4 s.
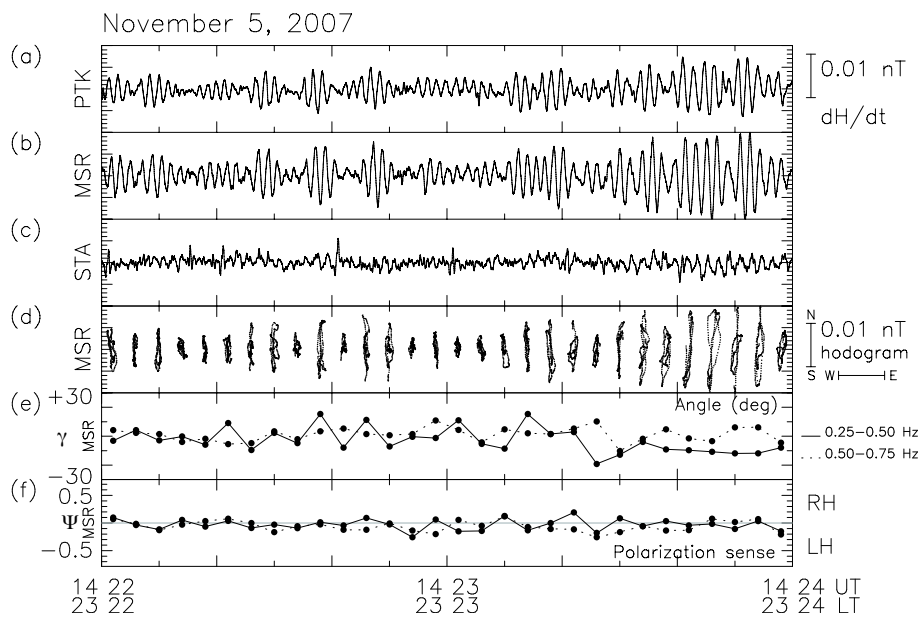
Figure 3.6: H component Pc1 waveform of the magnetic field observed at (a) PTK, (b) MSR, and (c) STA. (d) Pc1 hodogram, (e) angle of polarization ellipse orientation Ψ, and (f) polarization sense ε, at MSR at 1422-1424 UT on November 5, 2007. The polarization parameters are calculated with a time window of 4 s.

hodograms indicate almost linearly polarized waves, whose polarization ellipse orientation points continuously toward magnetic north with a slight tilt to the west (Figure 3.5d). The hodograms in Figure 7d also show almost linearly polarized waves. The orientations were again toward magnetic north with variations from slightly westward to slightly eastward at 1423:30 UT. The repetition period of the Pc1 pearl structure varied from ∼30 to ∼5 s during this Pc1 event observed at MSR, as shown in Figures 3.5a-3.5c and 3.6a-3.6c. Thus, in Figures 3.5e, 3.5f, 3.6e and 3.6f, we selected a time window of 4 s to calculate the angle of polarization ellipse orientation Ψ and polarization sense ε, in order to see the temporal variation associated with Pc1 pearl structures. In Figure 3.5e, the angle Ψ varied ∼50° during the 2 min interval plotted. The beginnings of the Pc1 pearl structure at 1408:30 UT and 1409:20 UT were coincident with the time when Ψ change from negative (positive) to positive (negative). In Figure 3.6e, the angle Ψ varied ∼40° for the 2 min interval plotted. The beginning of the Pc1 pearl structure at 1423:20 UT was coincident with the time when a drastic variation of polarization ellipse orientation from ∼+20° to ∼-20° occurred for the component of 0.25-0.50 Hz. These results suggest that the variation of the angle Ψ is associated with the pearl structure. Figures 3.5f and 3.6f indicate that the polarization sense seems to change similarly to Ψ.

3.2.2   Statistical Analysis

In order to investigate the statistical characteristics of the Pc1 polarization parameters, we examined 93 Pc1 events observed by the induction magnetometer at MSR over 2 year period from July 14, 2007 to July 13, 2009. The total duration of these events is 121.5 h, and the average duration of a single Pc1 event is 1.3 h. We chose three criteria for selecting Pc1 events: (1) The maximum PSD is larger than 10-5.5 nT/Hz; (2) Pc1 events should not be accompanied by a lower - frequency burst, to distinguish them from PiB pulsations associated with substorms; (3) Pc1 events are to be clearly distinguished from multiband structures in the dynamic spectra associated with the Ionospheric Alfvén resonator (IAR).

From the 93 detected events, we selected three types of event based on the characteristics of the angular variation of polarization ellipse orientation: mono-

tonic FDA, patchy FDA, and Monochromatic Angle of polarization ellipse orientation (MA). Monotonic FDA Pc1 events are those for which the angle of polarization ellipse orientation Ψ varies monotonically with Pc1 frequency f (e.g., as shown in Figure 3.2d). Patchy FDA events are those for which Ψ varies with f and time in a complex manner. Finally, MA Pc1 events are those for which Ψ is nearly constant in time and does not depend on f.

Examples of monotonic FDA (August 12, 2008), patchy FDA (November 28, 2007), and MA (April 16, 2008) Pc1 events observed simultaneously at PTK, MSR, and STA are shown in Figures 3.7a-3.7c. These events have been classified according to the $\Psi(f)$ dependence observed at MSR. The polarization sense ε is also shown. The data at STA for August 12, 2008 and November 28, 2007 are not available because of system malfunction.

During the monotonic FDA event, the angle of polarization ellipse orientation at MSR gradually decreases from $\Psi \sim +40°$ to $\Psi \sim 0°$ as the frequency increases from 0.2 to 0.5 Hz (Figure 3.7a). The polarization sense at MSR also varies from $\varepsilon \sim -0.5$ to $\varepsilon \sim 0.5$ at 1030-1200 UT and shows no evident monotonic frequency dependence in contrast to the $\Psi(f)$ behavior. At PTK, $\Psi(f)$ decreases from $\sim +70°$ to $\sim +10°$ with increasing frequency from 0.2 to 0.5 Hz, and the polarization sense is mostly constant: $\varepsilon \sim 0.5$, throughout this event.

For the patchy FDA event, the polarization characteristics at PTK and MSR in the band 0.4-1.2 Hz are shown in Figure 3.7b. The Ψ variations at each station both in frequency and in time are not regular. The variations are not fully random but show patchy structures. The polarization sense also shows patch-like features in frequency and time.

During the MA event (Figure 3.7c), the angle Ψ at MSR has a nearly constant value of $\sim +20°$ for 0.3-0.5 Hz. The polarization at MSR is nearly linear, $\varepsilon \sim 0$, during this event. At STA the angle is mostly $\varepsilon \sim -20°$ and the polarization is also linear, $\varepsilon \sim 0$, as at MSR. The data from PTK are severely contaminated by local noise.

From the 93 selected events, we have found 17 monotonic FDA (18.3%), 51 patchy FDA (54.8%), and 25 MA (26.9%) Pc1 events based on the angle Ψ criterion. Thus, about 70% of Pc1 events observed at MSR demonstrate the frequency dependence of Ψ (monotonic and patchy FDA events).
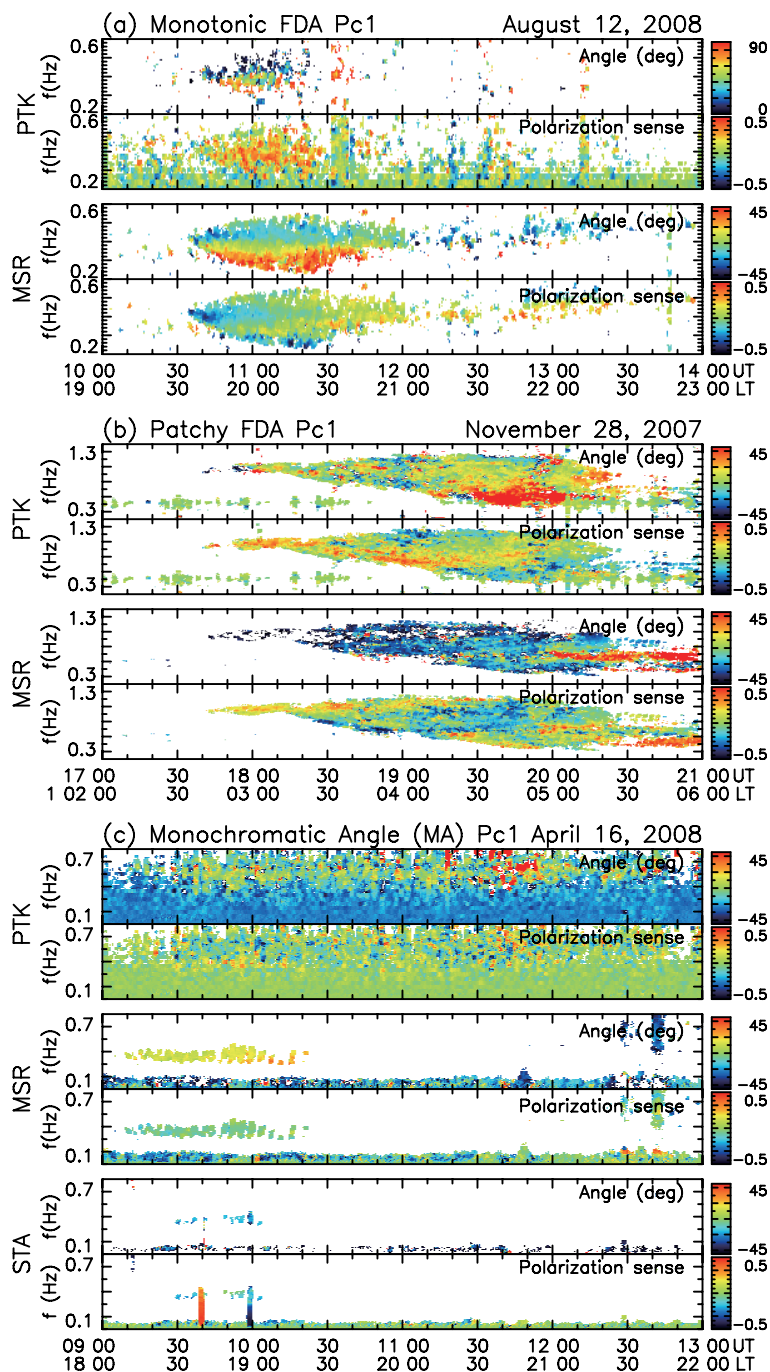
Figure 3.7: Angle of polarization ellipse orientation and polarization sense ε for (a) the monotonic FDA Pc1 at 1035-1210 UT on August 12, 2008 in a frequency range of 0.2-0.5 Hz, (b) the patchy FDA Pc1 at 1700-2100 UT on November 28, 2007 in a frequency range of 0.4-1.2 Hz, and (c) the MA Pc1 at 0910-1020 UT on April 16, 2008 in a frequency range of 0.2-0.3 Hz, observed simultaneously at PTK, MSR, and STA. These events are identified based on the angular variations observed at MSR. The STA data for August 12, 2008 and November 28, 2007 are not available because of system malfunction.

3.2.2.1 Seasonal dependence

The seasonal variation of the Pc1 occurrence rate for the three types of $\Psi(f)$ dependence based on the observations at MSR are shown in Figure 3.8. The
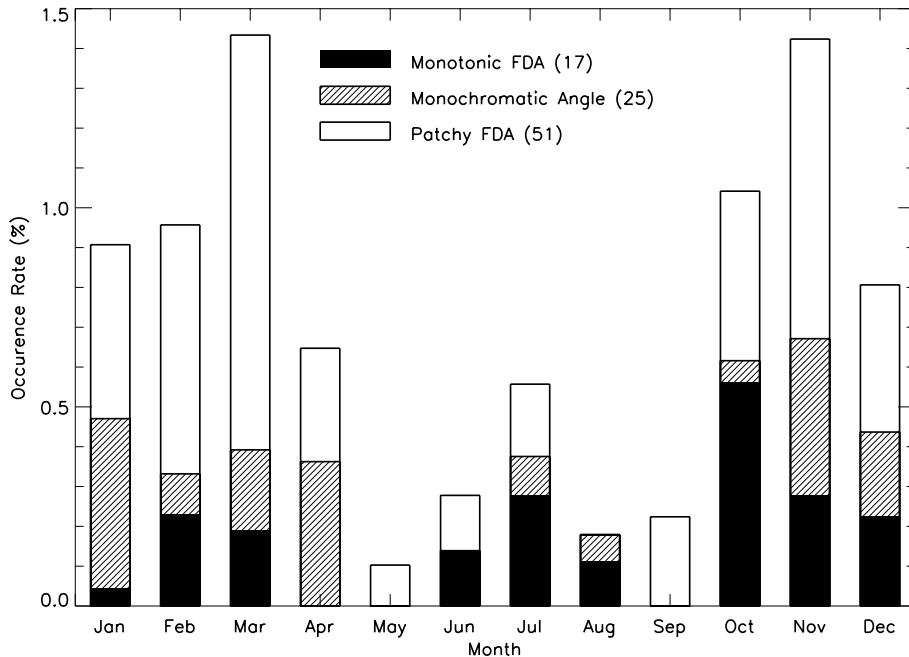
Figure 3.8: Seasonal variation of the Pc1 occurrence rate for three types of angle of polarization ellipse orientation Ψ based on the 93 Pc1 events observed at MSR over 2 years from July 14, 2007 to July 13, 2009. Black, white, and hatched areas indicate occurrence rates for monotonic FDA, patchy FDA, and MA Pc1 events, respectively.

occurrence rate is defined as the duration of time intervals with a specific Pc1 activity divided by the total observation time. In general Pc1 events occur most often in winter (from October to March). Similar seasonal variation of Pc1 occurrence at low latitudes was reported by Kuwashima et al. [1981] and Kawamura et al. [1981]. They explained this variation as being the result of the seasonal variation of the ionospheric density that controls the attenuation of Pc1 waves during their propagation in the ionospheric waveguide. Monotonic FDA and patchy FDA events have seasonal variations that are similar to the general Pc1 activity, that is, more frequent occurrence in winter.

3.2.2.2 Local time dependence

The diurnal dependence of occurrence rate at MSR for each type of Pc1 event is shown in Figure 3.9. General Pc1 activity is low during the daytime, 0600-1700
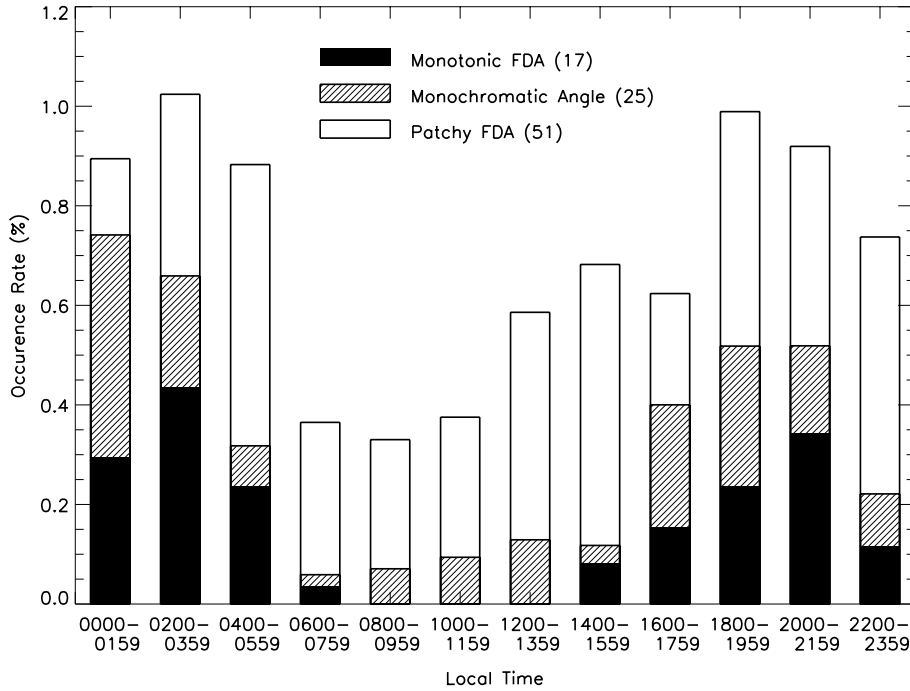
Figure 3.9: Local time dependence of Pc1 occurrence rate for three types of angle of polarization ellipse orientation Ψ based on the 93 Pc1 events observed at MSR over 2 years from July 14, 2007 to July 13, 2009. Black, white, and hatched areas indicate occurrence rates for monotonic FDA, patchy FDA, and MA Pc1 events, respectively.

LT. This dependence can be also explained by ionospheric density variation. The proportion of monotonic FDA events to total Pc1 events is larger during 1600-0500 LT. The characteristics of patchy FDA and MA events are less clear than those of monotonic FDA events.

3.3 Discussion

Using a dynamic polarization analysis, we found that Pc1 polarization character-
istics within a wave packet are not studies of 93 Pc1 events at MSR, we found
that for about 70% of Pc1 events the angle Ψ depended on frequency. The Pc1
occurrence rates of these events were highest in winter and during nighttime.
Here, we discuss the implications of these observed features.

3.3.1 Polarization ellipse orientation

Often the angles of polarization ellipse orientation Ψ exhibit different values de-
pending on frequency. For example, during the monotonic FDA event of Novem-
ber 5, 2007 (Figures 3.1-3.3) the angles Ψ at PTK and MSR vary gradually
from eastward ($\sim$-20°) to westward ($\sim$+20°) with increasing frequency. In other
monotonic FDA events, $\Psi(f)$ varied in a different manner, from the NW quadrant
(positive) to the NE quadrant (negative). During patchy FDA events, Ψ shows
a complex structure for both frequency and time.

If one suggests that the polarization ellipse orientation is closely related to
the wave propagation direction along the ionosphere, the monotonic FDA event
of November 5, 2007 may indicate that the lower-frequency waves propagate
from the east and higher-frequency waves propagate from the west. Galejs [1973]
showed by a model calculation of Pc1 duct propagation that Pc1 waves can prop-
agate not only along the meridian but also eastward and westward directions.
The off-meridian propagation of Pc1 waves was observed at the high-latitude
cusp region (Neudegg et al. [1995]). When we trace the direction of polarization
angles shown in Figure 3.2d at higher- (-20°) and lower- (+20°) frequency com-
ponents, the longitudinal difference between these two paths extends $\sim$800 km
at subauroral latitudes where the observed frequency matches with the modeled
ion cyclotron frequency at the magnetospheric equatorial plane. In this latitude,
Sakaguchi et al. [2008] observed isolated proton auroras which are caused by pre-
cipitation of magnetospheric ions scattered by EMIC waves and can be used as a
proxy of Pc1 ionospheric source since they show one-to-one correspondence with
the Pc1 waves. They found that these proton auroras had longitudinal widths
of 250-800 km, which is comparable to the present value of $\sim$800 km. Thus, it

is possible that a Pc1 source is not a localized point, but a longitudinally extended region. The wave frequencies differ at the western and eastern edges of this region.

This spatial-temporal structure may be formed by a prolonged injection and subsequent drift of energetic protons in the magnetosphere. During this drift, caused by a large-scale electric field, protons penetrate deeper into the inner magnetosphere. As a result, the frequency of waves emitted from regions with a larger B is higher, since the EMIC wave frequency can be estimated as $f \simeq \Omega(V_A/U_i)$, where Ω, V_A, and U_i are the ion cyclotron frequency, the Alfvén velocity and the thermal velocity of hot protons, respectively. Indeed, using the Viking satellite data, Mursula et al. [1997] observed a decrease of Pc1 frequency with increasing magnetic latitude. Erlandson et al. [1990] used the Viking data to show that the polarization parameters of some Pc1 events vary as a function of frequency. They claimed that the variation of polarization parameters is consistent with the spatial structure of the parameters in the model of Fujita and Tamao [1988].

There is a possibility that the Pc1 polarization can be significantly distorted owing to steep lateral gradients of the ionospheric density. Indeed, Fraser [1976] showed from multipoint ground observations of Pc1 waves at low latitudes that the polarization ellipse orientations depend on frequency in the predawn sector when the ionospheric plasma density changes drastically during sunrise. However, our polarization analysis indicates that parameters can vary depending on frequency continuously throughout the event for several hours around midnight when drastic changes of the plasma density are not expected. Therefore, the frequency dependence of polarization parameters should be caused by other factors. Taking into consideration the satellite data discussed above, we suggest the possibility that spatially distributed Pc1 waves at high latitudes with frequencies depending on longitude or latitude propagate in the ionospheric duct to cause the frequency dependence of polarization ellipse orientation at low latitudes. Figure 3.10 shows schematic pictures of the possible Pc1 ionospheric sources and propagation paths to lower latitudes, for monotonic FDA (Figure 3.10a), patchy FDA (Figure 3.10b), and MA Pc1 events (Figure 3.10c). We think that the Pc1 frequency increases with decreasing magnetic latitudes where EMIC waves precipitate to the ionosphere, since the frequency of EMIC waves depends on the

(a) Monotonic FDA event

Pc1 ionospheric source

Lower frequencies

Higher frequencies

Magnetic Latitude

Propagation Path

Low-latitude station

Magnetic Longitude

(b) Patchy FDA event

Magnetic Latitude

Magnetic Longitude

(c) Monochromatic Angle event

Magnetic Latitude

Magnetic Longitude
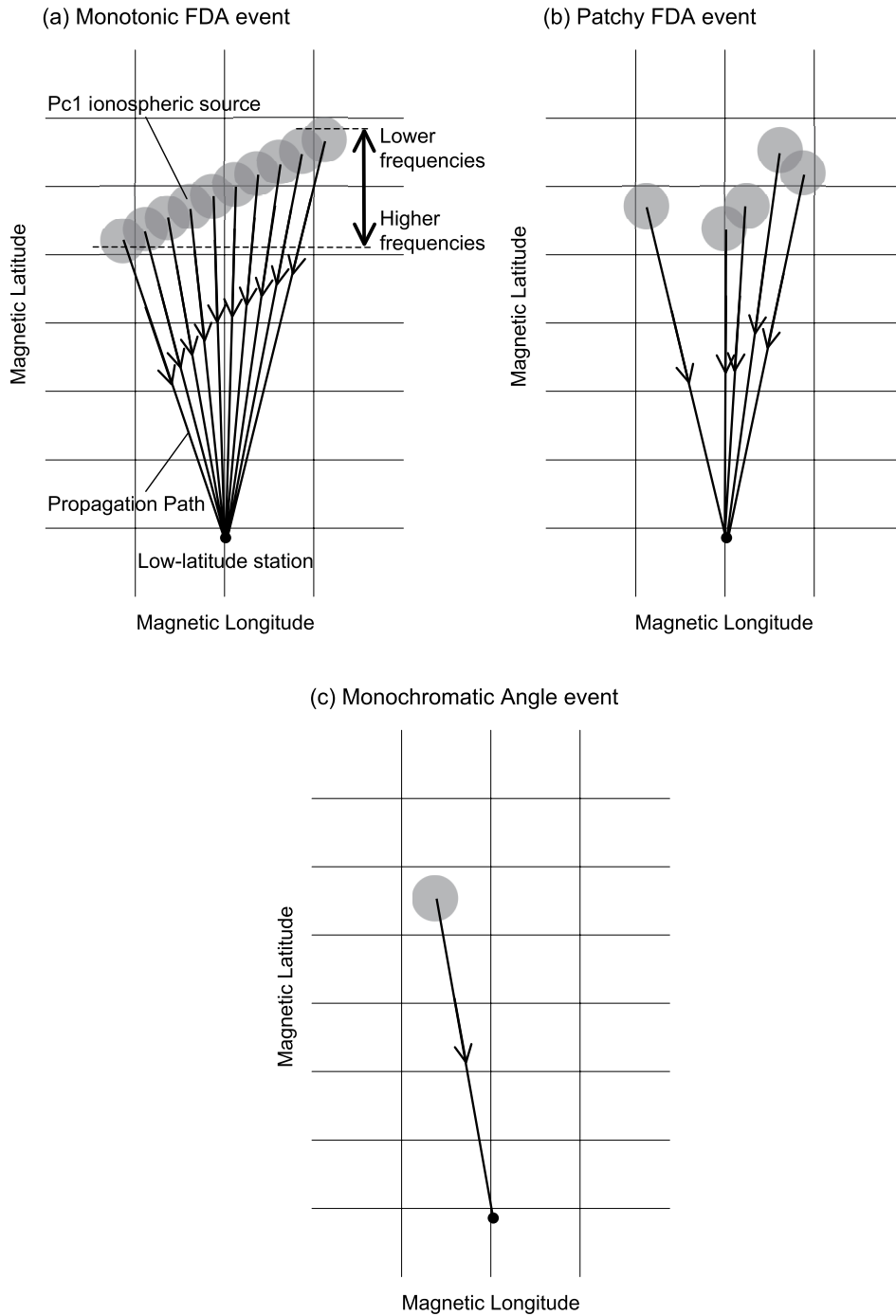
Figure 3.10: Schematic pictures of the possible Pc1 ionospheric sources at high latitudes and propagation paths to lower latitudes for (a) monotonic FDA, (b) patchy FDA, and (c) MA Pc1 events. The gray circles and the solid lines with arrows indicate Pc1 ionospheric sources and propagation paths, respectively.

magnetic field intensity at the magnetospheric equatorial region where the waves are excited. Thus the difference of frequency means the difference in magnetic latitude of the Pc1 source. For monotonic FDA events, we consider a region of Pc1 source expanding continuously both in longitudes (polarization angle) and latitudes (frequency) as shown in Figure 3.10a, because polarization angles vary monotonically depending on frequency. On the other hand, for Patchy FDA events, we consider spatially separated several Pc1 ionospheric sources shown in Figure 3.10b, because polarization angle does not vary monotonically. For MA events, Pc1 ionospheric source would be a localized region as shown in Figure 3.10c.

Any ionospheric disturbances or the gradient of the ionospheric plasma density could modify the Pc1 propagation path (e.g., Summers and Fraser [1972]; Summers [1974]). The amplitude and velocity of Pc1 wave vary during duct propagation (Greifinger and Greifinger [1968] and Greifinger and Greifinger [1973]). However in these previous models, we could not find any mechanism that makes the observed frequency dependence of major axis directions. In the data set used in the present paper, we cannot investigate the relations between the frequency dependence of polarization parameters and Pc1 ionospheric sources to understand how Pc1 waves propagates from source regions to lower latitudes, because we have no information about the Pc1 source. This topic will be investigated in future.

3.3.2 Polarization sense

The dynamic polarization analysis has shown that Pc1 waves can have different polarizations, even within the same wave packet. For example, during the event of November 5, 2007 at MSR (Figure 3.2) Pc1 waves are LH for higher frequencies and RH for lower frequencies, with a reversal at ∼0.5 Hz. Although the theoretical models of Greifinger [1972] predicted that LH waves will be converted into RH and linear waves during ionospheric duct propagation from high to low latitudes, most Pc1 events at MSR showed the coexistence of RH and LH waves. This result may indicate that mode conversion during duct propagation also depends on the wave frequency. Probably, a more advanced theory should consider the transmission and ionospheric waveguide excitation of both RH and LH modes in

a more realistic inhomogeneous ionospheric model.

In particular, during fast mode propagation along the ionospheric waveguide, part of its energy may be converted into higher harmonics of IAR. The Alfvén component of the ionospheric wavefield may result in the occurrence of LH polarization on the ground. The possibility of IAR and waveguide coupling was briefly mentioned by Fujita and Tamao [1988] and needs further examination.

Finally, there is an experimental finding that is not entirely appreciated by the modern theory of EMIC waves and the ICI of the magnetospheric plasma. A long - lasting Pc1 emission observed on the ground is produced not by the continuous generation of EMIC waves in a certain magnetospheric flux tube, but by a sequence of short - lived (<5 min) wave bursts (Engebretson et al. [2002], Engebretson et al. [2008]). These bursts are probably rather chaotically distributed in a certain magnetospheric domain.

3.3.3 Pearl structure

Recently, researchers have begun to reconsider the mechanism behind Pc1 pearl structures, because recent observations provide evidence against the previous interpretation based on the bouncing wave packet (BWP) model. It was thought that the pearl structure is formed by the wave bouncing between hemispheres along the geomagnetic field line. However, new precise observations by satellites indicate that the repetition periods of pearl events are shorter than those expected from the BWP model (e.g., Mursula et al. [1997]; Usanova et al. [2008]), and that only 10%-20% of the incident wave energy is reflected from the ionosphere (Erlandson et al. [1992]). Plyasova-Bakounina et al. [1996] and Mursula [2007] attempted to explain the pearl structures as a modulation of EMIC waves by coexisting Pc4-5 waves. For the event of November 5, 2007, pearl structures with repetition periods of ∼5-30 s were seen at MSR, as shown in Figures 3.5 and 3.6. The repetition period of ∼5 s for the pearl structure of November 5, 2007 is much shorter than the period of Pc5.

The polarization parameters seem to vary in association with the Pc1 pearl structure, especially at the beat minimum points for some times, as discussed in section 2.1. Indeed, Althouse and Davis [1978] also frequently observed that the

polarization sense changes repeatedly during a 10 min period. Pope [1964] showed by model calculations that the superposition of a number of waves with different frequencies should result in periodic variations of not only amplitude but also polarization parameters, and that significant effects occur near the beat minimum points. Thus, pearl structures shown in Figures 3.5 and 3.6 could be the beating. We suggest that this Pc1 event is the superposition of several waves which has slightly different polarization parameters depending on frequency, considering the polarization characteristics of this event (Figures 3.2d and 3.2e).

In our statistical analysis, we found that almost all the Pc1 events observed at low latitudes have the frequency dependence of polarization parameters. This observational fact and the fact that the polarization parameters vary associated with the pearl structure, lead us to the idea that the pearl structure observed at low latitudes may be a beat generated by the superposition of waves with slightly different frequencies.

3.4   Conclusions

In this chapter, we investigated the polarization parameters (angle of polarization ellipse orientation Ψ and polarization sense ε) of Pc1 geomagnetic pulsations observed by induction magnetometers at three low‑latitude stations (PTK, MSR, and STA). We also investigated the seasonal and local time characteristics of the angle of polarization ellipse orientation Ψ for 93 Pc1 events observed at MSR for 2 years. The results can be summarized as follows.

- Pc1 pulsations at our low-latitude stations are most frequently observed in winter and during the nighttime, in accordance with previous results. This indicates that the attenuation of Pc1 waves upon propagation via the ionospheric waveguide is weaker for lower F layer density.

- For $\sim$70% of Pc1 events, the ellipse orientation angle Ψ depends on frequency.

- There is a class of Pc1 events for which the angle Ψ increases or decreases monotonically with increasing frequency. For example, during the November 5, 2007 event, Ψ increases from $\sim$-20° (0.4 Hz) to $\sim$+20° (0.8 Hz).

- The polarization sense ε depends on frequency and time in a complex manner for these Pc1 events.

- For the Pc1 event of November 5, 2007, pearl structures with a repetition period of $\sim$5-30 s were observed at PTK and MSR. Variations of polarization parameters show correspondence with the pearl structures.

From these observations, we suggest that spatially distributed Pc1 waves at high latitudes with frequencies depending on longitude or latitude propagate in the ionospheric duct to cause the frequency dependence of polarization parameters at low latitudes. We also suggest that the Pc1 pearl structures with a repetition period of $\sim$5-30 s observed at low latitudes are produced as a beat of these waves with slightly different frequencies. Existing theoretical models cannot reliably interpret the observed features of the Pc1 polarization structure at low latitudes, which hampers the application of polarization analysis to the remote location of Pc1 sources.

Chapter 4

Pc1 geomagnetic pulsations at subauroral latitudes

4.1 Introduction

None of previous studies have compared the locations of Pc1 ionospheric sources estimated from ground-based Pc1 observations with the actual source locations. In this chapter we investigate for the first time whether Pc1 waves in the ionosphere propagate as a compressional wave at subauroral latitudes, that is, whether the major axis of the Pc1 polarization ellipse points toward the Pc1 ionospheric source, by using proton aurora images and induction magnetometer data obtained on the ground. We determined r, r_0, and the major axis of the Pc1 polarization ellipse observationally and compared the results with the model calculation of Fujita and Tamao [1988].

4.2 Observation

We used an all-sky camera and an induction magnetometer at Athabasca, Canada (ATH, 54.7°N, 246.7°E, magnetic latitude (mlat): 61.7°N). These were deployed by the Solar-terrestrial Environment Laboratory, Nagoya University. The highly sensitive all-sky camera is one of the Optical Mesosphere Thermosphere Imagers (OMTIs) (Shiokawa et al. [1999]; Shiokawa et al. [2009]). In this study, we identify

the region of the isolated proton aurora using images at a wavelength of 557.7 nm, since the intensity of 557.7 nm due to proton precipitation is much brighter than that of 486.1 nm. Sakaguchi et al. [2007] and Sakaguchi et al. [2008] showed that the isolated proton aurora in the 557.7 nm image obtained at ATH appeared at the same position as that in the 486.1 nm images when Pc1 waves were simultaneously observed.

4.2.1   Event Analysis

4.2.1.1   Event 1: April 18, 2006

We observed an isolated proton aurora and associated Pc1 geomagnetic pulsation on April 18, 2006, at ATH. Figures 4.1a and 4.1b show the 486.1 nm and 557.7 nm auroral intensity in a magnetic north-south meridian obtained from the all-sky images with a time resolution of 2 min.

The maximum counts for 236.7°-256.7°E at each magnetic latitude are shown. An isolated aurora appeared to the south of ATH at ∼58°-60° mlat at 0812-0840UT (0012-0040LT). There is no camera data after 0840UT. This luminous region had no large temporal movement in magnetic latitudes. Simultaneously, we observed a Pc1 pulsation at 0.5-1.2 Hz at 0803-0910UT, as shown in Figures 4.1c and 4.1d. These figures show the power spectral density for H- and D-components (PSD_h and PSD_d, respectively) of the magnetic field calculated every 30 s with a time window of 128 s and a frequency resolution of 0.0078 Hz. In the spectra, complicated fine structures with bandwidths of ∼0.1 Hz are continuously emerging.

In Figures 4.1e and 4.1f, we calculated the angle of the polarization ellipse orientation Φ and the polarization sense, based on the method of Fowler et al. [1967] with the same time and frequency resolution as those used in Figures 4.1c and 4.1d. Φ is defined as the angle of the major axis of the Pc1 polarization ellipse from magnetic north. Positive and negative angles indicate westward and eastward orientations, respectively. Right-handed (RH) and left-handed (LH) polarization senses are indicated as positive and negative values, respectively. A zero in polarization sense indicates linear polarization. These parameters are plotted only when $PSD_h \times PSD_d > 10^{-12.5}$ $(nT^2/Hz)^2$. In Figures 4.1e and 4.1f, both Φ
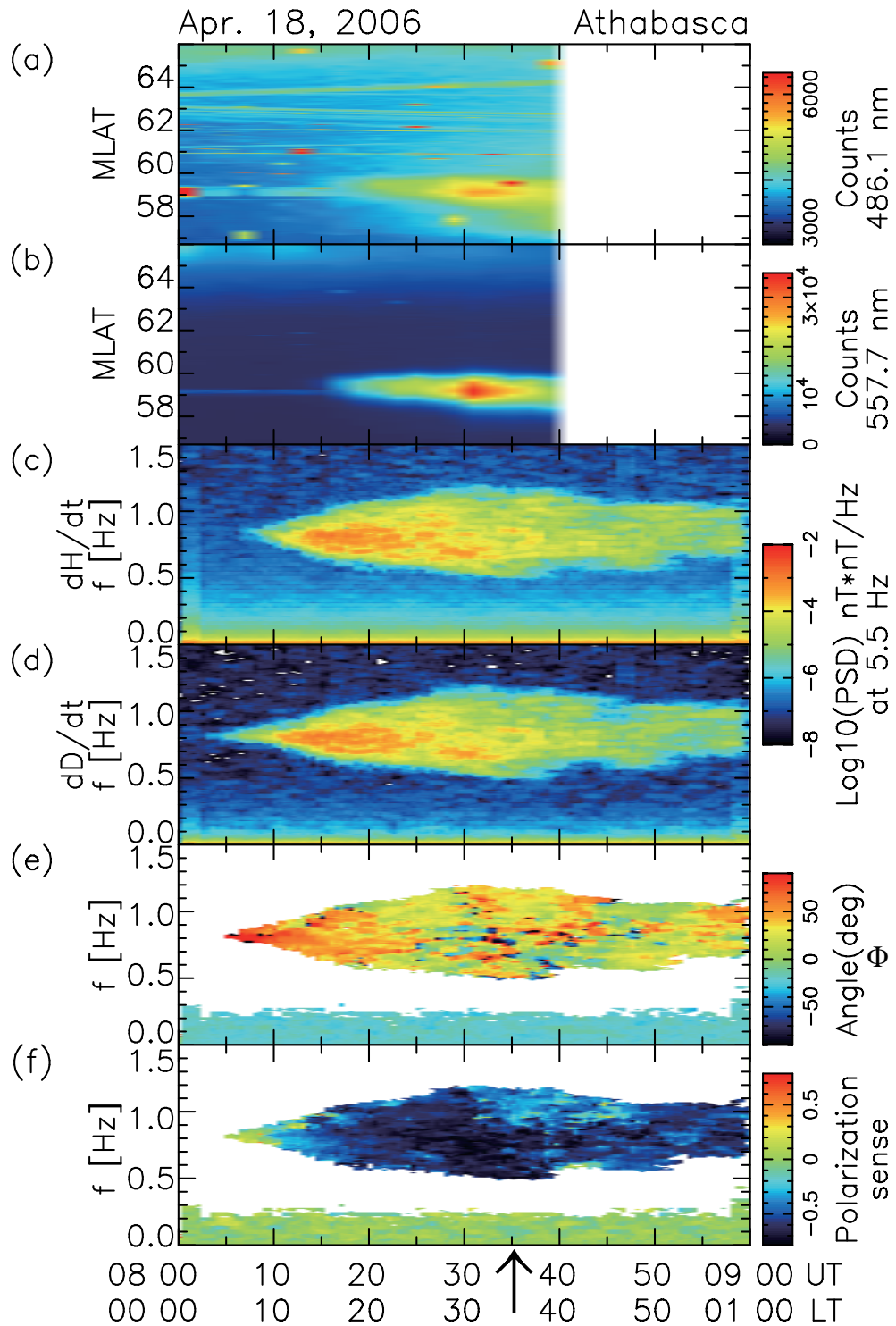
Figure 4.1: The maximum counts in a magnetic north-south meridian at wavelengths of (a) 486.1 nm and (b) 557.7 nm, the power spectral density (PSD) of the (c) H- and (d) D-components of the magnetic field, (e) angle of polarization ellipse orientation Φ, and (f) polarization sense, observed at ATH at 0800-0900UT (0000-0100LT) on April 18, 2006, for a frequency range of 0.0-1.5Hz. These parameters are plotted only when $\mathrm{PSD}_h \times \mathrm{PSD}_d > 10^{-12.5}$. The vertical arrow indicates times 0835:00-0835:30UT for which PSD and polarization parameters are shown in Figure 4.2.

and the polarization sense have complicated frequency and temporal dependences associated with the spectral fine structures shown in Figures 4.1c and 4.1d. Nomura et al. [2011a] have shown similar patchy frequency and temporal dependence of Pc1 polarization parameters at low latitudes using ground induction magnetometers. Kim et al. [2011] also showed complicated polarization characteristics of the Pc1 waves observed at high latitudes. The polarization sense changed from linear to LH mode at 0810UT.

In order to see the details of these fine structures in the Pc1 pulsations, we investigated the frequency dependence of PSD and polarization parameters (Figure 3). We found multiple peaks of PSD and corresponding variations of polarization parameters. Figure 4.2a shows the H and D components of PSD with a frequency resolution of 0.0072 Hz at 0835:00-0835:30UT. These two PSDs are very similar. Three clear peaks are seen at 0.59, 0.71, and 0.86 Hz as indicated by black arrows in Figure 4.2a, corresponding to the fine structures in the dynamic spectra in Figure 4.1. Figures 4.2b and 4.2c show the complicated frequency dependence of Φ and polarization sense. At the frequencies of the multiple peaks in PSD, Φ takes different values, 13.2°, 53.8°, and 39.2°, respectively (Figure 4.2b). The polarization sense is LH for all frequencies in Figure 4.2c. The number of peaks in PSD, the peak frequencies, and the corresponding values of polarization parameters vary significantly with time.

We should note here that in previous studies (e.g., Fraser and Summers [1972]; Althouse and Davis [1978], a fixed narrow-band filter was used to determine the propagation direction in the ionospheric duct using the major axis of Pc1 polarization ellipse. If each fine structure in Figure 4.1 is a minimum unit of Pc1 wave packets, the propagation direction may contain several Pc1 wave packets when we use a fixed-band filter, because fine structures change their frequencies in time during this event and their life time is shorter than that of the whole Pc1 event. Therefore, in order to investigate the relation between the position of the Pc1 ionospheric source and the propagation direction determined by the Pc1 polarization at ATH, we compared the brightest position of the proton aurora and the major axis direction of the Pc1 frequency component at the maximum PSD, since it is reasonable to consider that Pc1 waves with maximum amplitudes are related to the brightest point of the proton aurora. The red arrows in Figures
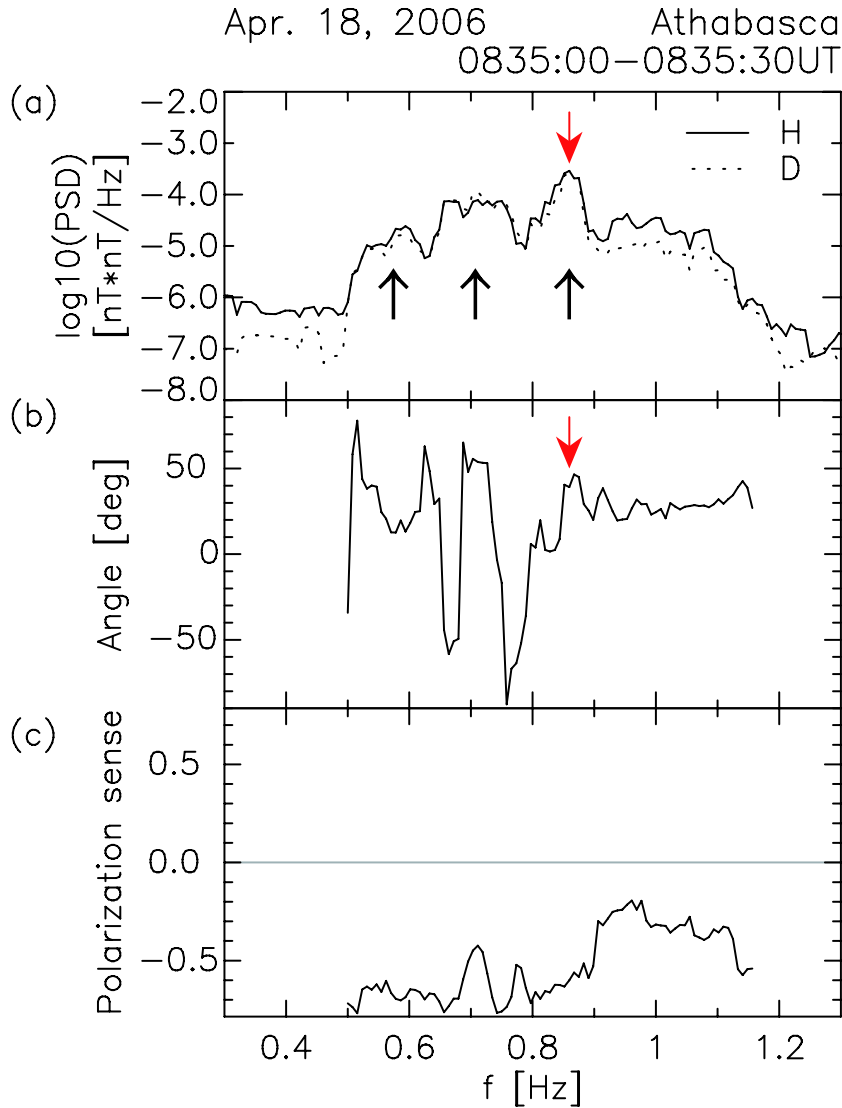
Figure 4.2: (a) The power spectral density of H- (solid line) and D- (dashed line) components of the magnetic field, (b) angle of polarization ellipse orientation Φ, and (c) polarization sense, observed at ATH at 0835:00-0835:30UT (0035:00-0035:30LT) on April 18, 2006, for a frequency range of 0.3-1.3Hz. The black and red arrows in Figures 4.2a and 4.2b indicate PSD peaks and the frequency with maximum $PSD_h \times PSD_d$, respectively.

4.2a and 4.2b indicate the frequency at which $\text{PSD}_h \times \text{PSD}_d$ is a maximum.

4.2.1.2 Analysis method

Figure 4 shows the definition of the parameters for the isolated proton aurora and Pc1 polarization that are used in our analysis. The gray filled area indicates proton aurora. We identify the region of the isolated proton aurora, which we consider to be the Pc1 ionospheric source region, as the auroral region where the count is higher than 120-130% of the background count. If necessary, visual inspection was also used to distinguish the region of isolated proton aurora from the bright auroral oval which is usually seen in the northern part of the images. The area size of the proton aurora S can be calculated using these definitions. Then in order to define the scale size of the Pc1 ionospheric source which was used as r_0 in the model by Fujita and Tamao [1988], we defined three parameters r_s, r', and r_{max} as shown in Figure 4.3. The r_s is defined as $r_s = \sqrt{S/\pi}$. The r' is defined as the distance between the brightest point and the edge of the proton aurora along the line between the brightest point and the observation site on the ground. The r_{max} is defined as $r_{max} = \sqrt{g_{w1}^2 + g_{w2}^2}$, where g_{w1} and g_{w2} are the proton aurora width in the geographic latitude and longitude, respectively. We selected the highest/lowest latitudes and longitudes of the edge positions. The differences between the highest and lowest values give the width g_{w1} and g_{w2} in the geographical latitude and longitude, respectively. The cross shows the brightest position in the proton aurora, which we use as the position of the proton aurora. The r is the distance from the ATH station to the position of the proton aurora at an altitude of 300 km where Pc1 waves propagate in the ionospheric duct. The angle θ_2 is defined as the angle between the magnetic north and the proton aurora from the ATH station.

We calculate the major axis direction of the Pc1 polarization ellipse using induction magnetometer data with a time window of 128 s, a frequency resolution of 0.0072 Hz, and a time resolution of 120 s which is the same time resolution as that of the all-sky camera data. The angle θ_1 is defined as the angle from the magnetic north to the major axis of the Pc1 polarization ellipse at the frequency corresponding to the maximum PSD. The angle θ is defined as $\theta = \theta_1 - \theta_2$. In
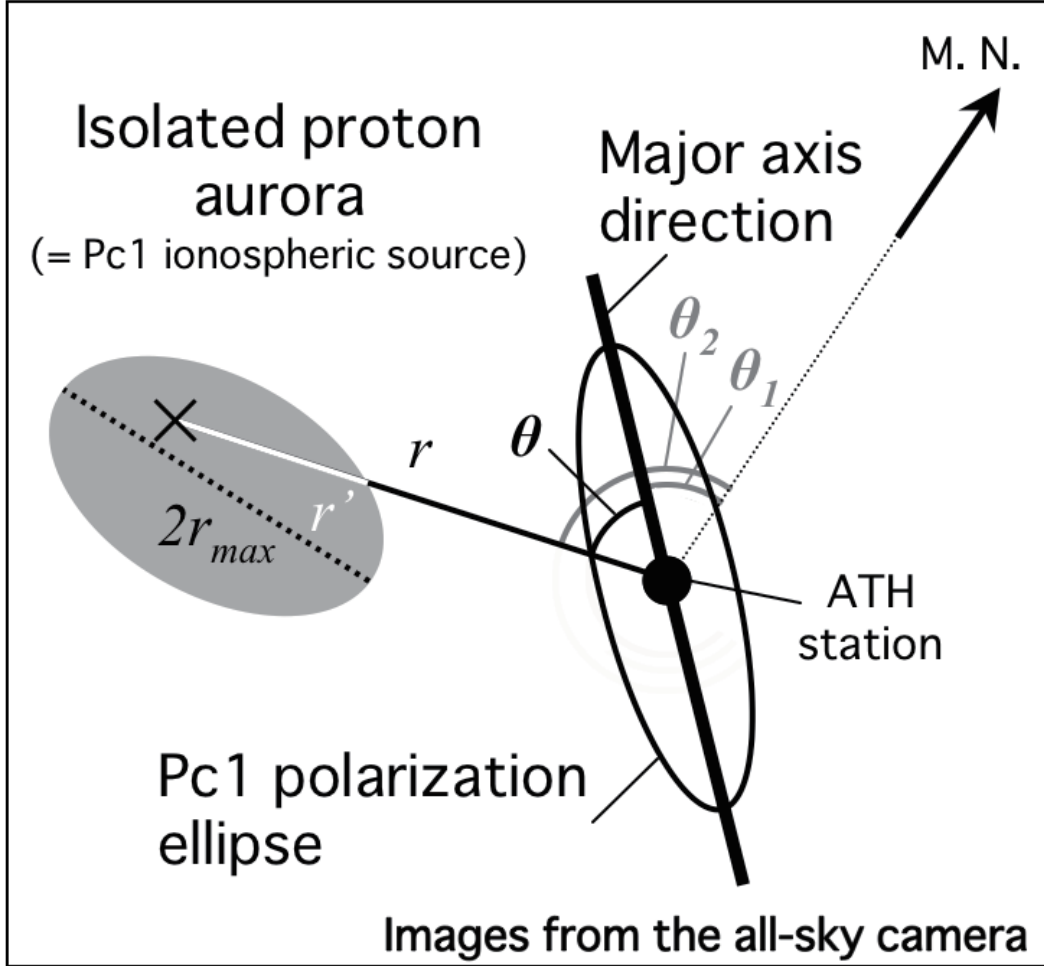
Figure 4.3: Schematic picture of our analysis method using images of isolated proton aurora observed by an all-sky camera and the major axis of the Pc1 polarization wave measured by an induction magnetometer, both at ATH. The gray area is the proton aurora as a Pc1 ionospheric source, θ_1 is the angle of the Pc1 major axis from magnetic north, θ_2 is the angle between the proton aurora and the magnetic north at the ATH station. We also define the angle $\theta = \theta_1 - \theta_2$. The proton aurora size is defined by r_s, r', and r_{max}, where $r_s = \sqrt{S/\pi}$ and S is the area of the proton aurora. The r' is the distance between the brightest point and the edge of the proton aurora along the line between the brightest point and the observation site on the ground. The $r_{max} = \sqrt{g_{w1}^2 + g_{w2}^2}$ where g_{w1} and g_{w2} are the proton aurora width in geographic latitude and longitude. The r is the distance from the ATH station to the proton aurora.

the model calculation of Fujita and Tamao [1988], the major axis points toward the source center ($\theta = 0°$) in regions far from the source center ($r \gg r_0$), because the compressional waves become dominant. On the other hand, the major axis points in the azimuthal direction ($\theta = \pm 90°$) near the source region ($r \le r_0$), because the Alfvén wave is dominant. Using the above method, we investigated how the major axis of the Pc1 polarization ellipse rotates depending on r/r_0 and compared the results with the model calculation by Fujita and Tamao [1988].

4.2.1.3 Relation between the Pc1 polarization and the position and size of the proton aurora

Figure 4.4 shows snapshots of auroral images at a wavelength of 557.7 nm with the major axis direction of Pc1 polarization ellipse at PSD maximum observed at ATH for 0814-0836UT on April 18, 2006. The images are centered on ATH with $10° \times 20°$ widths of geographic latitudes and longitudes. In this series of snapshots, the large bright area in the north is the auroral oval and the bright spot in the southeast is the isolated proton aurora. The red line indicates the major axis direction of the Pc1 polarization ellipse at the frequency of PSD maximum. This line points the position of the proton aurora with some small fluctuations. The two white lines indicate the geomagnetic latitude and longitude of ATH. The black line indicates contours of the boundary count defined as 130% of the background count. We identified these surrounded areas as the isolated proton aurora. The cross shows the position of the maximum count in the isolated proton aurora. This proton aurora is located ~ 400 km southeast from ATH and did not move significantly. The size of the proton aurora increased with time.

In order to compare the position of the proton aurora and the major axis direction of Pc1 polarization ellipse in detail, we calculated the wave and position parameters shown in Figure 4.5. Figure 4.5a shows the temporal variation of f_{Pmax} which is the frequency of the PSD maximum in the observed Pc1 band. The value of f_{Pmax} was not always at the center of the Pc1 band (0.5-1.2 Hz) and varied in the range 0.6-0.9 Hz. Figure 4.5b shows angles θ_1 and θ_2 which are defined in Figure 4.3. The angles are positive (negative) for westward (eastward) and zero for the magnetic north. The θ_1 varied from 10° to 70° while the θ_2 did

Figure 4.4: All-sky images at a wavelength of 557.7 nm every 2 min between 0814 and 0836UT (0014-0036LT) on April 18, 2006. The images are centered on ATH with 10°×20° widths of geographic latitudes and longitudes. The red lines are the major axis direction of the Pc1 polarization ellipse at ATH calculated by polarization analysis, the cross shows the position of the maximum count in the isolated proton aurora, the black lines indicate the positions of the boundary counts (130% of background count), and the white lines are the equivalent geomagnetic latitude and longitude of ATH.

72
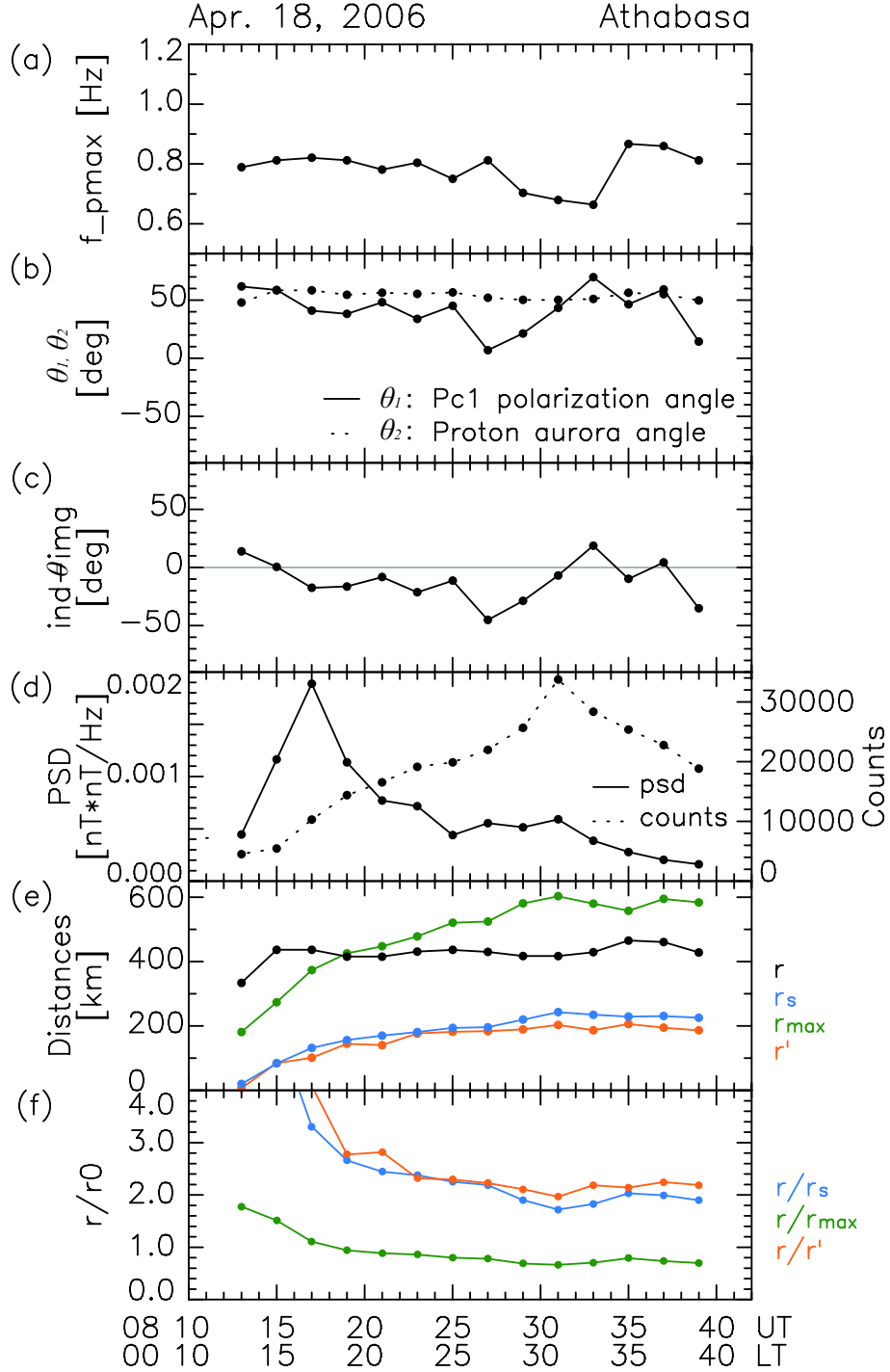
Figure 4.5: (a) The frequency of the power spectral density maximum in the Pc1 band, (b) θ_1 (solid line) and θ_2 (dashed line) as defined in Figure 4.3, (c) $\theta = \theta_1 - \theta_2$, (d) the maximum of the power spectral density in the Pc1 band (solid line) and the count at a wavelength of 557.7nm (dashed line), (e) distance of the proton aurora from ATH r and the scale size of the proton aurora r_s, r', and r_{max} as defined in Figure 4.5, and (f) r/r_s, r/r', and r/r_{max}. The figures cover 0812-0838UT (0012-0038LT) on April 18, 2006. The time resolution is 2 min. The data points are indicated by dots at the center of the 2-min time interval.

not vary significantly. Figure 4.5c shows $\theta(= \theta_1 - \theta_2)$ which indicates the angle between the major axis direction and the direction of the Pc1 ionospheric source. The major axis points to the position of proton aurora when $\theta = 0°$ and to the azimuthal direction when $\theta = \pm 90°$. The θ varies between -50° and 10°, indicating that the Pc1 major axis mostly points toward the proton aurora. The average and the standard deviation of θ are -11.8° and 17.9°, respectively. Figure 4.5d shows the maximum PSD values of the Pc1 waves (solid curve) and the maximum counts of the isolated proton aurora (dashed curve). The significant PSD peak at 0816-0818UT did not correspond to the peak of the proton aurora count. The other small PSD peak at 0830-0832UT did correspond to the count maximum. Figure 4.5e shows r, r_s, r' and r_{max}, where r is the distance from ATH to the proton aurora and r_s, r', and r_{max} denote the scale sizes of the proton aurora. The r_s and r' increased from ~0 km to 200 km. The r_{max} increased from ~200 km to 400 km. The distance r to the proton aurora was ~400 km and did not change significantly. We plot r/r_s, r/r', and r/r_{max} in Figure 4.5f to see the relation to the rotation angle θ shown in Figure 4.5c. The r/r_s and r/r' were mostly higher than 2, while the r/r_{max} was mostly less than 1. Since the Pc1 major axis points toward the proton aurora ($\theta = 0°$), this result is consistent with the model calculation of Fujita and Tamao [1988] in the case of $r \gg r_0$, except for r_{max}.

4.2.1.4   Event 2: October 18, 2006

Here we show another event of simultaneous isolated proton aurora and Pc1 pulsation observed on October 18, 2006 at ATH, as shown in Figure 4.6. The figure format is the same as that of Figure 4.1.

The keograms in Figures 4.6a and 4.6b show an isolated proton aurora observed by the all-sky camera from 0922 to 0950UT (0122-0150LT). There is no camera data after 0950UT. The magnetic latitude of this proton aurora moved from 62.2° to 61.6° and the latitudinal width of the proton aurora widened from ~0.5° to ~1.5° during this event. Figures 4.6c and 4.6d show PSDs of Pc1 pulsations at 0.3-0.9 Hz simultaneously observed from 0835 to 1100UT by the induction magnetometer. Fine structures with bandwidths of ~0.1 Hz, similar

74
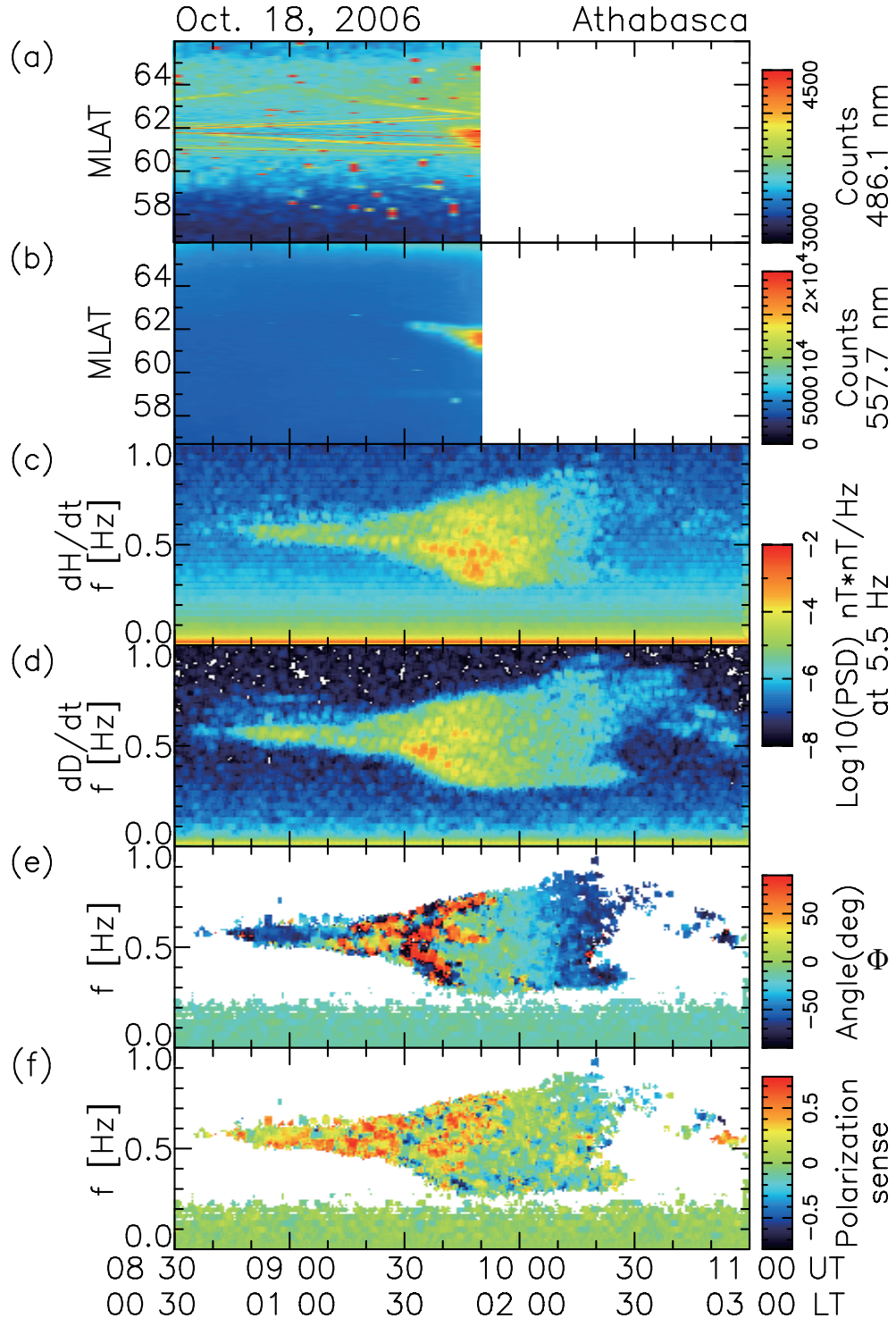
Figure 4.6: The maximum counts in a magnetic north-south meridian at wavelengths of (a) 486.1 nm and (b) 557.7 nm, the power spectral density (PSD) of the (c) H- and (d) D-components of the magnetic field, (e) angle of polarization ellipse orientation Φ, and (f) polarization sense, observed at ATH at 0830-1100UT (0030-0300LT) on October 18, 2006, for a frequency range of 0.0-1.0Hz. These parameters are plotted only when $PSD_h \times PSD_d > 10^{-12.5}$.

75

to those seen in Figures 4.1c and 4.1d, can be seen in the spectra. When the intensity of a fine Pc1 band at ∼0.5 Hz increased sharply at 0930UT, the proton aurora became clearer. Figure 4.6e shows distinct frequency and temporal dependences of polarization angle associated with the spectral fine structures. For example the structure at the PSD maximum in Figure 4.6d at 0930-0940UT at 0.4-0.5 Hz coincides with a patch in Figure 4.6e at 0.4-0.5 Hz with a ±90° polarization angle. Figure 4.6f shows that the polarization sense also depends on time and frequency and changes from RH (∼0.5) to nearly zero at ∼0950UT.

Figure 4.7 shows snapshots of auroral images at a wavelength of 557.7 nm with the major axis of the Pc1 polarization ellipse at the PSD maximum at ATH for 0926-0948UT on October 18, 2006. The figure format is the same as that of Figure 4.4. The boundary count is taken as 120% of the background count. Separated from the auroral oval in the northern part of the images, an isolated proton aurora appeared in the northwest and moved eastward. This proton aurora became larger with time, as in event 1. However the differences from event 1 are as follows. The bright region is much closer to ATH, and is longer in longitude and thinner in latitude. Especially, multiple proton auroras appeared for 0932-0936UT. The position of the maximum count in the proton aurora was nearest to ATH at 0940UT and moved from northwest to east. The major axis did not point stably to the position of the proton aurora. At 0938-0948UT the major axis points in the azimuthal direction of the proton aurora. On the other hand at 0926-0936UT it points toward the proton aurora. However, we should note that it is difficult to identify the azimuthal or the radial direction in this event, because the proton aurora was very close to ATH.

Figure 4.8 shows wave and aurora parameters used to compare the position of proton aurora and the major axis direction of the Pc1 polarization ellipse for the event on October 18, 2006. The figure format is the same as that of Figure 4.5. Figure 4.8a shows that the f_{Pmax} varied from 0.4 to 0.6 Hz. It was not always at the center of the Pc1 band of 0.3-0.9 Hz. Sudden changes of θ_1, θ_2, and θ at 0938UT can be seen in Figures 4.8b and 4.8c. The major axis was parallel to the latitudinal line of ATH before 0936UT as shown in Figure 4.7 (note that $\theta_1 = 90°$ is the same as $\theta_1 = -90°$). After that, the major axis pointed toward magnetic north ($\theta_1 = 0°$). Figure 4.8b shows that θ_2 also changed by ∼$\Delta 150°$
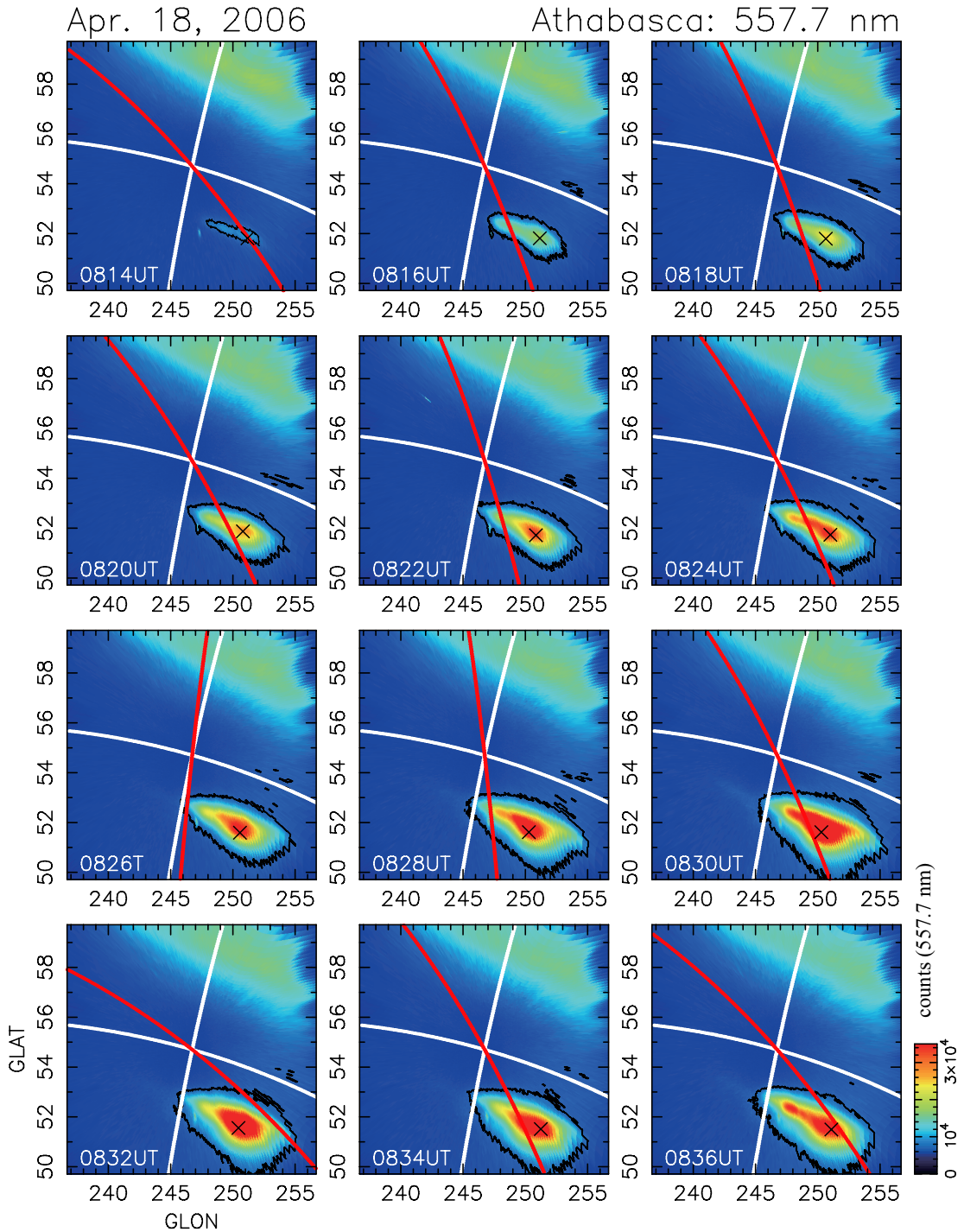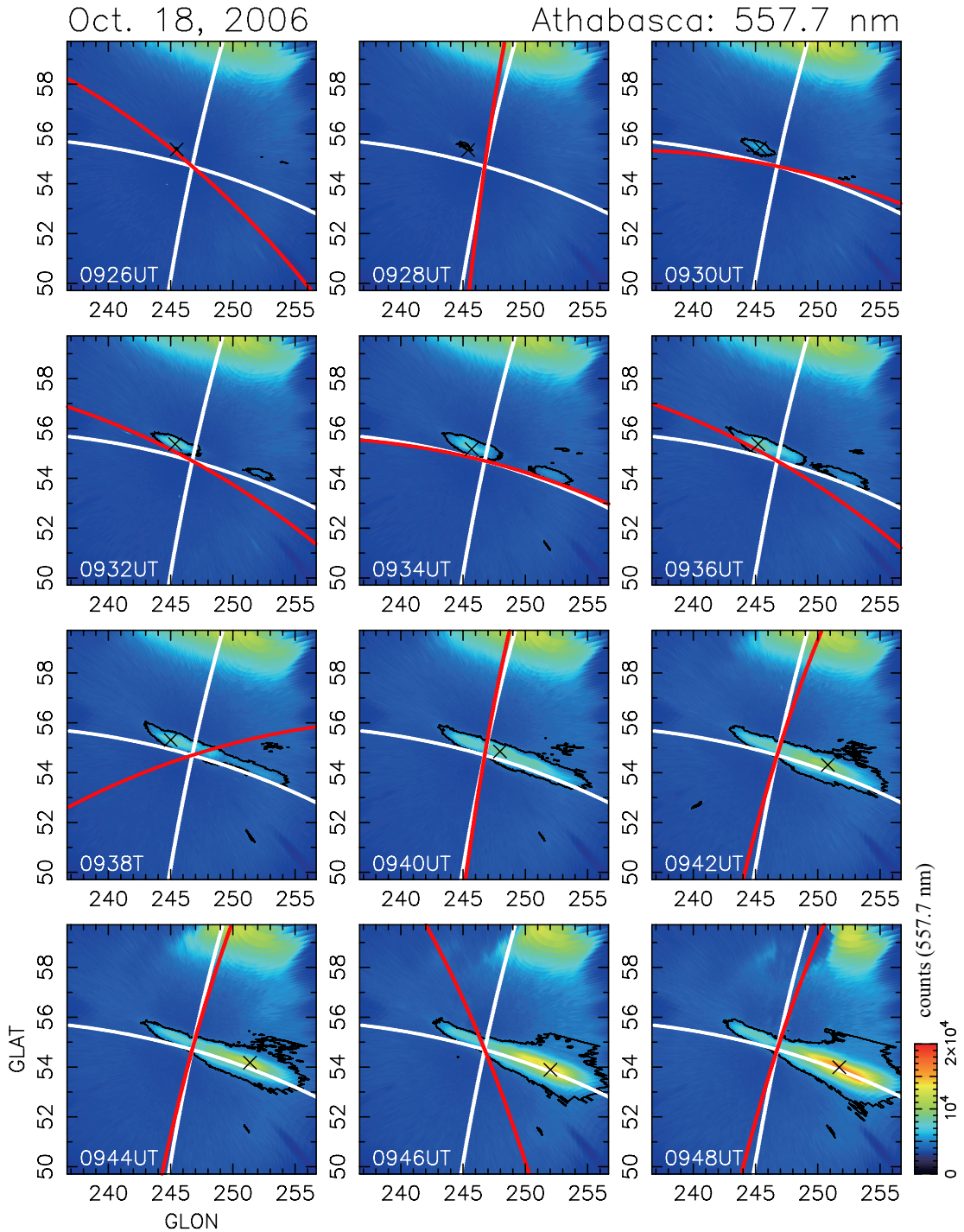
Figure 4.7: All-sky images at a wavelength of 557.7 nm every 2 min between 0926 and 0948UT (0126-0148LT) on October 18, 2006. The images are centered on ATH with 10°×20° widths of geographic latitudes and longitudes. The red lines are the major axis direction of the Pc1 polarization ellipse at ATH calculated by polarization analysis, the cross shows the position of the maximum count in the isolated proton aurora, the black lines indicate the positions of the boundary counts (120% of background count), and the white lines are the equivalent geomagnetic latitude and longitude of ATH.

77
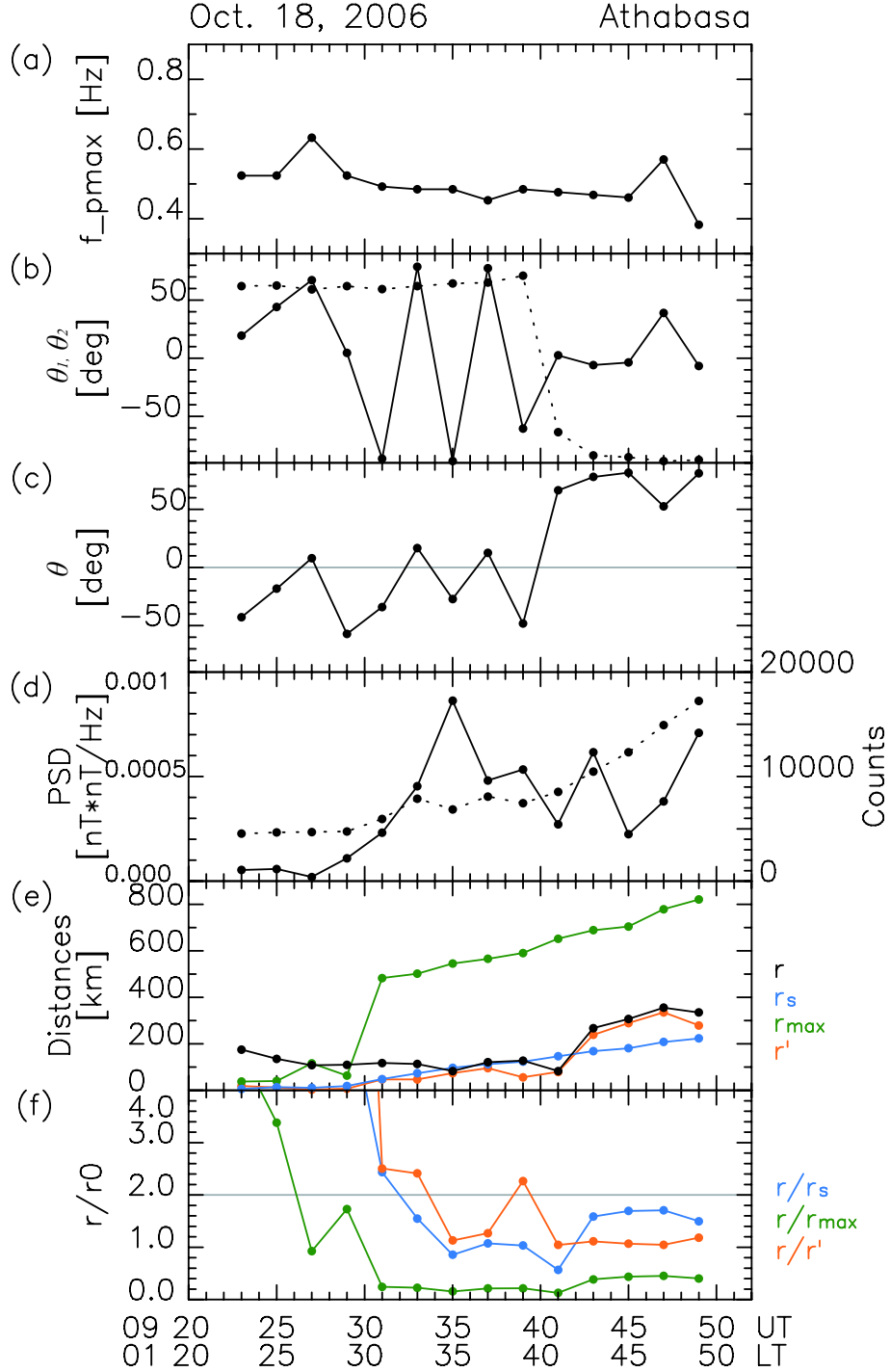
Figure 4.8: (a) The frequency of the power spectral density maximum in the Pc1 band, (b) θ_1 (solid line) and θ_2 (dashed line) as defined in Figure 4.3, (c) $\theta = \theta_1 - \theta_2$, (d) the maximum of the power spectral density in the Pc1 band (solid line) and the count at a wavelength of 557.7nm (dashed line), (e) distance of the proton aurora from ATH r and the scale size of the proton aurora r_s, r', and r_{max} as defined in Figure 4.3, and (f) r/r_s, r/r', and r/r_{max}. The figures cover 0812-0838UT (0012-0038LT) on April 18, 2006. The time resolution is 2 min. The data points are indicated by dots at the center of the 2-min time interval.

at 0938UT from northwest to east. Therefore, before 0938UT the major axis pointed to the proton aurora ($\theta = \sim 0°$) and after 0938UT the major axis pointed perpendicular to the proton aurora ($\theta = \sim 90°$), as shown in Figure 4.8c. We could find no clear correspondences between PSD peaks and the proton aurora intensity (Figure 4.8d). Figure 4.8e shows that r_s increased monotonically to 210 km. On the other hand, r and r' increased suddenly from ~ 100km at 0940UT and became ~ 300 km at 0948UT. The r_{max} increased drastically at 0930UT and became ~ 800 km at 0948UT. These variations are related to the movement and the expansion of the proton aurora. Figure 4.8f shows that r/r_s, r/r', and r/r_{max} are less than 2 after 0940UT. Before $\sim$0930UT r/r_s, r/r', and r/r_{max} could be overestimated because the intensity of the proton aurora was too weak to distinguish it from background counts in the images.

4.2.2 Statistical Analysis

In order to understand observationally the relation between the rotation of the Pc1 polarization ellipse θ, and the scale sizes r_s, r', and r_{max} and horizontal distance r of the Pc1 ionospheric source, we investigated Pc1 pulsations and simultaneous isolated proton auroras observed over 4 years at ATH from September 7, 2005, to September 6, 2009. The events from September 7, 2005, to September 3, 2006, are those studied by Sakaguchi et al. [2008] to show a one-to-one correspondence between isolated proton aurora and Pc1 pulsations. For the events after September 4, 2006, we selected Pc1 geomagnetic pulsation events for 455 days with $\mathrm{PSD}_h > 10^{-6.0}$ nT^2/Hz at ATH. In these 455 days the all-sky camera was operated for 92 nights including 30 nights with clear sky. We found isolated proton auroras with Pc1 pulsations on 27 nights. From these 27 night events and the 9 events selected by Sakaguchi et al. [2008], we finally identified 27 Pc1 events with proton auroras satisfying the criteria that (1) a clear boundary can be defined between the isolated proton aurora and the aurora oval, and (2) no other significant isolated proton auroras are observed at the same geomagnetic latitudes. When the isolated proton aurora appeared twice in one night, we treated them as 2 events. Table 4.1 lists the date, time, and temporal averages and standard deviations of the position and the width of proton auroras in ge-

ographical latitude and longitude for those events. Table 4.2 also lists temporal averages and standard deviations of θ, r, r_s, r' and r_{max} for these events. To distinguish the isolated proton aurora from the background sky emission, we used a boundary count of 120-130% of the background count. This boundary count varies depending on the sky condition.

Figure 4.9 shows typical examples of events. For the events shown in Figure 4.9a-f the major axis of the Pc1 polarization ellipse corresponding to the PSD maximum points toward the isolated proton aurora; for the event shown in Figure 4.9g-l the major axis did not point toward the isolated proton aurora. The figure format is same as that of Figure 4.4. The event of July 23, 2009 (event #27 in Table 4.1) in Figures 4.9f and 4.9l, includes both cas

4.2.2.1 Comparison to the Model calculation

Figure 4.10a shows the results of the model calculation by Fujita and Tamao [1988] (Figure 4.5) showing how the Pc1 polarization ellipse rotates depending both on r/r_0 and r/D from the azimuthal direction. In their model, they define r_0, r, and D as the radius of the Pc1 ionospheric source, which is assumed to be a circle shape, the distance from the source center, and the thickness of the ionospheric duct, respectively. The azimuthal and radial directions are indicated in the vertical axis by $0°$ and $90°$, respectively. When Pc1 waves are observed on the ground (solid line indicated by an arrow in Figure 4.10a), the major axis of the Pc1 polarization ellipse rotates from the azimuthal to the radial direction at $1.0 < r/r_0 < 2.0$. We call this region of r/r_0 the transition region. Figures 4.10b-d show the dependence of r/r_s, r/r', and r/r_{max} on the absolute rotation angle from the azimuthal direction ($90° - |\theta|$) of the major axis of the Pc1 polarization ellipse from our statistical analysis of the observations. The large and small circles indicate the values averaged over each event and all 2-min data, respectively. The error bars are the standard deviation. In Figures 4.10b-d, we can see the tendency that the major axis tends to point toward the radial direction ($90° - |\theta|=90°$) at further distance, particularly for r/r'. The transition of $90° - |\theta|$ from the azimuthal direction ($90° - |\theta|=0°$) to the radial direction ($90° - |\theta|=90°$) occurs at $r/r_s \sim$2.0-4.0, $r/r' \sim$2.0-4.0, and $r/r_{max} \sim$0.5-1.5. The r/r_{max} gives an agreement

Table 4.1: Lists of the Parameters the Analyzed Events

#	day	hour [UT]	averaged value $\pm$ standard deviation			
			glat [deg]	glon [deg]	wglat [deg]	wglon [deg]
1	Oct. 29, 2005	0956-1016	55.8 $\pm$ 0.2	247.4 $\pm$ 0.4	1.19 $\pm$ 0.49	4.03 $\pm$1.86
2	Nov. 2, 2005	0120-0310	56.9 $\pm$ 0.6	242.5 $\pm$ 0.9	3.41 $\pm$ 1.29	5.58 $\pm$ 1.98
3	Nov. 25, 2005	0348-0402	56.7 $\pm$ 0.5	239.5 $\pm$ 1.6	3.08 $\pm$ 1.00	8.05 $\pm$ 0.97
4	Apr. 18, 2006	0510-0620	50.0 $\pm$ 1.7	249.9 $\pm$ 1.6	1.74 $\pm$ 0.15	7.42 $\pm$ 1.87
5		0812-0838	51.7 $\pm$ 0.2	250.7 $\pm$ 0.5	2.96 $\pm$ 0.88	8.14 $\pm$ 2.09
6	Aug. 21, 2006	0632-0658	54.4 $\pm$ 2.4	241.0 $\pm$ 11.2	2.08 $\pm$ 0.44	6.79 $\pm$ 1.59
7		0716-0724	52.5 $\pm$ 0.5	250.0 $\pm$ 2.1	1.39 $\pm$ 1.01	4.82 $\pm$ 3.32
8		0740-0742	52.0 $\pm$ 0.0	252.1 $\pm$ 0.1	1.07 $\pm$ 0.13	1.98 $\pm$ 0.46
9	Sep. 2, 2006	0830-1040	56.5 $\pm$ 0.6	239.6 $\pm$ 1.7	3.18 $\pm$ 0.52	6.86 $\pm$ 1.86
10	Sep. 23, 2006	0956-1004	54.4 $\pm$ 0.7	252.0 $\pm$ 2.1	1.00 $\pm$ 0.13	5.74 $\pm$ 0.36
11		1018-1028	53.6 $\pm$ 0.3	253.9 $\pm$ 0.7	1.42 $\pm$ 0.13	6.47 $\pm$ 0.47
12	Sep. 27, 2006	0638-0700	54.2 $\pm$ 0.5	250.7 $\pm$ 1.1	0.87 $\pm$ 0.39	3.77 $\pm$ 1.23
13		0724-0730	54.2 $\pm$ 0.5	250.1 $\pm$ 1.6	0.47 $\pm$ 0.27	2.56 $\pm$ 1.63
14		0940-0954	53.7 $\pm$ 0.1	251.6 $\pm$ 0.9	0.60$\pm$ 0.18	1.72 $\pm$ 0.64
15	Oct. 18, 2006	0922-0948	55.0 $\pm$ 0.6	247.2 $\pm$ 2.8	2.02 $\pm$ 1.19	8.24 $\pm$ 4.79
16	Oct. 22, 2006	0432-0436	55.5 $\pm$ 0.4	243.0 $\pm$ 1.8	1.49 $\pm$ 0.34	4.65 $\pm$ 0.21
17	Dec. 20, 2006	0436-0448	54.3 $\pm$ 0.4	248.9 $\pm$ 1.6	2.17 $\pm$ 1.09	9.60 $\pm$ 5.49
18	Jan. 29, 2007	1346-1358	54.6 $\pm$ 0.1	254.5 $\pm$ 0.1	1.83 $\pm$ 0.14	6.19 $\pm$ 0.32
19	Feb. 02, 2008	0130-0148	57.7 $\pm$ 0.7	245.1 $\pm$ 5.4	3.04 $\pm$ 0.14	11.48 $\pm$ 2.17
20		0214-0256	57.1 $\pm$ 0.6	240.0 $\pm$ 2.0	4.40 $\pm$ 1.89	9.74 $\pm$ 4.84
21	Feb. 05, 2008	0658-0716	54.6 $\pm$ 0.2	249.0 $\pm$ 1.1	1.28 $\pm$ 0.11	3.26 $\pm$ 0.31
22		0720-0732	54.7 $\pm$ 0.3	248.1 $\pm$ 2.0	0.82 $\pm$ 0.12	2.41 $\pm$ 0.51
23		1122-1126	54.5 $\pm$ 0.0	250.1 $\pm$ 0.1	1.05 $\pm$ 0.07	2.45 $\pm$ 0.43
24	Apr. 01, 2008	0424-0426	57.9 $\pm$ 0.1	240.9 $\pm$ 0.7	1.72 $\pm$ 0.18	3.84 $\pm$ 0.06
25	Sep. 08, 2008	0442-0450	53.9 $\pm$ 0.1	251.6 $\pm$ 1.3	0.80 $\pm$ 0.36	2.64 $\pm$ 1.29
26	Jul. 23, 2009	0710-0742	52.7 $\pm$ 0.1	253.3 $\pm$ 2.5	1.94 $\pm$ 0.17	5.65 $\pm$ 0.60
27		0848-0928	52.7 $\pm$ 0.1	250.9 $\pm$ 0.8	1.48 $\pm$ 0.29	4.56 $\pm$ 0.90

Table 4.2: Lists of the Parameters of the Analyzed Events

#	averaged value ± standard deviation				
	θ [deg]	r [km]	r_s [km]	r' [km]	r_{max} [km]
1	-44.7 ± 13.2	132.9 ± 13.0	73.4 ± 33.3	44.5 ± 15.2	233.0 ± 106.2
2	-54.0 ± 25.2	358.6 ± 76.0	154.6 ± 27.1	212.6 ± 116.0	363.6 ± 128.3
3	-76.2 ± 10.6	500.7 ± 112.0	161.4 ± 10.8	325.4 ± 126.7	481.9 ± 44.3
4	-18.0 ± 16.2	566.6 ± 51.2	152.5 ± 29.2	112.4 ± 28.7	423.8 ± 100.3
5	-11.8 ± 17.2	425.4 ± 31.6	179.8 ± 62.2	156.3 ± 54.7	480.5 ± 124.3
6	-5.8 ± 10.7	369.8 ± 61.6	137.8 ± 32.4	103.6 ± 36.7	392.2 ± 90.7
7	-3.0 ± 29.0	330.6 ± 5.2	65.0 ± 16.4	47.6 ± 20.4	278.2 ± 192.1
8	-13.5 ± 1.9	468.9 ± 7.9	60.9 ± 7.1	68.8 ± 4.2	124.9 ± 25.8
9	-77.3 ± 10.0	487.4 ± 113.0	113.1 ± 26.1	181.5 ± 80.5	424.1 ± 87.4
10	21.2 ± 8.7	343.3 ± 58.0	83.1 ± 6.9	123.4 ± 55.5	323.0 ± 19.4
11	1.9 ± 2.7	485.1 ± 52.0	95.8 ± 6.4	204.8 ± 23.8	367.5 ± 26.4
12	79.0 ± 13.9	261.5 ± 42.5	36.4 ± 8.8	70.7 ± 17.7	214.8 ± 70.0
13	14.3 ± 41.4	226.2 ± 25.6	19.6 ± 5.4	36.5 ± 12.9	144.4 ± 91.4
14	0.0 ± 50.2	337.8 ± 54.2	31.1 ± 13.0	32.7 ± 19.0	101.3 ± 36.0
15	12.0 ± 49.7	174.2 ± 94.0	102.3 ± 73.2	113.1 ± 113.9	470.8 ± 273.6
16	-71.6 ± 14.5	248.1 ± 122.9	73.5 ± 10.5	126.1 ± 76.5	271.5 ± 15.4
17	-15.0 ± 37.6	151.9 ± 108.9	117.4 ± 53.1	110.1 ± 111.4	545.9 ± 309.9
18	3.4 ± 11.3	500.3 ± 8.5	109.6 ± 4.9	208.9 ± 27.4	358.0 ± 15.8
19	-40.6 ± 21.0	350.1 ± 21.6	190.0 ± 20.3	136.9 ± 24.9	659.2 ± 116.3
20	-21.1 ± 27.4	506.6 ± 135.3	215.2 ± 91.1	356.7 ± 167.6	595.5 ± 282.3
21	58.5 ± 25.4	150.0 ± 3.8	77.2 ± 7.9	82.8 ± 15.2	194.3 ± 17.1
22	74.6 ± 10.7	93.8 ± 25.2	48.6 ± 11.3	46.6 ± 28.5	141.1 ± 28.4
23	0.1 ± 4.5	222.2 ± 5.5	57.5 ± 2.4	73.0 ± 11.9	148.2 ± 23.1
24	-58.1 ± 3.6	504.3 ± 33.9	75.4 ± 13.3	134.0 ± 49.6	233.4 ± 34.4
25	-22.5 ± 61.5	335.7 ± 95.6	39.6 ± 18.6	62.6 ± 40.9	153.1 ± 74.0
26	-48.6 ± 29.9	490.0 ± 19.8	125.0 ± 15.7	206.2 ± 36.8	331.3 ± 33.9
27	-39.9 ± 20.4	356.1 ± 39.5	106.2 ± 21.3	105.6 ± 26.5	265.9 ± 50.6
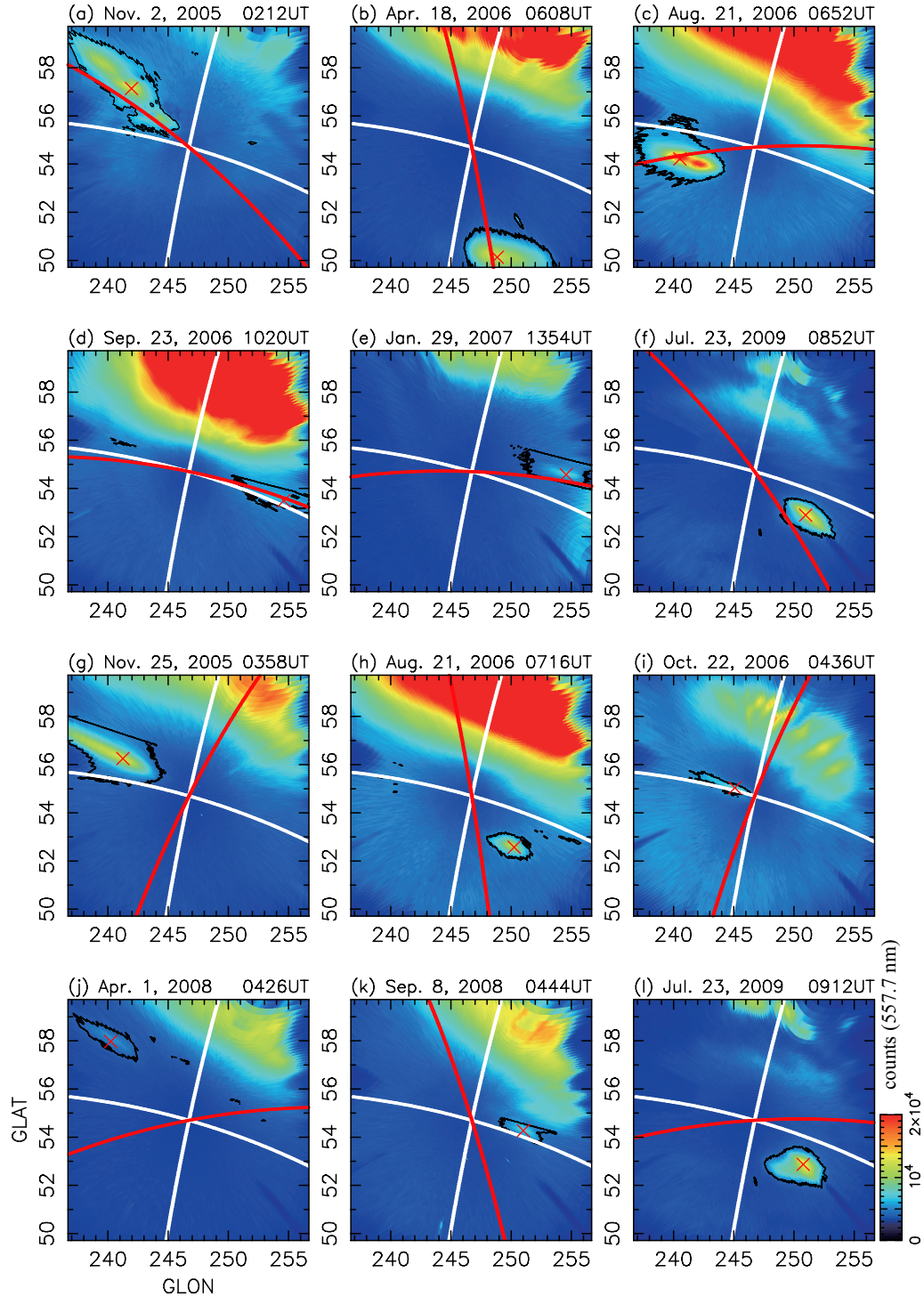
Figure 4.9: All-sky images at a wavelength of 557.7 nm centered on ATH with $10° \times 20°$ widths of geographic latitudes and longitudes. In the events (a-f) the major axis of the Pc1 polarization ellipse (red lines) pointed to the maximum count in the isolated proton aurora (cross). In the events (g-l) the major axis of the Pc1 polarization ellipse did not point to the isolated proton aurora. The black lines indicate the positions of the boundary counts (120-130% of background count), and the white lines are the equivalent geomagnetic latitude and longitude of ATH.
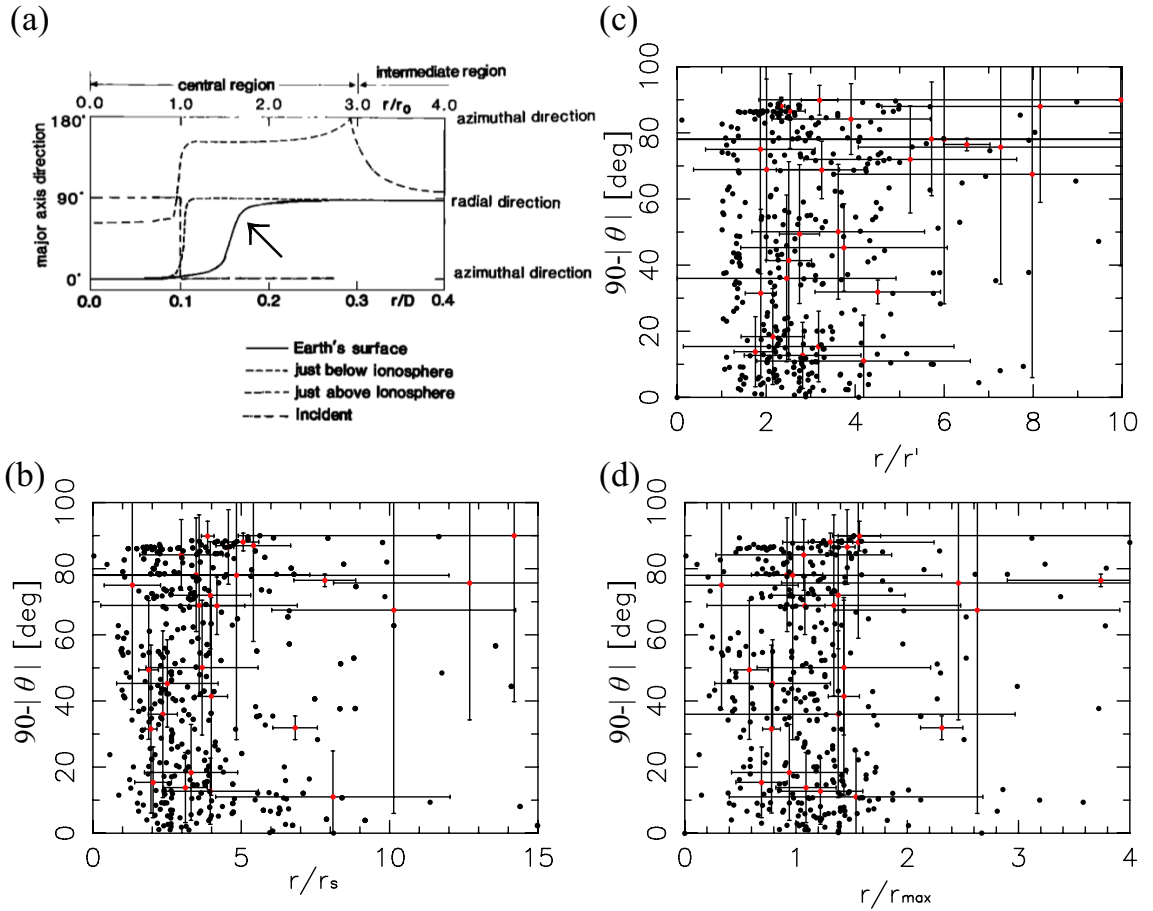
Figure 4.10: The dependence on r/r_0 of the absolute angle of rotation from the azimuthal direction $(90° - |\theta|)$ of the major axis of the Pc1 polarization ellipse. (a) The model calculation by Fujita and Tamao [1988] (Figure 6). The solid line indicated by an arrow in Figure 4.10a is the angle to be observed on the ground. (b) The result of our statistical analysis of 27 events over 4 years for (b) r/r_s, (c) r/r', and (d) r/r_{max}. The large and small circles are the temporally-averaged data and all the data, respectively. The error bar is the standard deviation.

with the model of Fujita and Tamao [1988] for the location of the transition region.

4.3 Discussion

We have compared the direction of the major axis of the Pc1 polarization ellipse with the possible Pc1 ionospheric source. This has not been done in previous studies, but it is important for understanding how Pc1 geomagnetic pulsations propagate from the ionospheric sources to the ground. For example, for event 1 (April 18, 2006), the major axis pointed toward the isolated proton aurora. This fact indicates that the compressional wave propagated from the direction of the proton aurora. Therefore, our observation indicates there is an ionospheric duct propagation, as shown by model calculations [e.g., *Greifinger*, 1972, *Fujita and Tamao*, 1988].

As shown in Figures 4.10b-d, we identified the transition regions at $r/r_s \sim$2.0-4.0, $r/r' \sim$2.0-4.0, and $r/r_{max} \sim$0.5-1.5 where the major axis of the Pc1 polarization ellipse rotates from the azimuthal direction ($90° - |\theta| = 0°$) to the radial direction ($90° - |\theta| = 90°$). This result indicates that Alfvén waves precipitate into the Pc1 ionospheric source and are converted to compressional waves in the ionospheric duct in a horizontal area at the transition region which is made by a mixture of these two waves, as suggested by the model calculation.

There are two possible errors to determine the edge of the Pc1 ionospheric source using proton auroras observed by an all-sky camera. They could cause either underestimation and overestimation of the scale size of the Pc1 ionospheric source. One possible error is that we could underestimate the scale size r_0 of the Pc1 ionospheric sources if the proton aurora was not clearly separated from the background emissions or if the proton aurora size is smaller than the Pc1 ionospheric source. The proton aurora usually becomes bright enough to distinguish from background when the amplitudes or the bandwidth of the Pc1 pulsation become larger. In Figures 4.1a and 4.1b, the aurora became bright at 0820UT. On the other hand, Pc1 waves began to be observed $\sim$15 min earlier than the aurora at 0805UT in Figures 4.1c and 4.1d, suggesting that the proton aurora intensity was too weak to be observed at the first 15 min. The region of EMIC waves excited by the ion cyclotron instability could be larger than the region of proton

precipitation caused by the resonance between EMIC waves and magnetospheric protons.

The other possible error is that when we observe proton aurora at 486.1 nm and 557.7 nm, the aurora size can be larger than the actual region of proton precipitation, because hydrogen particles emit 486.1 nm light when moving across the magnetic fields and excite Oxygen 557.7 nm emission. The difference between the boundary and the maximum counts to distinguish the background emission from the isolated proton aurora is usually the order of $\sim 10^4$ counts at a wavelength of 557.7 nm. Assuming that the noise level of the CCD is in the order of 10^2 counts, we can distinguish the proton aurora boundary at 10^{-2} of the peak intensity. *Davidson* [1965] showed by a model calculation of the intensity of proton auroras that, when the magnetospheric protons with an isotropic pitch-angle distribution precipitate along a magnetic field into the ionosphere, the emission at an altitude of 120 km with an intensity of 10^{-2} of the peak intensity will occur at $\sim 2°$ in latitude away from the peak. Therefore, the aurora size can be $\sim 2°$ (~ 220 km) larger than the size of the precipitation region. This causes the overestimation of r_0 in our analysis, meaning underestimation of r/r_0. Thus r/r_0 for the actual transition region may be larger than the observational result. The relation between the size of isolated proton aurora and that of EMIC waves or Pc1 ionospheric sources should be investigated in future.

In Figure 4.10c for r/r', we can see that the clearest tendency of the polarization angle dependence is similar to the model calculation in Figure 4.10a. This means that the Pc1 polarization observed on the ground is mainly determined by two distances, from the observation site to the brightest point and to the edge of the Pc1 ionospheric source. The transition region is at $r/r' \sim 2$-4. The averaged major axes tend to toward the proton aurora at $r/r' > 4$. We can also recognize two discrepancies between Figures 4.10a and 4.10c. One is that data points near $90° - |\theta|$ are not seen for $r/r' < 2$, and the other is the large error bars for $r/r' > 6$.

The smaller values of $r/r' < 2$ mean a small distance r from the proton aurora to the observation site, or a large radius r' of the proton aurora. In both cases, ATH would be located close to the edge of the proton aurora. The proton aurora observed in the present study suggests that the inhomogeneity of the conductivity occurs in the auroral region due to the proton precipitation. Fujita and Tamao

[1988] did not include such conductivity effect related to the proton precipitation in their model calculation. Belova et al. [1997] showed by a model calculation of the polarization characteristics of the geomagnetic pulsation that the polarization ellipse will rotate along the inhomogeneity of ionospheric conductivity. However, we do not know how the non-uniform conductivities affect the Pc1 polarization when they exist at the same location as the Pc1 ionospheric source. These topics will be studied in future.

The large values of $r/r' > 6$ mean a large distance r from the proton aurora to the observation site, or a small radius r' of the proton aurora. In the case of small radius r' of the proton aurora, small proton auroras with weak intensities of emissions are included. For such small and weak proton aurora, it is possible that the estimations of their scale sizes are affected by the background intensity variations. This effect could cause the statistical errors in Figure 4.10c at $r/r' > 6$.

In Figure 4.10, the transition regions from $90° - |\theta| = 0°$ to $90° - |\theta| = 90°$ occurs in the range of 2.0-4.0 for r/r_s and r/r', and 0.5-1.5 for r/r_{max}. One of the possible reason why the transition regions scatter in these ranges is that r/r_0 also depends on D as shown in Figure 4.10a, where D is the thickness of the ionospheric duct. In the model calculation of Fujita and Tamao [1988], D was assumed to be 1000km. In the case of $D' = 500$km and $D' = 2000$km, the value of r/D' will be twice and half of r/D, respectively. Thus we suggest that the differences in ionospheric conditions for different events cause the shift of the r/D thus the transition region.

The average scale sizes of the proton aurora for r_s, r', and r_{max} are $\sim$100 km in our statistical study. The transition regions are at $r/r_s \sim$2.0-4.0, $r/r' \sim$2.0-4.0, and $r_{max} \sim$0.5-1.5. Therefore, we suggest that in order to identify the ionospheric sources of Pc1/EMIC waves by remote sensing using ground induction magnetometers, the observation site should be located at a distance at least $r > \sim$400 km equatorward of the ionospheric source regions, which is typically at $\sim$60°mlat. Miyoshi et al. [2008] showed using a set of ground and satellite observations that EMIC waves can cause precipitation of relativistic electrons into an isolated proton aurora. The remote sensing method of subauroral magnetic measurement is useful for investigation of the interaction between EMIC waves and relativistic electrons in the inner magnetosphere.

As we pointed out in Section 2, the PSD of the Pc1 band shows fine structures with multiple peaks. The polarization parameters also vary depending on these fine spectral structures. By investigating the major axis of the Pc1 polarization ellipse at the PSD maximum without using band-pass filters, we found a relation of the Pc1 major axis direction to r/r_0 similar to that predicted in a model calculation. Thus we consider that the frequency component of the Pc1 wave associated with the PSD maximum propagated from the brightest point of the proton aurora. Nomura et al. [2011a] have shown the frequency dependence of the PSD and polarization parameters at low latitudes and suggested the existence of spatially distributed Pc1 ionospheric sources at high latitudes. Sometimes the proton aurora was observed to be composed of several spots (e.g., at 0836UT on April 18, 2006 in Figure 4.4), suggesting multiple Pc1 sources existing at the same time. Each small proton aurora could cause the fine structure in the PSD of Pc1 pulsations. Therefore, one possible reason for the multiple peaks in a PSD of Pc1 waves is that several Pc1/EMIC waves spatially stick together and reach the ionosphere at the same time. Then the frequency dependence of the polarization parameter could be caused by the differences of the small proton aurora spots in size and distance from the observation site on the ground. Fujita [1988] showed, however, that the attenuation of duct propagation could also cause similar multiple peaks in Pc1 bands.

4.4 Conclusions

In this chapter, we investigated the relation between the polarization of Pc1 geomagnetic pulsations observed by an induction magnetometer and isolated proton auroras which were simultaneously observed by an all-sky camera at a subauroral station ATH. A detailed spectrum and polarization analysis showed that Pc1 waves have multiple peaks in the power spectrum density (PSD) and a frequency dependence of their polarization. For 27 events over 4 years, the directions of the major axis for the Pc1 polarization ellipse corresponding to the PSD maximum were compared with the position of proton auroras, which we considered as projections of the Pc1 ionospheric source. We identified statistically that the rotation angle θ of the Pc1 polarization ellipse depended on r/r_s, r/r', and r/r_{max},

where r is the distance to the proton aurora and r_s, r', and r_{max} are measures of the proton aurora scale sizes. For example, for the event of April 18, 2006 between 0814 and 0836UT, the major axis of the Pc1 polarization ellipse pointed toward the isolated proton aurora. For the event of October 18, 2006, the major axis pointed, not to the isolated proton aurora, but in the azimuthal direction. The transition regions where the major axis changes from pointing in a direction toward proton auroras ($\theta=0°$) to pointing the perpendicular direction ($\theta=90°$) were observationally identified at $r/r_s \sim 2.0$-4.0, $r/r' \sim 2.0$-4.0, and $r/r_s \sim 0.5$-1.5, while the model calculation of Fujita and Tamao [1988] predicted $r/r_0 \sim 1.0$-2.0. These differences of the transition region may imply that the Pc1 ionospheric sources are larger than the isolated proton aurora, or that the inhomogenuity of the ionospheric conductivity by the proton precipitation affects the values of the transition region. For r/r' we can see that the clearest tendency of the polarization angle dependence is similar to the model calculation. This means that the Pc1 polarization observed on the ground is mainly determined by two distances, from the observation site to the brightest point and to the edge of the Pc1 ionospheric source. The averaged major axes tend to point toward the proton aurora at large r/r'. In our observations, the average scale size of the isolated proton aurora was ~ 100 km. Therefore, in order to make remote sensing of ionospheric sources of Pc1/EMIC waves by using polarization analysis of subauroral ground magnetic measurement, we suggest that the induction magnetometer should be located at least $r > \sim 400$ km equatorward of the ionospheric source regions, which is typically at $\sim 60°$mlat.

Chapter 5

Summary and Conclusions

In this thesis, we investigated the polarization characteristics (major axis of polarization and polarization sense) of Pc1 geomagnetic pulsations observed by induction magnetometers at low and subauroral latitudes. From the analysis of the magnetometer data at three low-latitude stations at PTK, MSR, and STA, we found that the Pc1 pulsations have the frequency dependence of polarization characteristics. We also investigated the seasonal and local time dependences of Pc1 polarization characteristics for 93 Pc1 events observed at MSR for 2 years. Pc1 pulsations are most frequently observed in winter and during the nighttime, in accordance with previous results. This indicates that the attenuation of Pc1 waves upon propagation by the ionospheric waveguide is weaker for lower F layer density. For $\sim70\%$ of Pc1 events, the major axis direction of Pc1 polarization waves depends on their frequency. For example, during the event on November 5, 2007, the major axis direction varies monotonically from $\sim20°$ eastward (0.4 Hz) to $\sim20°$ westward (0.8 Hz) (0°: the direction to the magnetic north). The polarization sense depends on frequency and time in a complex manner. We also newly found the correspondence of the temporal variation of the Pc1 polarization with the repetition of the pearl structures. This correspondence was suggested by the previous model calculation as the result of the superposition of several waves with slightly different frequencies. For the Pc1 event on November 5, 2007 at PTK and MSR, the repetition periods of pearl structures were ~5-30 s which is much shorter than the repetition period expected from the bouncing wave packet model, and also shorter than the repetition periods typically observed at high

latitudes.

From these observations, we suggest that spatially-distributed Pc1 sources with varying frequencies depending on locations at high latitudes propagate in the ionospheric duct to cause the observed frequency dependence of polarization parameters at low latitudes. We also suggest that the Pc1 pearl structures with a repetition period of ∼5-30 s observed at low latitudes are produced as a beat of these waves with slightly different frequencies. Present theoretical models cannot reliably interpret the observed features of the Pc1 polarization structure at low latitudes, which hampers the application of polarization analysis to the remote location of Pc1 sources.

Then we investigated the relation between the polarization of Pc1 pulsations observed by an induction magnetometer and isolated proton auroras which were simultaneously observed by an all-sky camera at a subauroral station ATH. The isolated proton aurora is considered as projections of the Pc1 ionospheric source. For 27 events over 4 years, the directions of the major axis for the Pc1 polarization ellipse at the frequency of the PSD maximum were compared with the distances from the Pc1 source to the observation site normalized by the scale size of the Pc1 source. We tried three different definitions of the scale size of Pc1 source for the normalized distances. We found that the rotation angle θ between the Pc1 polarization ellipse and the direction to the proton aurora changes from 90° to 0° as the normalized distance increases. For the definition of the scale sizes that gives most clear θ-transition from 90° to 0°, the transition occurs at the normalized distance ∼2.0-4.0, while it was ∼1.0-2.0 by the model calculation of Fujita and Tamao [1988]. These differences of the transition region may imply that the Pc1 ionospheric sources are larger than the isolated proton aurora, or that the inhomogenuity of the ionospheric conductivity by the proton precipitation affects the values of the transition region. For the normalized distances r/r' where r is the distance to the proton aurora and r' is the scale size of the proton aurora, we can see the clearest tendency of the polarization angle dependence similar to the model calculation. This means that the Pc1 polarization observed on the ground is mainly determined by two distances, from the observation site to the brightest point and to the edge of the Pc1 ionospheric source. The averaged major axes tend to point toward the proton aurora at large r/r'. In our observations, the

average scale size of the isolated proton aurora was $\sim$100 km. Therefore, in order to make remote sensing of ionospheric sources of Pc1/EMIC waves by using polarization analysis of subauroral ground magnetic measurement, we suggest that the induction magnetometer should be located at least $r >$400 km equatorward of the ionospheric source regions, which is typically at $\sim$60°mlat.

Future works

- **Remote sensing of the ionospheric source of Pc1/EMIC wave by multi-point magnetometer observation**

  We have investigated the Pc1 polarization characteristics and found that the major axis of Pc1 polarization waves will point toward the proton aurora which is the ionospheric source of Pc1/EMIC wave, when the observation site locates at a distance larger than $\sim$400 km from the region where the waves enter into the ionosphere. This polarization method is a powerful tool to find out the location of the ionospheric source of the Pc1/EMIC waves, because we can obtain 24-hour data of the induction magnetometers. However the remote sensing method has not been well established using the polarization method, and thus we do not know statistical characteristics for the location of the ionospheric source of Pc1/EMIC wave. It is necessary to investigate the major axes of the Pc1 polarization waves by the multi-point observation of the induction magnetometers, in order to estimate the location of the ionospheric source of Pc1/EMIC waves by the intersection of the major axes directions. Evaluation should be done for the accuracy of the estimated position by comparing the result to the actual location of the proton aurora.

- **Effect of the proton precipitation to the Pc1 polarization**

  In our observation, the transition region accompanied by the drastic rotation of the Pc1 polarization wave had different characteristics from that expected by the previous model calculation by Fujita and Tamao [1988]. This discrepancy may be explained by the inhomogeneity of the ionospheric conductivity caused by the proton precipitation, which was not included in the previous model. At low latitudes, we observed LH polarized frequency

components for which the previous model also did not predict. In order to see the conductivity effect to the Pc1 polarization wave, it is necessary to improve the model calculation of the Pc1 ionospheric source.

- **Possible pulsation of proton aurora and Pc1 pearl structure**
Sometimes the observed isolated proton aurora seemed to blink with periods shorter than 120 s, which is the time resolution of the all-sky camera observation we used in this study. No one has investigated variation of the isolated proton aurora emission in the time scale of less than 100 s. For the monochromatic proton-aurora imaging, we need an exposure time of $\sim$20 s because the emission of the proton aurora is very weak. However using observation of the proton aurora by a panchromatic imager with a sampling rate less than 1 s, new characteristics of the variation of the proton aurora emission associated with the Pc1 pulsation may be revealed.

  The variation of the proton aurora emission must be closely related to the variation of Pc1/EMIC waves considering the wave-particle interaction in the magnetospheric equatorial plane. Comparison of the variation of the proton aurora intensity with the repetition period of the pearl structure of Pc1/EMIC waves will be important to understand the mechanism of the Pc1 pearl structures. The energy of precipitating proton particles can be estimated by measuring the Doppler shift of H_β emission using the filter-tilting photometer. Thus it may be possible to compare the frequency of the Pc1/EMIC waves and the proton energy observation to check the resonance condition of EMIC waves with protons.

- **Localized and fine structures of isolated proton aurora**
We still do not understand the reason why the proton auroras simultaneously observed with the Pc1/EMIC waves are localized in a range less than $\sim$1° in latitudes and less than $\sim$1000 km in longitudes. Also we still do not know the exact mechanism for the latitudinal and longitudinal motions of the proton aurora. For example we observed the proton aurora moving westward with a velocity faster than that expected from the magnetospheric convection. By using a test particle simulation, one can investigate the energy dependence of the drift motion of ions in the magnetosphere which may

be related to the observed aurora motions. We also observed fine structures of emissions at a scale size of ∼10 km in the proton aurora. One of the possible mechanism of the localized and fine structure of the proton aurora is that the excitation region of waves is localized along the patchy structures of the plasmapause. It has been considered that the plasmapause is the region where the EMIC waves are frequently excited because the injected hot ions encounter the cold plasma of the plasmasphere to cause the ion cyclotron instability. Comparison between the two-dimensional distribution of the plasma density estimated by the cross-phase method (Chi and Russell [1998]) using ground magnetometers, and the proton aurora image related to Pc1/EMIC waves would be very interesting.

References

E. L. Althouse and J. R. Davis. Five-station observations of Pc 1 micropulsation propagation. *J. Geophys. Res.*, 83:132–144, January 1978. doi: 10.1029/JA083iA01p00132. 11, 41, 61, 67

E. Belova, E. Pchelkina, W. Lyatsky, and A. Pashin. The effect of ionospheric inhomogeneity on magnetic pulsation polarization: magnetic disturbance on the ground as a function of inhomogeneity magnitude. *J. Atmos. Terr. Phys.*, 59:1945–1952, 1997. doi: 10.1016/S1364-6826(97)00022-9. 87

P. J. Chi and C. T. Russell. An interpretation of the cross - phase spectrum of geomagnetic pulsations by the field line resonance theory. *Geophys. Res. Lett.*, 25:4445–4448, 1998. 94

G. T. Davidson. Expected Spatial Distribution of Low-Energy Protons Precipitated in the Auroral Zones. *J. Geophys. Res.*, 70:1061–1068, 1965. doi: 10.1029/JZ070i005p01061. 14

M. J. Engebretson, W. K. Peterson, J. L. Posch, M. R. Klatt, B. J. Anderson, C. T. Russell, H. J. Singer, R. L. Arnoldy, and H. Fukunishi. Observations of two types of pc 1-2 pulsations in the outer dayside magnetosphere. *J. Geophys. Res.*, 107(A12):1451,doi:10.1029/2001JA000198, 2002. 7, 61

M. J. Engebretson, J. L. Posch, A. M. Westerman, N. J. Otto, J. A. Slavin, G. Le, R. J. Strangeway, and M. R. Lessard. Temporal and spatial characteristics of Pc1 waves observed by ST5. *J. Geophys. Res.*, 113:A07206, July 2008. doi: 10.1029/2008JA013145. 12, 61

R. E. Erlandson, L. J. Zanetti, T. A. Potemra, L. P. Block, and G. Holmgren. Viking magnetic and electric field observations of Pc 1 waves at high latitudes. *J. Geophys. Res.*, 95:5941–5955, May 1990. doi: 10.1029/JA095iA05p05941. 41, 58

R. E. Erlandson, B. J. Anderson, and L. J. Zanetti. Viking magnetic and electric field observations of periodic Pc 1 waves - Pearl pulsations. *J. Geophys. Res.*, 971:14823–+, 1992. doi: 10.1029/92JA00838. 12, 13, 61

R. A. Fowler, B. J. Kotick, and R. D. Elliott. Polarization Analysis of Natural and Artificially Induced Geomagnetic Micropulsations. *J. Geophys. Res.*, 72: 2871–2883, June 1967. doi: 10.1029/JZ072i011p02871. 27, 30, 41, 42, 43, 65

B. J. Fraser. Temporal variations in pc1 geomagnetic micropulsations. *Planet. Space Sci.*, 72(11):2871–2883, 1968. 8

B. J. Fraser. Ionospheric duct propagation and Pc 1 pulsation sources. *J. Geophys. Res.*, 80:2790–2796, July 1975a. doi: 10.1029/JA080i019p02790. 10

B. J. Fraser. Polarization of Pc 1 pulsations at high and middle latitudes. *J. Geophys. Res.*, 80:2797–2807, July 1975b. doi: 10.1029/JA080i019p02797. 10, 11

B. J. Fraser. Pc 1 geomagnetic pulsation source regions and ionospheric waveguide propagation. *J. Atmos. Terr. Phys.*, 38:1141–1146, 1976. 11, 58

B. J. Fraser. Is the plasmapause a preferred source region of electromagnetic ion cyclotron waves in the magnetosphere? *J. Atmos. Terr. Phys.*, 63:1225–1247, 2001. 4

B. M. Fraser and W. R. Summers. Pcl micropulsations-Polarization of micropulsations propagated through ionospheric ducts. *Nat. Phys. Sci.*, 235:170–171, February 1972. 10, 67

S. Fujita. Duct propagation of hydromagnetic waves in the upper ionosphere. II - Dispersion characteristics and loss mechanism. *J. Geophys. Res.*, 931:14674–14682, 1988. doi: 10.1029/JA093iA12p14674. 49, 88

S. Fujita and T. Tamao. Duct propagation of hydromagnetic waves in the upper ionosphere. I - Electromagnetic field disturbances in high latitudes associated with localized incidence of a shear Alfven wave. *J. Geophys. Res.*, 931:14665–14673, December 1988. doi: 10.1029/JA093iA12p14665. iii, x, xvii, 2, 9, 11, 58, 61, 64, 69, 71, 74, 80, 84, 85, 86, 87, 89, 91, 92

H. Fukunishi, T. Toya, K. Koike, M. Kuwashima, and M. Kawamura. Classification of hydromagnetic emissions based on frequency-time spectra. *J. Geophys. Res.*, 86:9029–9039, 1981. doi: 10.1029/JA086iA11p09029. x, 1, 2, 4, 14, 43

H. Fukunishi, S. Kokubun, and N. Matsuura. **南極の科学** *2* **オーロラと超高層大気**. 古今書院, 1983. 4

J. Galejs. Arbitrary Propagation of HM Waves along the F Region. *J. Geophys. Res.*, 78:3894–3902, 1973. doi: 10.1029/JA078i019p03894. 57

C. Greifinger and P. Greifinger. Wave Guide Propagation of Micropulsations out of the Plane of the Geomagnetic Meridian. *J. Geophys. Res.*, 78:4611–4618, 1973. doi: 10.1029/JA078i022p04611. 60

C. Greifinger and P. S. Greifinger. Theory of Hydromagnetic Propagation in the Ionospheric Waveguide. *J. Geophys. Res.*, 73:7473–7490, 1968. doi: 10.1029/JA073i023p07473. 8, 60

P. Greifinger. Micropulsations from a Finite Source. *J. Geophys. Res.*, 77:2392–2396, 1972. doi: 10.1029/JA077i013p02392. 2, 9, 60

K. Hayashi, S. Kokubun, T. Oguti, K. Tsuruda, S. Machida, T. Kitamura, O. Saka, and T. Watanabe. The extent of Pc 1 source region in high latitudes. *Canadian Journal of Physics*, 59:1097–1105, August 1981. 11, 12

M. Hino. *Spectral analysis*. 朝倉書店, 1977. 27

T. Iyemori and K. Hayashi. PC 1 micropulsations observed by Magsat in the ionospheric F region. *J. Geophys. Res.*, 94:93–100, January 1989. doi: 10. 1029/JA094iA01p00093. 12

J. Jacobs, Y. Kato, S. Matsushita, and V. Troitskaya. Classification of geomagnetic micropulsations. *J. Geophys. Res.*, 69(1):180–181, 1964. x, 1, 12

J. Kangas, A. Guglielmi, and O. Pokhotelov. Morphology and physics of short-period magnetic pulsations. *Space Sci. Rev.*, 83:435–512, 1998. 49

M. Kawamura, M. Kuwashima, and T. Toya. Comparative Study of Magnetic Pc1 Pulsations between Low Latitudes and High Latitudes: Source Region and Propagation Mechanism of the Waves Deduced from the Characteristics of the Pulsations at Middle and Low Latitudes. *National Institute Polar Research Memoirs*, 18:83–100, March 1981. x, 4, 7, 8, 55

M. Kawamura, M. Kuwashima, T. Toya, and H. Fukunishi. Comparative study of magnetic pc 1 pulsations observed at low and high latitudes: Long-term variation of occurrence frequency of the pulsations. *National Institute Polar Research Memoirs*, 26:1–12, March 1983. 4, 9

H. Kim, M. R. Lessard, M. J. Engebretson, and M. A. Young. Statistical study of Pc1-2 wave propagation characteristics in the high-latitude ionospheric waveguide. *J. Geophys. Res.*, 116:7227, 2011. doi: 10.1029/2010JA016355. 67

M. Kuwashima, T. Toya, M. Kawamura, T. Hirasawa, H. Fukunishi, and M. Ayukawa. Comparative Study of Magnetic Pc1 Pulsations between Low Latitudes and High Latitudes: Statistical Study. *National Institute Polar Research Memoirs*, 18:101–117, March 1981. 8, 55

R. L. Lysak. Propagation of Alfvén waves through the ionosphere: Dependence on ionospheric parameters. *J. Geophys. Res.*, 1041:10017–10030, May 1999. doi: 10.1029/1999JA900024. 12

Y. Miyoshi, K. Sakaguchi, K. Shiokawa, D. Evans, J. Albert, M. Connors, and V. Jordanova. Precipitation of radiation belt electrons by EMIC waves, observed from ground and space. *Geophys. Res. Lett.*, 352:L23101, 2008. doi: 10.1029/2008GL035727. x, 15, 87

K. Mursula. Satellite observations of Pc 1 pearl waves: The changing paradigm. *J. Atmos. Terr. Phys.*, 69:1623–1634, 2007. doi: 10.1016/j.jastp.2007.02.013. 12, 13, 61

K. Mursula, R. Rasinkangas, T. Bösinger, R. E. Erlandson, and P.-A. Lindqvist. Nonbouncing Pc 1 wave bursts. *J. Geophys. Res.*, 1021:17611–17624, 1997. doi: 10.1029/97JA01080. 7, 12, 58, 61

D. A. Neudegg, B. J. Fraser, F. W. Menk, H. J. Hansen, G. B. Burns, R. J. Morris, and M. J. Underwood. Sources and velocities of Pc1-2 ULF waves at high latitudes. *Geophys. Res. Lett.*, 22:2965–2968, 1995. doi: 10.1029/95GL02939. 57

R. Nomura, K. Shiokawa, V. Pilipenko, and B. Shevtsov. Frequency‐dependent polarization characteristics of pc1 geomagnetic pulsations observed by multi-point ground stations at low latitudes. *J. Geophys. Res.*, 116:A01204, 2011a. 67, 88

T. Obayashi. Hydromagnetic whistlers. *J. Geophys. Res.*, 70:1069–1078, 1965. 12

V. A. Pilipenko, E. N. Fedorov, and M. J. Engebretson. Alfven resonator in the topside ionosphere beneath the auroral acceleration region. *J. Geophys. Res.*, 107(A02):1257, doi:10.1029/2002JA009282, 2002. 7

T. A. Plyasova-Bakounina, J. Kangas, K. Mursula, O. A. Molchanov, and A. W. Green. Pc 1-2 and Pc 4-5 pulsations observed at a network of high-latitude stations. *J. Geophys. Res.*, 1011:10965–10974, 1996. doi: 10.1029/95JA03770. 7, 61

J. H. Pope. An Explanation for the Apparent Polarization of Some Geomagnetic Micropulsations (Pearls). *J. Geophys. Res.*, 69:399–405, 1964. doi: 10.1029/ JZ069i003p00399. 62

J. L. Rauch and A. Roux. Ray tracing of ULF waves in a multicomponent magnetospheric plasma - Consequences for the generation mechanism of ion

cyclotron waves. *J. Geophys. Res.*, 87:8191–8198, October 1982. doi: 10.1029/ JA087iA10p08191. 11

K. Sakaguchi, K. Shiokawa, A. Ieda, Y. Miyoshi, Y. Otsuka, T. Ogawa, M. Connors, E. F. Donovan, and F. J. Rich. Simultaneous ground and satellite observations of an isolated proton arc at subauroral latitudes. *J. Geophys. Res.*, 112:A04202, 2007. doi: 10.1029/2006JA012135. 13, 65

K. Sakaguchi, K. Shiokawa, Y. Miyoshi, Y. Otsuka, T. Ogawa, K. Asamura, and M. Connors. Simultaneous appearance of isolated auroral arcs and Pc 1 geomagnetic pulsations at subauroral latitudes. *J. Geophys. Res.*, 113:A05201, 2008. doi: 10.1029/2007JA012888. 7, 13, 57, 65, 79

K. Shiokawa, Y. Katoh, M. Satoh, M. K. Ejiri, T. Ogawa, T. Nakamura, T. Tsuda, and R. H. Wiens. Development of Optical Mesosphere Thermosphere Imagers (OMTI). *Earth, Planets, and Space*, 51:887–896, 1999. xi, 26, 27, 64

K. Shiokawa, K. Hosokawa, K. Sakaguchi, A. Ieda, Y. Otsuka, T. Ogawa, and M. Connors. The Optical Mesosphere Thermosphere Imagers (OMTIs) for network measurements of aurora and airglow. In M. Hirahara, Y. Miyoshi, N. Terada, T. Mukai, & I. Shinohara, editor, *American Institute of Physics Conference Series*, volume 1144 of *American Institute of Physics Conference Series*, pages 212–215, June 2009. doi: 10.1063/1.3169292. 27, 64

K. Shiokawa, R. Nomura, K. Sakaguchi, Y. Otsuka, Y. Hamaguchi, M. Satoh, Y. Katoh, Y. Yamamoto, B. M. Shevtsov, S. Smirnov, I. Poddelsky, and M. Connors. The STEL induction magnetometer network for observation of high-frequency geomagnetic pulsations. *Earth, Planets, and Space*, 62:517–524, 2010. doi: 10.5047/eps.2010.05.003. 17, 42

W. R. Summers. Production mechanisms for the observed behavior of the low latitude Pcl polarization ellipse. *Planet. Space Sci.*, 22:801–809, May 1974. doi: 10.1016/0032-0633(74)90150-0. 11, 60

W. R. Summers and B. J. Fraser. Polarization properties of Pc 1 micropulsations at low latitudes. *Planet. Space Sci.*, 20:1323–1335, August 1972. doi: 10.1016/ 0032-0633(72)90019-0. 11, 41, 60

M. E. Usanova, I. R. Mann, I. J. Rae, Z. C. Kale, V. Angelopoulos, J. W. Bonnell, K.-H. Glassmeier, H. U. Auster, and H. J. Singer. Multipoint observations of magnetospheric compression-related EMIC Pc1 waves by THEMIS and CARISMA. *Geophys. Res. Lett.*, 351:L17S25, 2008. doi: 10.1029/2008GL034458. 12, 61

D. J. Webster and B. J. Fraser. Source structure and dynamics of Pc1 pulsations at low latitudes. *Planet. Space Sci.*, 32:935–947, August 1984. doi: 10.1016/0032-0633(84)90050-3. 10

D. J. Webster and B. J. Fraser. Source regions of low-latitude Pc1 pulsations and their relationship to the plasmapause. *Planet. Space Sci.*, 33:777–793, 1985. doi: 10.1016/0032-0633(85)90032-7. 41

A. G. Yahnin, T. A. Yahnina, and H. U. Frey. Subauroral proton spots visualize the Pc1 source. *J. Geophys. Res.*, 112:A10223, 2007. doi: 10.1029/2007JA012501. 13

A. G. Yahnin, T. A. Yahnina, H. U. Frey, T. Bösinger, and J. Manninen. Proton aurora related to intervals of pulsations of diminishing periods. *J. Geophys. Res.*, 114:12215, 2009. doi: 10.1029/2009JA014670. 7

T. A. Yahnina, A. G. Yahnin, J. Kangas, and J. Manninen. Proton precipitation related to Pc1 pulsations. *Geophys. Res. Lett.*, 27:3575–3578, 2000. doi: 10.1029/2000GL003763. 13

T. A. Yahnina, H. U. Frey, T. Bösinger, and A. G. Yahnin. Evidence for subauroral proton flashes on the dayside as the result of the ion cyclotron interaction. *J. Geophys. Res.*, 113:A07209, 2008. doi: 10.1029/2008JA013099. 13

副 論 文

1. Nomura, R., K. Shiokawa, V. Pilipenko, and B. Shevtsov (2011), Frequency-dependent polarization characteristics of Pc1 geomagnetic pulsations observed by multipoint ground stations at low latitudes, *J. Geophys. Res.*, *116*, A01204, doi:10.1029/2010JA015684.

2. Nomura, R., K. Shiokawa, K. Sakaguchi, Y. Otsuka, and M. Connors (2012), Polarization of Pc1/ EMIC waves and related proton auroras observed at subauroral latitudes, *J. Geophys. Res.*, in press.

参 考 論 文

Shiokawa, K., R. Nomura, K. Sakaguchi, Y. Otsuka, Y. Hamaguchi, M. Satoh, Y. Katoh, Y. Yamamoto, B. M. Shevtsov, S. Smirnov, I. Poddelsky, and M. Connors (2010), The STEL induction magnetometer network for observation of high-frequency geomagnetic pulsations, *Earth Planets Space*, *62*, 517–524.